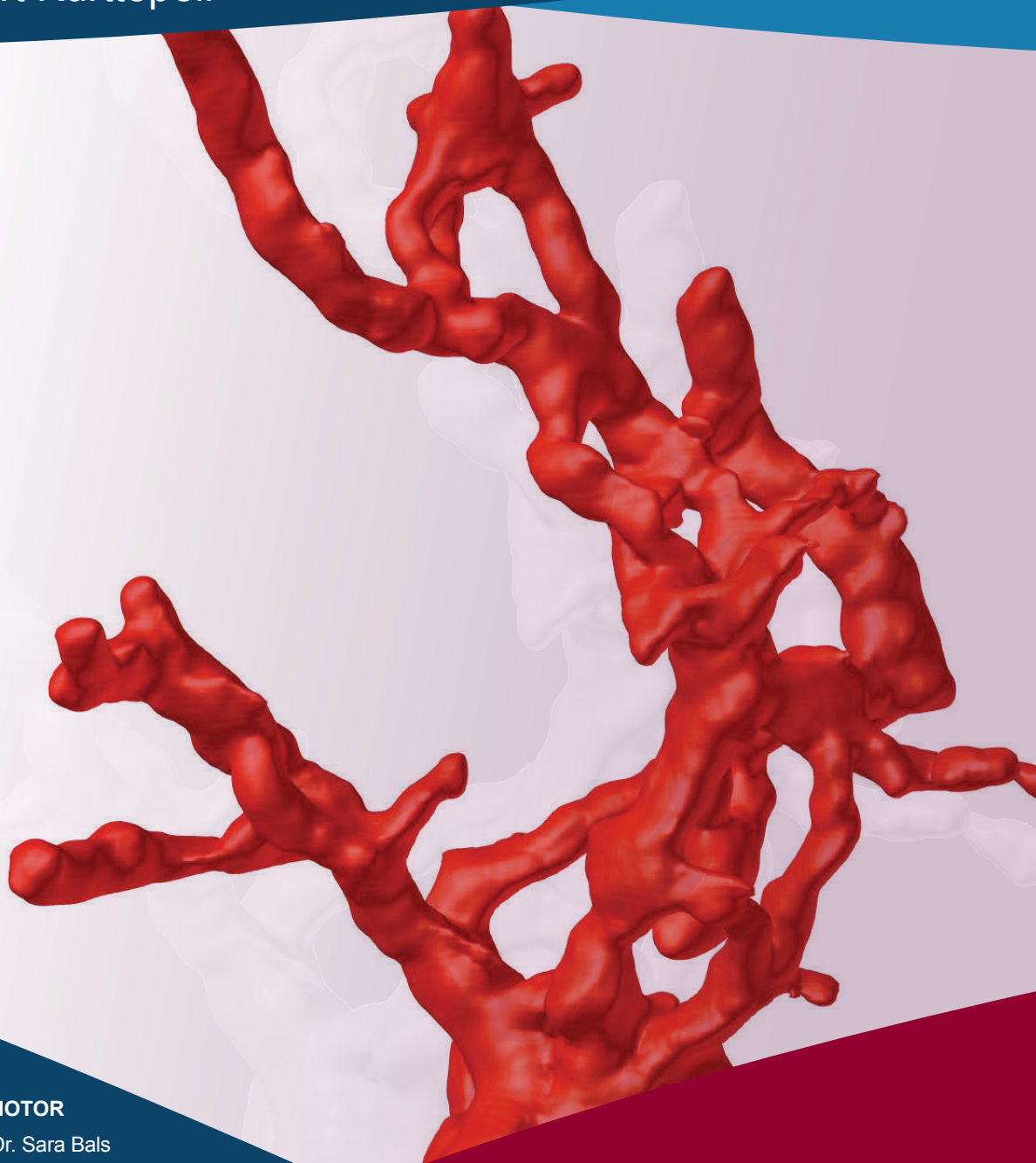


Carbon Based Materials and Hybrid Nanostructures Investigated by Advanced Transmission Electron Microscopy

Proefschrift voorgelegd tot het behalen van de graad van Doctor in de Wetenschappen aan de Universiteit Antwerpen te verdedigen door

Mert Kurttepli



PROMOTOR

Prof. Dr. Sara Bals

Faculteit Wetenschappen
Departement Fysica
Antwerpen 2015

 Universiteit
Antwerpen

CARBON BASED MATERIALS AND HYBRID
NANOSTRUCTURES INVESTIGATED BY ADVANCED
TRANSMISSION ELECTRON MICROSCOPY

GEAVANCEERDE TRANSMISSIE-
ELEKTRONENMICROSCOPIE STUDIE VAN KOOLSTOF
GEBASEERDE MATERIALEN EN HYBRIDE
NANOSTRUCTUREN

Proefschrift voorgelegd tot het behalen van de graad van

Doctor in de Wetenschappen

aan de Universiteit Antwerpen, te verdedigen door

Mert Kurttepli

Promotor:

Prof. Dr. Sara Bals

Antwerpen, 2015

Doctoral Committee

Chairman

Prof. Dr. Michiel Wouters, University of Antwerp, Belgium

Promoter

Prof. Dr. Sara Bals, University of Antwerp, Belgium

Members

Prof. Dr. Christophe Detavernier, Ghent University, Belgium

Prof. Dr. Jin Won Seo, KU Leuven, Belgium

Prof. Dr. Silvia Lenaerts, University of Antwerp, Belgium

Prof. Dr. Wim Wenseleers, University of Antwerp, Belgium

Prof. Dr. Gustaaf Van Tendeloo, University of Antwerp, Belgium

Contact Information

Mert Kurttepli

University of Antwerp - Department of Physics

EMAT - Electron Microscopy for Materials Science

Groenenborgerlaan 171

B-2020 Antwerp

Belgium

mert.kurttepli@uantwerpen.be

Table of Contents

CHAPTER 1 INTRODUCTION	3
1.1 ALLOTROPES OF CARBON.....	3
1.2 CARBON NANOSHEETS	3
<i>Carbon nanosheets: Properties</i>	4
<i>Carbon nanosheets: Synthesis</i>	5
<i>Carbon nanosheets: Applications</i>	6
1.3 CARBON NANOTUBES.....	6
<i>Carbon nanotubes: Properties</i>	7
<i>Carbon nanotubes: Synthesis</i>	7
<i>Carbon nanotubes: Applications</i>	10
1.4 CHARACTERIZATIONS OF CARBON BASED MATERIALS AND HYBRID NANOSTRUCTURES	11
1.5 OUTLINE OF THE THESIS.....	12
CHAPTER 2 ELECTRON MICROSCOPY	17
2.1 SCANNING ELECTRON MICROSCOPY	17
2.2 TRANSMISSION ELECTRON MICROSCOPY	18
2.2.1 SAMPLE PREPARATION.....	18
<i>Crushing</i>	19
<i>Ion-beam milling</i>	19
<i>Ion-beam milling: Plan-view sample preparation</i>	19
<i>Ion-beam milling: Cross-section sample preparation</i>	20

<i>Focused-ion beam</i>	21
2.2.2 TRANSMISSION ELECTRON MICROSCOPY TECHNIQUES	22
<i>Bright field transmission electron microscopy</i>	24
<i>Electron diffraction</i>	24
<i>High resolution transmission electron microscopy</i>	25
<i>Scanning transmission electron microscopy</i>	26
<i>Energy dispersive X-ray spectroscopy</i>	27
<i>Electron energy-loss spectroscopy</i>	28
<i>Energy-filtered transmission electron microscopy</i>	29
<i>Electron tomography</i>	30
2.3 TRANSMISSION ELECTRON MICROSCOPY OF MATERIALS COMPRISING CNSS AND CNTS.....	33
PART I STRUCTURAL CHARACTERIZATION OF ALIGNED CARBON NANOTUBE BUNDLES SYNTHESIZED THROUGH POROUS MEMBRANES . 37	
PART I: INTRODUCTION.....	39
CHAPTER 3 TRANSMISSION ELECTRON MICROSCOPY STUDY OF ALIGNED CARBON NANOTUBE BUNDLES SYNTHESIZED THROUGH ANODIZED ALUMINA MEMBRANE PORES	
3.1 INTRODUCTION	45
3.2 EXPERIMENTAL DETAILS.....	47
<i>Synthesis of aligned carbon nanotube bundles</i>	47
<i>Characterization techniques</i>	48
3.3 RESULTS.....	50
3.4 DISCUSSION.....	56
3.5 CONCLUSIONS	59

CHAPTER 4 CHARACTERIZATION OF HIERARCHICAL MESOPOROUS SILICA SYNTHESIZED THROUGH ANODIZED ALUMINA MEMBRANES	63
4.1 INTRODUCTION	63
4.2 EXPERIMENTAL PROCEDURES.....	65
<i>Evaporation induced self-assembly (EISA)</i>	65
<i>Sample preparation for transmission electron microscopy</i>	66
<i>Transmission electron microscopy</i>	66
4.3 RESULTS.....	67
4.4 DISCUSSIONS.....	71
4.5 CONCLUSIONS	72
PART II CHARACTERIZATION OF CARBON NANOSHEETS/NANOTUBES TEMPLATE ASSISTED AND ATOMIC LAYER DEPOSITION BASED SYNTHESIS OF POROUS MATERIALS	73
PART II: INTRODUCTION	75
CHAPTER 5 CHARACTERIZATION OF PHOTOREACTIVE TiO ₂ /CARBON NANOSHEET MATERIALS.....	83
5.1 INTRODUCTION	83
5.2 EXPERIMENTAL DETAILS.....	85
<i>SEM and TEM characterizations</i>	85
<i>Photocatalytic activity tests</i>	85
<i>Carbon nanosheets growth on silicon substrate</i>	86
<i>ALD-based synthesis and annealing of TiO₂ nanostructures</i>	86
5.3 RESULTS.....	88
<i>Post-ALD calcination in air environment</i>	88
<i>Post-ALD calcination in helium environment</i>	89
5.4 DISCUSSION.....	96

5.5	CONCLUSIONS	98	
CHAPTER 6 TEM INVESTIGATION OF POROUS NANOSTRUCTURED METAL OXIDES SYNTHESIZED THROUGH ATOMIC LAYER DEPOSITION ON A CARBONACEOUS TEMPLATE FOLLOWED BY CALCINATION			101
6.1	INTRODUCTION	101	
6.2	EXPERIMENTAL DETAILS	102	
6.3	RESULTS AND DISCUSSION	102	
	<i>Al₂O₃ hollow nanotubes</i>	103	
	<i>TiO₂ nanoparticle chains</i>	104	
	<i>V₂O₅ and ZnO network of interconnected nanoparticles</i>	107	
	<i>Kinetics of carbon removal</i>	112	
6.4	CONCLUSIONS	113	
CHAPTER 7 INVESTIGATION OF A 3D NETWORK OF PT NANOWIRES SYNTHESIZED BY ATOMIC LAYER DEPOSITION ON A CARBONACEOUS TEMPLATE			117
7.1	INTRODUCTION	117	
7.2	EXPERIMENTAL DETAILS	118	
7.3	RESULTS AND DISCUSSION	119	
7.4	CONCLUSIONS	126	
CHAPTER 8 CONCLUSIONS AND FUTURE RESEARCH			129
BIBLIOGRAPHY			135
SCIENTIFIC CONTRIBUTIONS			163

List of Abbreviations

1D	1-Dimensional
2D	2-Dimensional
3D	3-Dimensional
aCNTb's	Aligned Carbon Nanotube Bundles
AAO	Anodized Alumina
ADF	Annular Dark Field
ALD	Atomic Layer Deposition
AlPO	Al-isopropoxide
BF	Bright Field
BFTEM	Bright field transmission electron microscopy
CCD	Charge-coupled Device
CVD	Chemical Vapor Deposition
CNS	Carbon Nanosheet
CNT	Carbon Nanotube
DEZn	Diethylzinc
EDX	Energy Dispersive X-ray Spectroscopy
EELS	Electron Energy-Loss Spectroscopy
EFTEM	Energy Filtered Transmission Electron Microscopy
EISA	Evaporation Induced Self-Assembly
FEG	Field Emission Gun
FIB	Focused Ion Beam
GIS	Gas-injection System

LIST OF ABBREVIATIONS

HAADF	High-angle Annular Dark Field
HMM	Hierarchical Mesoporous Membrane
HRTEM	High Resolution Transmission Electron Microscopy
CTAB	Ionic Hexadecyl-Trimethyl-Ammonium Bromide
MWCNT	Multi-Walled Carbon Nanotube
MWPECVD	Micro-wave Plasma Enhanced Chemical Vapor Deposition
OMS	Ordered Mesoporous Silica System
PECVD	Plasma Enhanced Chemical Vapor Deposition
RF	Radio Frequency
SAED	Selected Area Electron Diffraction
SAXS	Small-Angle X-Ray Scattering
SEM	Scanning Electron Microscopy
SIRT	Simultaneous Iterative Reconstruction Technique
STEM	Scanning Transmission Electron Microscopy
SWCNT	Single-Walled Carbon Nanotube
TDMAT	Tetrakis(dimethylamido)titanium
TEM	Transmission Electron Microscopy
TEMAV	Tetrakis-(ethylmethylamino)vanadium
TEOS	Tetraethoxysilane
TMA	Trimethylaluminum
UV	Ultraviolet
WBP	Weighted-back projection
XRD	X-Ray Diffraction

Preface

Carbon based materials have been investigated intensely in the materials science community for decades owing to their exceptional electrical, physical, chemical and mechanical properties. One of the main trends in this research field is to synthesize allotropes of carbon, such as carbon nanotubes, via a templated approach, which can lead to enhancements in their morphologies. Another popular trend is to use allotropes of carbon (such as carbon nanosheets and carbon nanotubes) as templates for the deposition of different metal/metal oxide layers in order to form hybrid nanostructured films for a wide range of materials applications. In both cases, the interaction between carbonaceous species with their coatings/templates plays a vital role in the final structure and morphology of the materials. Investigation of the carbon based materials and hybrid nanostructures is therefore crucial to understand their properties, which may lead to their use in actual applications.

Transmission electron microscopy is a powerful technique to study materials at the atomic level. The combination of conventional transmission electron microscopy techniques with more advanced ones, such as electron tomography, enables one to obtain valuable structural and chemical information, both in two- and three-dimensions. Moreover, through the instrumental developments, such as aberration correction, the characterization of carbon based materials and hybrid nanostructures using transmission electron microscopy has become of increasing interest.

This thesis focuses on the structural characterization of carbon based materials and hybrid nanostructures performed by transmission electron microscopy. The thesis is divided into two main parts. The first part is devoted to the systematic investigation of structures obtained using a method based on a templated approach, which aims to produce large areas of highly ordered, isolated, well-aligned and long carbon nanotube bundles. The second part focuses on

the structural characterization of carbon nanosheets and carbon nanotubes which are used as templates for the synthesis of various metal/metal oxides for different materials applications. Combining conventional and advanced transmission electron microscopy techniques, the structural transitions and the interaction between coatings/templates and carbonaceous species have been revealed. The content of this thesis is divided into eight chapters, organized as follows:

Chapter 1 provides a general introduction to allotropes of carbon, where the main emphasis was put on two main types, namely carbon nanosheets and carbon nanotubes. Their properties, synthesis and applications are discussed.

Chapter 2 focuses on explaining all the electron microscopy techniques that were performed to characterize the materials which were described in this thesis.

Chapter 3 covers all work carried out on the investigation of carbon nanotubes fabricated by catalytic chemical vapor deposition through porous anodized alumina membranes. Transmission electron microscopy is used to reveal the characteristics of the templated materials at each step of their synthesis. Initially, the effects of a short pre-chemical vapor deposition NaOH etching step on the adhesion characteristics of the catalysts at the anodized alumina membrane pores are discussed. Following the growth of carbon nanotubes, advanced transmission electron microscopy experiments, including electron tomography combined with energy-dispersive X-ray spectroscopy, were performed to report the presence of aligned carbon nanotube bundles and to reveal the dominant carbon nanotube growth type.

In **Chapter 4**, the investigation of mesoporous silica formed inside the pores of anodized alumina membranes is presented. The presence of such additional template can be beneficial for increasing the alignment of as-grown carbon nanotubes in anodized alumina templated carbon nanotube growth approach. However, an optimization of the mesopores of silica is essential. In this chapter, it is demonstrated that transmission electron microscopy can be used both in a qualitative and quantitative manner to investigate these materials for the optimization of the mesoporous silica synthesis.

Chapter 5 presents an application of carbon nanosheets as templates to deposit TiO₂ layers through atomic layer deposition followed by a post-deposition annealing in helium environment. The resulting materials can be used in photocatalysis applications. In such case, the anatase content of the TiO₂ layer is important. Therefore, advanced transmission electron microscopy characterizations, including electron energy loss spectroscopy, were performed to determine the phase analysis of TiO₂ layer. In addition, the presence of a conductive carbon nanosheets layer in between a substrate and TiO₂ layer is observed, which can be beneficial for different materials applications.

In **Chapter 6**, the investigation of different metal oxide layers, such as Al₂O₃, TiO₂, V₂O₅ and ZnO, deposited onto forests of carbon nanotubes by atomic layer deposition is shown. As part of the research, the structure of the resulting materials and the effects of post-deposition annealing in air environment on each type of the metal oxide layer were studied by transmission electron microscopy.

Chapter 7 presents an application of Pt deposited onto forests of carbon nanotubes by atomic layer deposition and subsequent annealing in air environment. Conventional and advanced transmission electron microscopy techniques were performed to report on the crystallinity of Pt layer both prior to and upon annealing. In addition, electron tomography experiments were conducted to observe the morphological transformations which occur at the Pt-carbon nanotube film as a result of the annealing step.

Finally, in **Chapter 8**, general conclusions are presented.

Voorwoord

Koolstof gebaseerde materialen worden al decennia lang intensief bestudeerd door wetenschappers omwille van hun uitzonderlijke elektrische, fysische, chemische en mechanische eigenschappen. Een belangrijke trend is het synthetiseren van koolstof allotropen, zoals de synthese van koolstof nanobuizen via een mal methode, waardoor de morfologie van de nanobuizen kan verbeterd worden. Een andere populaire trend is het gebruik van koolstof allotropen (zoals koolstof nanobuizen en koolstof nanoplaten) als mal voor de depositie van verschillende metaal/metaaloxide lagen om zo hybride nanogestructureerde films voor verschillende toepassingen te vormen. In beide gevallen speelt de interactie tussen koolstofhoudende materialen en hun coatings /mallen een belangrijke rol in de resulterende structuur en morfologie van het composietmateriaal. Het onderzoek van koolstof gebaseerde composieten en hybride nanostructuren is daarom van uitermate belang om zo hun eigenschappen, die kunnen leiden tot concrete toepassingen, te begrijpen.

Transmissie-elektronenmicroscopie is een krachtige techniek om materialen tot op atomair niveau te bestuderen. De combinatie van conventionele en meer geavanceerde transmissie-elektronenmicroscopie technieken, zoals elektronentomografie, leidt tot het verkrijgen van waardevolle morfologische en chemische informatie, zowel in twee als in drie dimensies. Bovendien is er een toenemende belangstelling voor de karakterisering van koolstof gebaseerde composieten en hybride nanostructuren door middel van transmissie-elektronenmicroscopie omwille van instrumentele ontwikkelingen, zoals aberratie correctie.

Dit proefschrift behandelt de morfologische karakterisering van koolstof gebaseerde composieten en hybride nanostructuren aan de hand van transmissie-elektronenmicroscopie. Het proefschrift bestaat uit twee grote delen. In het eerste deel worden structuren die verkregen werden door een mal methode, waarbij men een groot aantal geordende, afzonderlijke, goed

uitgelijnde en lange koolstof nanobuis bundels tracht te bekomen, systematisch onderzocht. In het tweede deel wordt de karakterisering van de morfologie van koolstof nanoplaten en koolstof nanobuizen, die gebruikt worden als mal voor de synthese van verschillende metalen / metaaloxiden voor verschillende materiaalkundige toepassingen, onderzocht. De structurele overgangen en de interactie tussen coatings / mallen en koolstofhoudende materialen worden bestudeerd aan de hand van een combinatie van conventionele en geavanceerde transmissie-elektronenmicroscopie technieken. De inhoud van dit proefschrift wordt verdeeld in acht hoofdstukken:

Hoofdstuk 1 geeft een algemene inleiding over koolstof allotropen, waarbij de nadruk wordt gelegd op koolstof nanoplaten en koolstof nanobuizen. Zowel hun eigenschappen, synthese en toepassingen worden besproken.

In **hoofdstuk 2** worden de elektronenmicroscopie technieken, die gebruikt werden om de onderzochte materialen te karakteriseren, uitgelegd.

Hoofdstuk 3 behandelt het onderzoek van de koolstof nanobuizen die vervaardigd werden door katalytische chemische dampdepositie (*catalytic CVD*, *catalytic chemical vapor deposition*) aan de hand van poreuze geanodiseerde aluminium membranen. Transmissie-elektronenmicroscopie wordt gebruikt om de eigenschappen van de composietmaterialen te onthullen bij elke stap van de synthese. Aanvankelijk, worden de effecten van een korte *pre-CVD NaOH etsstap* op de hechtingseigenschappen van de katalysatoren aan de geanodiseerde alumina membraanporiën besproken. Na de groei van de koolstof nanobuizen, wordt de aanwezigheid van uitgelijnde koolstof nanobuis bundels en het dominante groeitype onderzocht. Dit gebeurt door middel van geavanceerde transmissie-elektronenmicroscopie experimenten, waarbij elektronentomografie gecombineerd wordt met energie-dispersieve X-stralen spectroscopie.

In **hoofdstuk 4** wordt het onderzoek van mesoporeuze silica, die gevormd worden binnenin de poriën van de geanodiseerd aluminium membranen, weergegeven. De aanwezigheid van een dergelijk aanvullende mal kan nuttig zijn om de uitlijning van de as-groei van koolstof nanobuizen te verhogen in de geanodiseerd aluminium mal groei methode. Een optimalisatie van de mesoporiën van silica is echter noodzakelijk. In dit hoofdstuk wordt aangetoond dat

transmissie-elektronenmicroscopie zowel kwalitatieve als kwantitatieve resultaten oplevert, die gebruikt kunnen worden om de synthese van de mesoporeuze silica te verbeteren.

In **hoofdstuk 5** wordt de toepassing van koolstof nanoplaten als mal voor de depositie van TiO₂ lagen door middel van atomaire laag depositie (ALD, *atomic layer deposition*), gevolgd door een na-depositie gloeiproces (*annealing*) in een helium omgeving, besproken. De resulterende materialen kunnen gebruikt worden in fotokatalytische toepassingen. Hierbij is de anataasvorm van de TiO₂ laag erg belangrijk. Aan de hand van geavanceerde transmissie-elektronenmicroscopie karakterisering, zoals elektron energieverlies spectroscopie (EELS, *electron energy loss spectroscopy*), wordt de fase van de TiO₂ laag onderzocht. De aanwezigheid van een geleidende koolstof nanoplaat laag tussen een substraat en de TiO₂ laag is bovendien waargenomen. De aanwezigheid van deze geleidende laag kan voordelig zijn, voornamelijk in kleurstof gesynthetiseerde zonneceltoepassingen.

In **hoofdstuk 6** worden verschillende metaaloxide lagen, zoals Al₂O₃, TiO₂, V₂O₅ en ZnO, die gedeponerd worden op een veld van koolstof nanobuizen door ALD, onderzocht. Als onderdeel van het onderzoek, worden de structuur van de resulterende materialen en de effecten van het na-depositie gloeien in lucht omgeving op elk type metaaloxide laag bestudeerd met transmissie-elektronenmicroscopie.

Hoofdstuk 7 behandelt de toepassing van Pt depositie op een veld van koolstof nanobuizen door middel van ALD en een daaropvolgend gloeiproces in lucht omgeving. Conventionele en geavanceerde transmissie-elektronenmicroscopie technieken worden uitgevoerd om de kristalliniteit van de Pt laag, voorafgaand aan en na het gloeien, aan te tonen. Bovendien, worden elektronentomografie experimenten toegepast om de morfologische veranderingen, die optreden aan de Pt-koolstof nanobuis film als gevolg van de gloeistap, waar te nemen.

Tot slot worden in **hoofdstuk 8** de algemene conclusies van dit proefschrift weergegeven.

Chapter 1 INTRODUCTION

CONTENTS

CHAPTER 1 INTRODUCTION	3
1.1 ALLOTROPES OF CARBON.....	3
1.2 CARBON NANOSHEETS	3
<i>Carbon nanosheets: Properties</i>	4
<i>Carbon nanosheets: Synthesis</i>	5
<i>Carbon nanosheets: Applications</i>	6
1.3 CARBON NANOTUBES.....	6
<i>Carbon nanotubes: Properties</i>	7
<i>Carbon nanotubes: Synthesis</i>	7
<i>Carbon nanotubes: Applications</i>	10
1.4 CHARACTERIZATIONS OF CARBON BASED MATERIALS AND HYBRID NANOSTRUCTURES	11
1.5 OUTLINE OF THE THESIS	12

Chapter 1 Introduction

In this chapter, a brief introduction will be given on two main types of carbon allotropes, namely carbon nanosheets and carbon nanotubes, and their synthesis, properties and applications will be discussed. Main emphasis will be put on the importance of their in-depth structural characterizations in applications such as their use as templates for the deposition of different metals/metal oxides as well as the templated growth of carbon nanotubes, which can lead to enhancements in their morphologies.

1.1 Allotropes of carbon

Carbon atoms can exert three different types of hybridizations; sp , sp^2 , and sp^3 . Each of these unique valence states belongs to a distinct archetypical, i.e., generic allotropic form of carbon that is characterized by its polymeric connectivity¹. Hence, the sp^3 -type of hybridization corresponds to a spatial three dimensional (3D) polymer of carbon with strong σ bonds to adjacent atoms, i.e., diamond; the sp^2 -type of hybridization corresponds to a planar two dimensional (2D) polymer with strong σ bonds in a plane and weaker π bond on one or more neighboring atoms, i.e., graphite; and finally, the sp -type of hybridization corresponds to a linear one dimensional (1D) chain-like polymer of carbon with strong σ bond directed along the $\pm x$ -axis, and two electrons entering $p\pi$ orbitals in the y and z directions, i.e. carbyne^{1,2}. Graphite, the allotropic form of carbon exerting mostly sp^2 -type of hybridization state, consists of a succession of layers parallel to the basal plane of hexagonally linked carbon atoms. Each of these layers is called graphene, and it constitutes the building block of both carbon nanosheets and carbon nanotubes, as will be explained in the following sections.

1.2 Carbon nanosheets

Ever since its discovery in 2004³, graphene has been drawing worldwide attention due to its unique properties. Graphene is a single atomic layer of sp^2 hybridized carbon atoms packed densely in a honeycomb lattice (see Figure 1-(A)), that can be folded into buckyballs, rolled into nanotubes, or stacked into graphite⁴. In case of the latter, graphene sheets stack together along the c -axis to generate graphite with an interlayer spacing of 0.34 nm, which produces strong in-plane bonding but poor van der Waals interaction between the layers⁴. Based on this

structure, a new and similar type of carbon nanostructure, called carbon nanosheets (CNSs), has been produced^{5,6}. These are nanomaterials made up of several graphene layers similar to graphite⁵. To demonstrate this, a high-resolution transmission electron microscopy (HRTEM) image from the edge of a CNSs flake is presented in Figure 1-(B). The HRTEM image reveals individual graphene layers with an interlayer spacing of 0.34 nm, as mentioned previously. Due to their graphitic nature, the properties, synthesis and applications of CNSs are closely related to that of graphite as well as graphene.

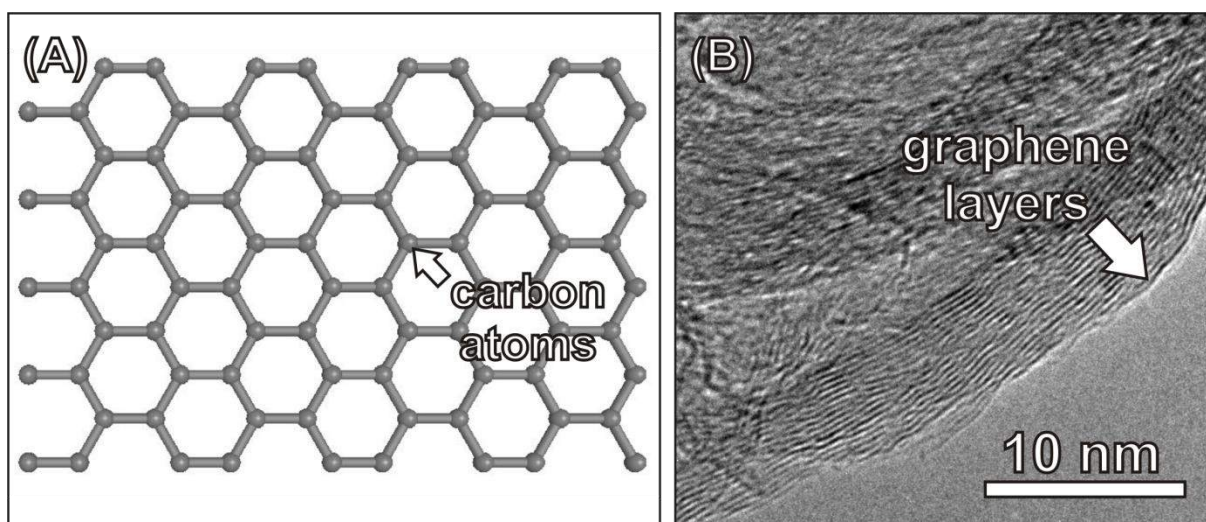


Figure 1 (A) Graphene honeycomb lattice. (B) HRTEM image of CNSs displaying their graphitic nature.

Carbon nanosheets: Properties

Some of the important properties of CNSs are their flexibility, elasticity, the fact that they are lightweight, and their chemical and thermal stability⁷. Thin layered graphitic films of CNSs retain graphene-like properties, such as high carrier mobility, large sustainable current density and superior electrical conductivity along the plane of the sheet^{6,8}. CNSs also have very high surface areas⁶, exceeding 1000 m²/g. Moreover, when compared to single layer graphene, CNSs have more defective sites on their surface. Both high surface-area-to-volume ratio and an increased number of surface defects are considered as important materials properties, especially in terms of their use as templates for the deposition of various metal/metal oxide structures. An application of CNSs as templates for the deposition of TiO₂ layer will be presented in Chapter 5, where their increased number of surface defects and high surface areas will be regarded as advantageous towards their uses as a coating surface.

Carbon nanosheets: Synthesis

In the early studies, CNSs have been synthesized using a technique referred to as radio frequency (RF) plasma enhanced chemical vapor deposition (PECVD), which enabled the formation of vertically-oriented, atomically thin and two-dimensional CNSs⁶. In addition, CNSs with different morphologies such as carbon nanowalls, nanoflakes, petal-like films or graphite sheets have also been reported by many groups, who employed various synthetic methods, including arc discharge-based technique⁹, RF sputtering¹⁰, PECVD¹¹⁻¹³ and other chemical processes¹⁴. Among these, PECVD is still regarded as the most promising approach for CNSs growth. When using PECVD, the growth of CNSs is achieved through plasma to enhance chemical reaction rates of the precursors. In general, PECVD is known for its feasibility and potential for large-area production with high quality, high growth rate and/or atomically thin characteristics¹⁵. The other main advantages of this technique are related to the fact that the CNSs can be synthesized at relatively low temperatures and the resulting materials offer a high amount of defect sites. These defects in CNS films provide an advantage towards their use as a conductive template to enhance the adhesion and surface area of metal oxide electrodes, as observed for TiO₂^{8,16}. A scanning electron microscopy (SEM) image from the surface of CNSs produced via the PECVD presented in Figure 2 reveals its morphology. Chapter 5 of this thesis includes the characterization of CNSs grown on single-crystalline silicon substrates synthesized via the PECVD process.

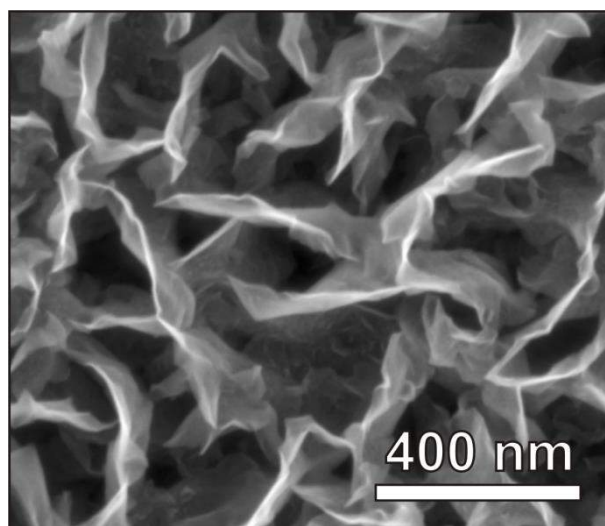


Figure 2 SEM image of the surface of CNSs from which a high surface area can be observed.

Carbon nanosheets: Applications

Carbon nanosheets exhibit great promise for potential applications in many technological fields. For instance, it was previously shown that the CNSs can be used as a support material for Pt nanoparticles in electrocatalysis applications¹⁷. The analysis of CNSs-Pt nanoparticles comprising materials showed that the CNSs give rise to a modification to the electrocatalytic properties of the Pt clusters. In another study, the electrochemical performance of CNSs as anode material for lithium-ion batteries was investigated¹⁸. The study revealed that the CNSs exhibit a relatively high reversible capacity and fine cycle performance. Moreover, the performance of CNSs was also evaluated as an electrode material for an electrochemical double-layer capacitor¹⁹, in which the capacitance of CNSs per area was found to be 0.076 Fcm^{-2} as a working electrode. Recently, there is an increasing interest in using CNSs as a template to fabricate multifunctional nanomaterials, which combine a material that provides ideal support properties, such as the high surface area of CNSs, with the desired properties of a second material. In this case, the application of CNSs as template mostly benefits from their outstanding surface properties and morphology^{5,20,21}. As mentioned previously, the application of CNSs as templates for the deposition of TiO_2 will be shown in Chapter 5 of this study, where their increased number of surface defects and high surface areas will be exploited as important properties in determining the final characteristics of the resulting material.

1.3 Carbon nanotubes

“Here I report the preparation of a new type of finite carbon structure consisting of needle-like tubes.” This is the sentence Prof. Iijima used in his abstract when he declared his discovery of carbon nanotubes (CNTs)²² to the rest of the world. Ever since, CNTs have been investigated intensely in many fields. CNTs can be considered as single or multiple graphene sheets rolled up as a tube. Structures corresponding to a single rolled up graphene sheet are referred to as single-walled carbon nanotubes (SWCNTs). Multi-walled carbon nanotubes (MWCNTs), on the other hand, contain two or more graphene sheets. Schematic drawings of SWCNT and MWCNT are presented in Figure 3-(A) and (B). In this section, a brief introduction about the properties, synthesis and applications of CNTs will be given. Since this

this thesis mainly deals with the growth and the use of MWCNTs as templates, therefore more attention will be paid to MWCNTs.

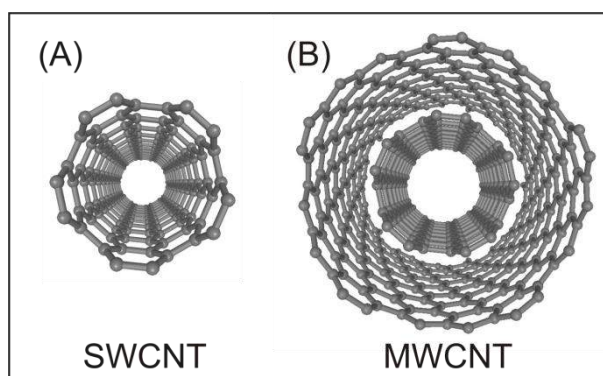


Figure 3 Schematic drawings of (A) SWCNT and (B) MWCNT.

Carbon nanotubes: Properties

The morphology of CNTs is an important feature which predefines some of their properties, especially when their outstanding aspect ratios (length/diameter) and extremely high surface areas are considered. The diameters of SWCNTs and MWCNTs are typically range from 0.8 to 2 nm and 5 to 20 nm, respectively²³. The length of CNTs range from less than 100 nm to several centimeters²³. When considering the cross-sectional area of the CNT walls only, an elastic modulus approaching 1 TPa and a tensile strength of 100 GPa has been measured for single MWCNTs²⁴, which is over 10-fold higher than any industrial fiber. Individual SWCNTs can have a thermal conductivity of $3500 \text{ Wm}^{-1}\text{K}^{-1}$ at room temperature based on the wall area²⁵, which exceeds the thermal conductivity of diamond^{23,26}. Regarding the electrical properties, MWCNTs are typically metallic²⁷ and can carry currents of up to 109 A cm^{-2} . In addition, compared to SWCNTs, MWCNTs are known to yield more structural defects or impurity sites on the tube walls²⁸. As will be shown in Chapter 6 and Chapter 7, this is an important feature and as a result, depositing thin layer coatings onto MWCNTs is less challenging.

Carbon nanotubes: Synthesis

The most commonly used techniques to produce CNTs are summarized in Table 1. These techniques include arc discharge, laser ablation (vaporization) and CVD. Both arc discharge and laser ablation methods are considered as high temperature preparation techniques.

Depending on whether pure or catalyst including graphite rods or targets are used, both MWCNTs and SWCNTs can be produced with each of these techniques. The main advantage of arc discharge technique is that it is a very simple and straightforward technique to produce CNTs. However, there are also several drawbacks. For instance, the technique leads to the production of a complex mixture of components, and further purification is required to collect CNTs. On the other hand, laser ablation is one of the superior methods to grow CNTs with high-quality and high-purity. The disadvantage here is that since this method involves evaporating the carbon source, which is also the case for arc discharge method, it becomes difficult to scale up the production into the industrial level²⁹.

CNTs synthesis methods	References
Arc discharge	22,30,31
Laser ablation	32,33
Hot filament CVD	34
Water assisted CVD	35–37
Oxygen assisted CVD	38
Micro-wave plasma CVD	13,15
Radio frequency CVD	39
Thermal CVD	40
Plasma enhanced CVD	41,42

Table 1 Commonly used methods for CNTs synthesis.

CVD, also known as thermal CVD or catalytic CVD⁴³, is one of the most popular and standard methods for CNTs production. A schematic drawing of a CVD synthesis reactor in its simplest form is presented in Figure 4-(A). Generally, the catalytic CVD process includes the decomposition of hydrocarbons in a tube reactor at 550-900°C, and the growth of CNTs over the catalysts deposited on a substrate. There are two major mechanisms, which are used to explain the catalytic growth of CNTs that depend on the position of the catalyst with respect to the substrate (see Figure 4-(B) and (C)). These are the root growth mechanism, in which the catalyst particle is found at the bottom of the tube (see Figure 4-(B)), and tip growth mechanism, where the catalyst particle is located at the tip of a growing tube (see Figure 4-(C)). Depending on the catalyst-support interaction, either of these mechanisms can occur. If

the interaction is strong, it is more likely that the root-growth mechanism takes place, but, if this interaction is weak, the tip-growth mechanism would also be more dominant.

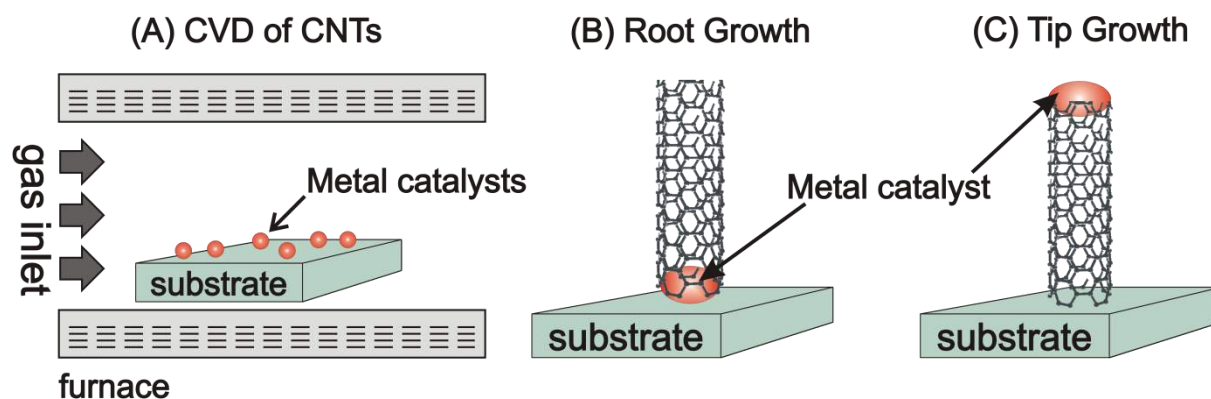


Figure 4 (A) Schematic drawing of a CVD synthesis reactor as well as (B) the root growth and (C) the tip growth mechanism of CNTs.

Since the catalytic CVD process is performed at a lower temperature and ambient pressure when compared to arc-discharge and laser ablation techniques, it is particularly useful for large-quantity synthesis of CNTs. In terms of crystallinity, arc-discharge and laser-grown CNTs are superior to the catalytic CVD-grown ones. However, concerning the yield, purity and structural control, catalytic CVD is superior to the arc and laser methods. One of the main technological advantages of catalytic CVD over arc discharge and laser ablation is that seeding a surface with active metal catalysts can lead to selective catalytic CVD on the seeded regions. This selective nature of the catalytic CVD enables one to use substrates with complex morphologies, e.g. patterned wafers⁴⁴ or porous membranes⁴⁵, which is not the case for arc discharge and laser ablation⁴⁶. Therefore, catalytic CVD provides the possibility to harness plenty of hydrocarbons in any state (solid, liquid or gas), and to grow CNTs with desired architecture on predefined sites of patterned or porous substrates⁴⁷. An example of CNTs grown through a porous substrate (anodized alumina) via the catalytic CVD process will be covered in Chapter 3.

There are trends to use other types of CVD techniques, such as water assisted CVD, oxygen assisted CVD, radio frequency CVD, or micro-wave plasma enhanced CVD (MWPECVD). Examples of the application of these techniques from the literature are given in Table 1. Some of these methods have been developed to perform CVD at even lower temperatures than usual, allowing the nanotubes to be grown at thermally sensitive substrates⁴⁸. Among these,

PECVD is a widely used technique. In this approach, electron energy (plasma) is used as an excitation method to perform CNT growth at a low temperature and at a moderate rate. An important characteristic of PECVD grown CNTs (or CVD in general, if the as-grown CNTs are compared with the ones formed through arc-discharge and laser ablation methods) is that there are high defect densities in the MWCNT structures grown by this process. This is most likely due to the lack of sufficient thermal energy for annealing CNTs because of relatively low growth temperature⁴⁹. These defects make the CNT surface reactive to the atomic species of an atomic layer deposition precursor²⁸. Examples of atomic layer deposition onto MWCNTs will be presented in Chapter 6 and Chapter 7. A SEM image of a PECVD grown CNT is presented in Figure 5-(A). A HRTEM image in Figure 5-(B) displays the graphitic layers of the MWCNT grown by this technique. Part II of this thesis partially concerns MWCNTs forests grown on single-crystalline silicon substrates synthesized via catalyst-enhanced PECVD process. The experimental details of the PECVD of MWCNTs will also be covered in this section.

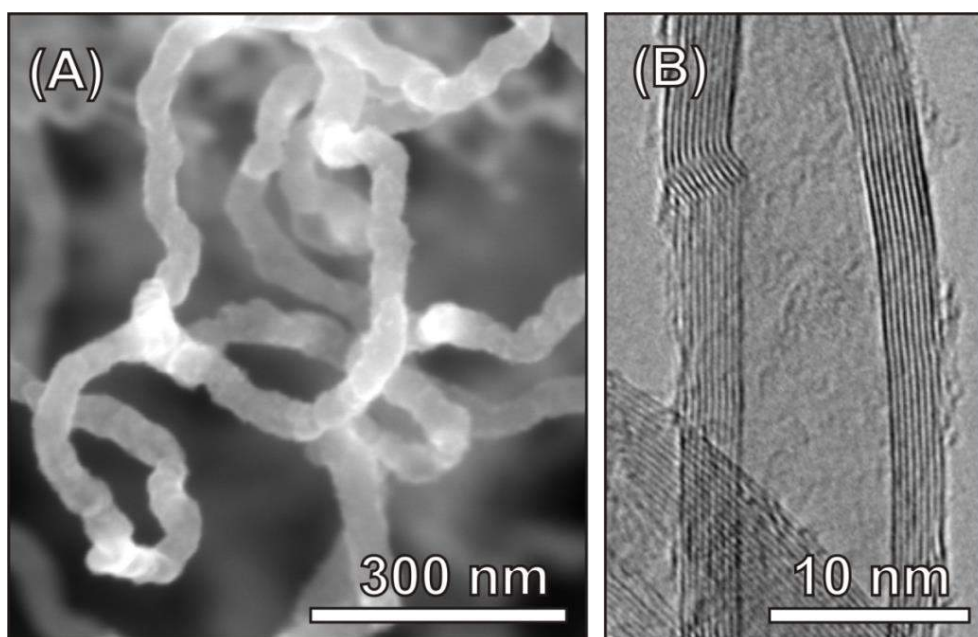


Figure 5 (A) SEM image of a CNT synthesized by PECVD method. (B) HRTEM image of a MWCNT showing the graphitic layers in the tube.

Carbon nanotubes: Applications

The type of the application is usually dependent on the structure of the CNTs (number of walls, diameter, length, chiral angle, etc.), which also determines their specific properties⁵⁰.

One of the major application areas for which CNTs are investigated is the biomedical field. The development of efficient methodologies for the chemical modification of CNTs (functionalization) has stimulated the preparation of soluble CNTs that can be used for the delivery of small drug molecules, exploiting their ability to penetrate into the cells⁵¹. Ongoing interest in CNTs as components of bio-sensors and medical devices is motivated by the dimensional and chemical compatibility of CNTs with biomolecules, such as DNA and proteins²³. In electronics, CNTs are considered to be promising building blocks for nanoscopic electronic devices⁵², or field effect transistors⁵³. CNTs are used in many other applications, for instance in hydrogen storage applications, showing very high hydrogen uptake efficiencies⁵⁴. Similar to CNSs, CNTs exhibit extremely high aspect ratios, high number of defect sites and large surface areas, which are attractive properties for many applications of CNTs, for instance, as templates for different material depositions. In Chapter 6 and Chapter 7 of this thesis, the characterization of MWCNTs and their applications as templates for various metals/metal oxides depositions will be shown.

1.4 Characterizations of carbon based materials and hybrid nanostructures

Nowadays, one of the main trends in carbon related research is to synthesize allotropes of carbon, for instance CNTs, via a templated approach. The aim here is to exploit the extraordinary physical properties of individual CNTs into their fiber or bundle forms. Furthermore, another popular trend is to use carbonaceous templates, e.g. CNSs or CNTs, for the deposition of different metals/metal oxides to obtain various nanomaterials for a wide range of applications. For the synthesis of such materials, atomic layer deposition (ALD) was found to be a powerful technique, through which fine layers of a material can be deposited onto complex template structures, including MWCNTs forest or CNSs flakes. Both ALD of CNSs and CNTs and the templated growth of CNTs will be thoroughly discussed in the following chapters. In both cases of these applications, it should be noted that understanding the interaction between different materials components, such as between the as-grown CNTs and their templates, or between CNTs or CNSs and their coatings, is important. Therefore, an in-depth characterization is essential. Such characterization is therefore the topic of this thesis.

In the past, several characterization techniques, including *in situ* X-Ray diffraction⁵⁵⁻⁵⁷ (*in situ* XRD) and SEM accompanied by energy dispersive X-ray spectroscopy⁵⁸⁻⁶⁰ (SEM-EDX), were utilized to fully examine nanomaterials. *In situ* XRD has proven to be a useful technique to uncover the physical and chemical mechanisms controlling the characteristics of nanomaterials. However, *in situ* XRD mostly provides structural information and identification of the phases from bulk samples at a given or an interval of temperature rather than their local characterization⁶¹. Similarly, SEM-EDX measurements can only be sufficient to evaluate the morphologies of materials mostly at the micrometer scale due to the limited spatial resolution of this technique. In this respect, TEM is an ideal tool in order to perform a detailed characterization at the nano-scale. Not only structural, but also chemical and electronic information can nowadays be obtained by TEM, even atomic column by atomic column^{62,63}. In this thesis, a variety of TEM techniques has accordingly been performed, including HRTEM, scanning TEM (STEM), electron energy-loss spectroscopy (EELS) and EDX. However, it is important to note that these conventional TEM techniques mostly yield 2D projection images of 3D objects. To obtain the correct 3D information about materials, TEM has been expanded to 3D, which is referred to as “electron tomography”. By combining all these conventional and more advanced TEM techniques, the main goal is to provide a thorough structural characterization, both in 2D and 3D. In this manner, the growth (Chapter 3 and Chapter 4) and the applications of CNSs and CNTs (Chapter 5, Chapter 6 and Chapter 7) can be optimized. Therefore, Chapter 2 of this thesis is dedicated to explaining the TEM techniques used in this study to characterize the materials described here.

1.5 Outline of the thesis

The most effective way to utilize the properties of individual CNTs, such as high strength, high stiffness and low density, is to assemble CNTs into fibers. Previous studies have shown that the CNTs can be used to form fibers of very high length. For instance, it was shown that it is possible to wind up a continuous fiber without an apparent limit to the length by mechanically drawing the CNTs directly from the gaseous reaction zone⁶⁴. In another study, it was reported that multi-ply, torque-stabilized fibers can be produced by introducing a twist during spinning of MWCNTs from nanotube forests⁶⁵. However, in both of these cases the resulting materials exhibit significantly reduced strength when compared to the strength of the

individual CNTs. A possible route to overcome this problem is to allow bundling of CNTs during their synthesis by using a porous material as a substrate for the CNT growth. With this approach, well aligned CNT bundles (aCNTb's) can directly be grown by means of catalytic CVD, since it allows selective CVD on the catalyst particle deposited regions at a porous template, as mentioned previously. In the first part of this thesis, we focus on the structural characterization of such aCNTb's directly grown through porous anodized alumina (AAO) membranes performed by TEM. These results are covered in Chapter 3. In addition, the templated synthesis of CNTs can be improved even further by introducing an additional template material, e.g. mesoporous silica, inside the pores of AAO membrane. By doing so, an increase at the alignment and the quality of the as-grown aCNTb's can be achieved. However, this initially requires the optimization of the pore architecture of the mesoporous silica prior to the CNT growth. In Chapter 4, it will be shown that advanced TEM techniques can be performed on these complex AAO-Silica materials systems, which can yield valuable information that could assist the optimization of their synthesis.

In the second part of this thesis, we present detailed characterizations of ALD processed CNSs and MWCNTs and describe the effects of post-deposition annealing in air or helium environments on the morphology of the resulting self-supported porous films. Since the MWCNTs and CNSs are grown through PECVD, and the resulting materials contain high amount of defects, and these defects give rise to nucleation sites for ALD, allowing for conformal deposition^{20,66}. By taking this into account, the structural details of TiO₂ layers deposited onto CNSs and their morphological and crystalline characteristics prior to annealing in helium environment are revealed by TEM (Chapter 5). In case of ALD-processed MWCNTs, earlier studies showed that the calcination in ambient air would lead to the removal of MWCNTs. In principle, this should lead to the metal/metal oxide coatings with a final tubular morphology. However, it is far from straightforward to achieve such tubular morphology with ultra-thin coatings on MWCNTs. We observed through TEM that depending on the type of coating, different morphologies could be obtained. For instance, ALD of very thin layers of TiO₂ on MWCNTs forest and subsequent calcination in ambient air removes the MWCNTs and a final morphology with interconnected crystallized TiO₂ nanoparticles is observed. In Chapter 6, we report on the characterization of porous metal oxides (Al₂O₃, TiO₂, V₂O₅ and ZnO) with different morphologies formed by ALD on MWCNTs forests followed

by post-deposition calcination in air based on TEM results. In addition to metal oxide films, another possibility of the use of MWCNTs for ALD is the growth of porous metal films, for instance, platinum (Pt). In Chapter 7, we present results from the TEM characterizations of ALD processed Pt on MWCNTs forests and reveal the formation of a 3D network comprising pure self-supporting Pt nanowires upon removal of the MWCNTs through calcining in air.

Chapter 2 ELECTRON MICROSCOPY

CONTENTS

CHAPTER 2 ELECTRON MICROSCOPY	17
2.1 SCANNING ELECTRON MICROSCOPY	17
2.2 TRANSMISSION ELECTRON MICROSCOPY	18
2.2.1 SAMPLE PREPARATION	18
<i>Crushing</i>	19
<i>Ion-beam milling</i>	19
<i>Ion-beam milling: Plan-view sample preparation</i>	19
<i>Ion-beam milling: Cross-section sample preparation</i>	20
<i>Focused-ion beam</i>	21
2.2.2 TRANSMISSION ELECTRON MICROSCOPY TECHNIQUES	22
<i>Bright field transmission electron microscopy</i>	24
<i>Electron diffraction</i>	24
<i>High resolution transmission electron microscopy</i>	25
<i>Scanning transmission electron microscopy</i>	26
<i>Energy dispersive X-ray spectroscopy</i>	27
<i>Electron energy-loss spectroscopy</i>	28
<i>Energy-filtered transmission electron microscopy</i>	29
<i>Electron tomography</i>	30
2.3 TRANSMISSION ELECTRON MICROSCOPY OF MATERIALS COMPRISING CNSs AND CNTs.....	33

Chapter 2 Electron microscopy

Since the realization of the first TEM by Max Knoll and Ernst Ruska in 1931, much progress has been made in improving instruments and methods for exploring the microstructure and the nanostructure of the materials. Today, TEM is a very powerful technique, which allows investigating complex material systems at the atomic scale not only from structural, but also from chemical and electronic point of views. With regard to this, TEM has been the primary characterization method. This chapter is devoted to presenting all the TEM characterization techniques performed in this work. Furthermore, the experimental details of SEM and EDX are briefly explained.

2.1 Scanning electron microscopy

SEM is a method, which uses electrons for imaging of surfaces. The electrons are produced by a thermal emission source, such as a heated tungsten filament, or by a field emission cathode. The energy of the electrons can be as low as 100 eV or as high as 30 keV, depending on the objective of the characterization and the type of material investigated. The electrons are focused into a fine beam by a series of electromagnetic lenses inside the SEM column (see Figure 6). The scanning coils direct, position and raster the focused beam on the sample surface. Once the focused electrons interact with a sample, their energy is dissipated as a variety of signals produced by electron-sample interaction. These resulting signals include secondary electrons and photons (X-rays). Secondary electrons are emitted from the inelastic collisions of the incident electrons with the electrons in the k-orbital of the specimen's atoms. Once the secondary electrons that escape the surface of the sample are collected by a detector, they are used for imaging the morphology and topography of samples. An example of a SEM image acquired by the collection of secondary electrons is given in Figure 6-right. Similarly, X-rays are generated by the inelastic collisions of the incident electrons with electrons in discrete orbitals (shells) of atoms in the sample. As the incident electrons knock out in discrete orbitals (shells) of atoms in the sample, outer shell electrons go to these emptied lower energy states, and upon this, they yield X-rays that are of a fixed wavelength related to the difference in energy levels of electrons in different shells for a given element. These characteristic X-rays are used for chemical analysis, known as energy-dispersive X-ray

spectroscopy (EDX). Nowadays, qualitative and quantitative chemical analysis information can be obtained using SEM accompanied with EDX. Figure 6-left presents an example of EDX elemental mapping from a region specified by the SEM image given on the right.

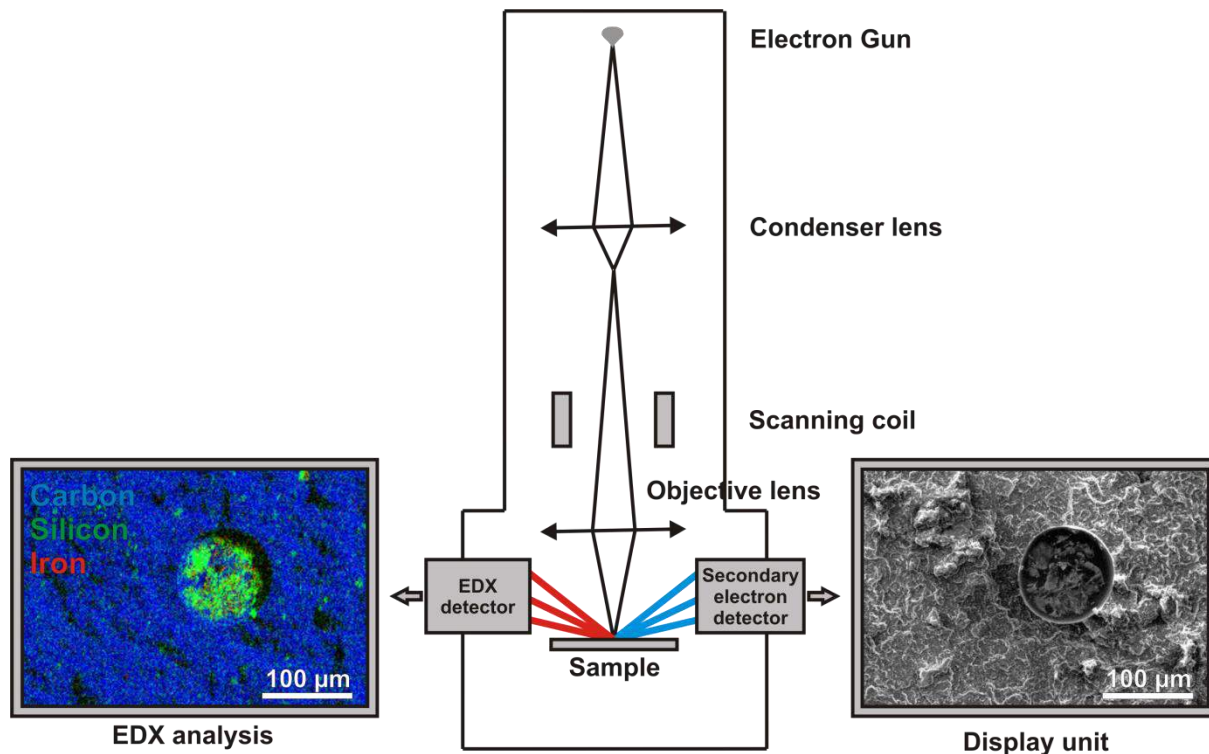


Figure 6 Schematic overview of the column of a SEM⁶⁷.

2.2 Transmission electron microscopy

2.2.1 Sample preparation

In TEM, a high-energy electron beam interacts with a specimen, through which the structure and composition of the materials can be investigated. One of the most important challenges in TEM is to use samples that are sufficiently thin to allow the transmission of electrons. Furthermore, the surface roughness of the samples should be negligible. Therefore, TEM sample preparation is often a very critical step in determining the quality and precision of the final TEM results⁶⁸. TEM samples can be prepared by a variety of techniques, including crushing, mechanical polishing, dimpling, electro polishing, ion-beam milling, and focused ion beam (FIB) milling. Among these, crushing, ion-beam milling and FIB milling are popular techniques to prepare TEM samples, which were also employed often to the materials investigated in this thesis.

Crushing

Crushing materials for TEM sample preparation is a widely used and straightforward technique. The advantage of crushing a sample is that there is a higher chance of obtaining thin regions which can be used for TEM investigation. The sample is first crushed in an agitate mortar in the presence of a solution, usually ethanol. Next, this solution is dispersed using ultrasonication in order to minimize any agglomeration of the particles. The solution is then drop-casted onto a carbon-coated copper grid (holey carbon grid). The grid is dried on a filter paper under an infrared lamp, after which it can be used for TEM investigation.

Ion-beam milling

Ion-beam milling is a sputtering process commonly used for preparing TEM samples from thin films consisting of metals, semiconductors, insulator, or even a combination of these materials. Using this technique, energetic (~ 5 keV) neutral atoms and argon ions from a cathode impinge on the disc (or target) under a small angle (~ 5 - 8°). This causes the removal of the atoms of the target, and leads to thinning of the ion beam exposed area⁶⁹. Electron transparency is obtained at the edges near this perforation. The energy and nature of the ions, the beam current, angle of incidence and nature of the sample are important parameters in controlling the thinning rate. Through this method, plan-view or cross-sectional TEM sample can be prepared, and both will be discussed briefly in the following sections.

Ion-beam milling: Plan-view sample preparation

The main steps of the plan-view sample preparation technique are schematically shown in Figure 7-(A). TEM discs (3*3 mm squares) are obtained by cutting the samples either using a diamond wire or a diamond tip pen. The discs are wax-bonded to a glass slide of a holder, where it needs to be mechanically polished. Either one or both sides of the discs can be polished until a final thickness of about ~ 30 μm is reached. Next, the material is bonded carefully on a copper grid having a single hole of about 1.5-2.0 mm hole diameter. The ion-milling is done by keeping both ion guns at the top at $\sim 5^\circ$ until an electron transparent region is obtained.

Ion-beam milling: Cross-section sample preparation

Cross-section TEM specimens are prepared by vertical polishing of the samples to obtain TEM specimens which can be imaged in cross-sectional view. The main steps of the cross-section sample preparation technique are schematically shown in Figure 7-(B). In this case, a sandwich structure is formed by gluing supporting materials (glass, Si wafer pieces, etc.) on both sides of the sample. TEM discs (3*3 mm squares) are obtained from cutting the sandwich structure by using a diamond wire. The disc from the sandwich structure is then wax-mounted to the base of the tripod polisher. The mechanical polishing and ion-milling steps are accomplished in the same manner, as explained previously for plan-view sample preparation.

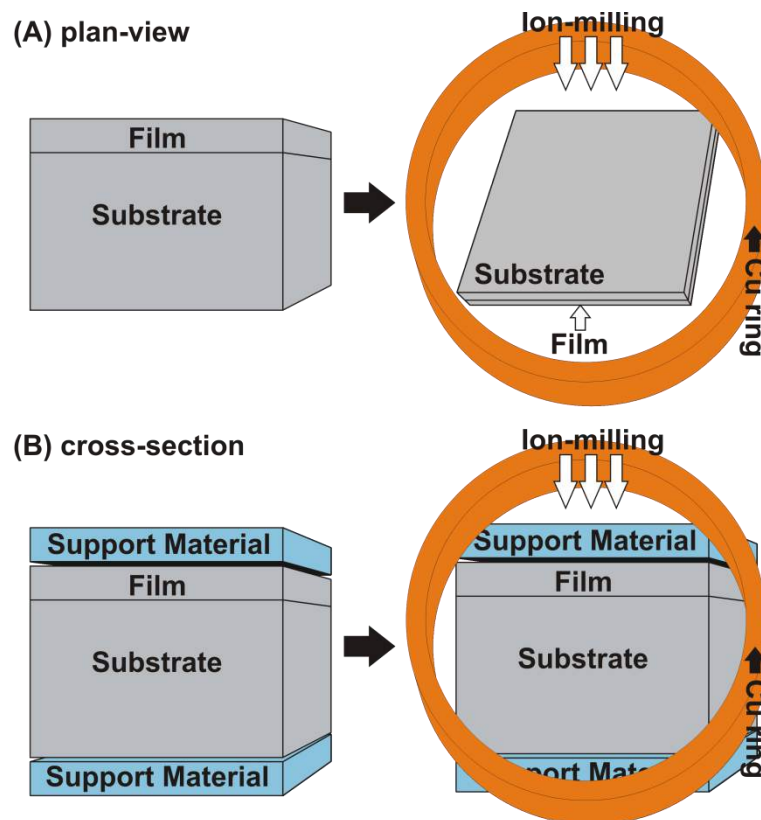


Figure 7 Schematic illustration of (A) plan-view and (B) cross-section ion milling TEM sample preparation techniques.

The combination of the two materials systems in nanomaterials promises superior performance compared to the isolated systems⁷⁰. In these materials, the interface between each component plays a key role for the final performance. Both plan-view and cross-

sectional TEM are keys to understand the structure of this interface. However, the above explained sample preparation techniques are rarely used for nanomaterials consisting of several components. This is due to several factors. For instance, the TEM sample preparation through ion-milling is time-consuming. In addition, it includes gluing of the specimen, baking the material, and the application of organic solvents such as acetone which potentially jeopardize the stability of organic materials, such as carbon⁷¹. In this thesis, it will be shown that the structure of the organic component embedded in a hybrid material system can still be preserved by conventional TEM sample preparation with final broad beam argon ion milling, and that adequate ion-milled TEM samples can be prepared from such complex material systems.

Focused-ion beam

FIB milling has been widely used in materials science to prepare TEM samples, thanks to its site-specific approach. Using FIB, it is also possible to prepare TEM lamellas from materials with complex morphologies, as will be shown in Chapter 3. Nowadays, a FIB is mostly combined with an electron and ion beam columns, yielding a so-called FIB/SEM Dual beam system, in which Ga⁺ ions are the most common FIB sources. In a dual-beam FIB system the electron column is usually vertically aligned, whereas the ion column is positioned under an angle of 52° with respect to the electron column. In addition, several other tools can be integrated into FIB, such as a gas-injection system (GIS) or a microprobe (see Figure 8-(A)). At the beginning, a Pt layer is deposited on the area where the TEM lamella is to be prepared (see Figure 8-(B)), which aims at minimizing the damages of the surface features during ion milling process. Trenches are milled around the Pt protection layer (see Figure 8-(B)), and the lamella is released from the bottom. The probe is then inserted as shown in Figure 8-(C). The micro-probe is connected to the lamella by depositing Pt. After the edge is released from the bulk by ion-milling, the lamella is picked up by the probe, as shown in inset given at Figure 8-(C). By moving the probe and the sample stage, the lamella is transferred to a TEM grid dedicated for FIB. When the attachment of the lamella to the grid is carried out by Pt deposition, the probe is released from the lamella. The lamella at this step is milled by ion beam from both sides to achieve electron transparency (see Figure 8-(D)).

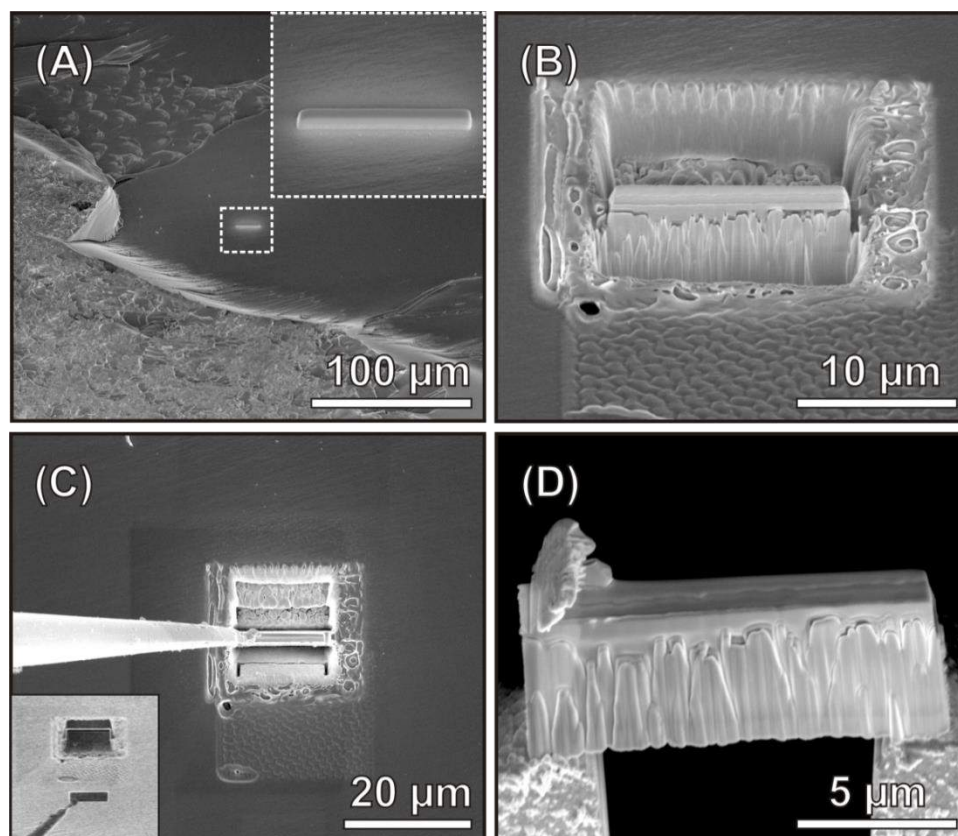


Figure 8 (A-D) SEM images depicting the main steps of FIB procedure: (A) A Pt protection layer is deposited onto the sample surface; (B) trenches are milled around the lamella; (C) the probe is attached to the lamella by Pt deposition, and then the lamella is released from the bulk (inset); (D) The lamella is attached to the grid to be milled by focused ion beam to obtain electron transparency.

2.2.2 Transmission electron microscopy techniques

TEM is a powerful tool to investigate the morphology, structure and composition of materials at the nano-scale. In general, TEM uses similar working principles as optical microscopy. For instance, an optical microscope uses light and optical lenses to magnify images of a given sample, whereas a TEM uses electrons and electromagnetic lenses. The resolution of the optical microscope is restricted by the wavelength of visible light, which prevents it from obtaining atomic-resolution imaging. In case of TEM, high energy electrons have wavelength smaller than 1 Å. This makes the attainable resolution of a TEM much better than that of an optical microscope. This comparison of resolution between an optical microscope and a TEM can be understood by the formula:

$$d = \frac{\lambda}{2n \sin \theta}$$

where n is the refractive index (which is 1 in the vacuum of an electron microscope), d is the minimum distance at which the points can be distinguished as individuals, θ is the half angle of the pencil of light that enters the objective and λ is the wavelength. Visible light ranges in wavelength from the long red waves (= 760 nm) to the short blue/violet waves (= 400 nm). Therefore, the best resolution that can be achieved by light microscopes is about 200 nm. In case of electrons, the wavelength of an electron, λ , is approximately equal to:

$$\lambda = \frac{h}{\sqrt{2meV}}$$

where h is Planck's constant (6.626×10^{-34} J seconds), m is the mass of an electron (9.1×10^{-31} kg) and e is the charge of an electron (1.6×10^{-19}) if the electrons are accelerated in an electric potential, V . By taking into account the relativistic effects the wavelength at 100 keV, 200 keV, and 300 keV operating voltages in electron microscopes can be calculated as 3.70 pm, 2.51 pm and 1.96 pm, respectively. Therefore, resolution in sub-angstrom levels is reachable with the TEM. However, in most cases the resolution is practically limited to ~ 1 Å due to several factors, such as the lens aberrations in electron microscopes, the necessity for a very thin sample, the drift and the vibrations experienced by the TEM samples during their characterization, etc.

In TEM, high energy electrons are emitted by a source (electron gun) and they are focused and magnified by a system of electromagnetic lenses. The electron beam is condensed onto the sample by the condenser lenses, which control the brightness of the beam. The condenser aperture controls the fraction of the beam which is allowed to reach the specimen. On the other side of the sample, the objective lens forms an initial image, which is subsequently magnified⁷². The interactions which occur during the collision of the electron beam with the sample will lead to (see Figure 9) backscattered electrons, secondary electrons, coherent elastic scattered electrons, incoherent inelastic electrons, incoherent elastic forward scattered electrons, characteristic and Bremsstrahlung X-rays, Auger electrons, visible and ultraviolet (UV) lights, etc. In principle all these by-products of the primary beam interaction can be used to derive information on the nature of the specimen. In order to obtain information concerning different aspects of a given specimen, a variety of TEM techniques has been developed. All the imaging and spectroscopic TEM techniques, such as HRTEM, STEM or EDX, which

were used in this thesis, are explained briefly in this section. A more extended explanation of different microscopy techniques can be found in several textbooks^{73,74}.

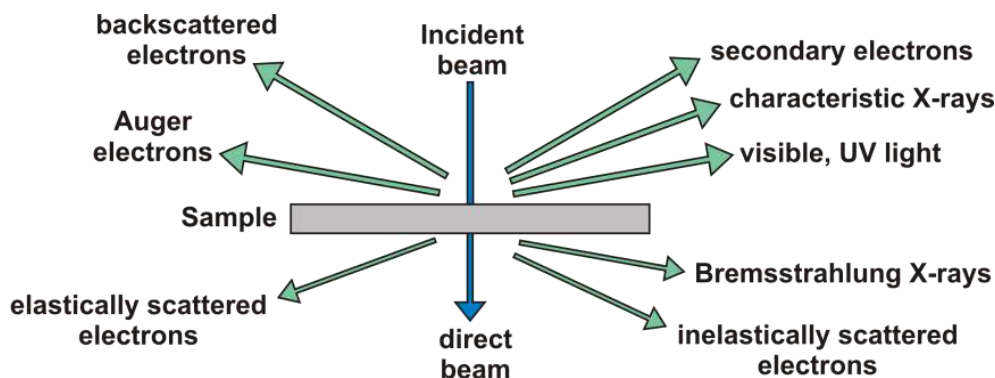


Figure 9 Overview of the signals generated when an electron beam interacts with a (relatively) thin specimen.

Bright field transmission electron microscopy

When using this method, the sample is imaged using a parallel electron beam and the image plane of the objective lens acts as the object plane for the intermediate lenses. An objective aperture with a given diameter placed in the back focal plane is typically used to select the electrons that can contribute to the image. In bright field TEM (BFTEM) imaging mode, the image contrast is influenced by several mechanisms. For example, denser areas or areas containing heavier elements appear darker due to scattering of the electrons to angles excluded by the objective aperture, which is known as mass-thickness contrast. In addition, scattering from crystal planes introduces diffraction contrast, which depends on the orientation of a crystalline area in the sample with respect to the electron beam. Due to diffraction contrast mechanism, a sample consisting of randomly oriented crystals will yield TEM images with varying contrast levels, since each crystal will have its own grey-level related to its orientation with respect to the electron beam. This enables one to distinguish different sites of a sample from each other in terms of crystallinity as well as crystal defects.

Electron diffraction

In crystalline materials, electron diffraction occurs as the electron beam is diffracted by the crystal lattice at specific angles. This will yield a diffraction pattern, which is characteristic for the studied crystalline material. The projector and intermediate lenses below the objective

lens are used to focus and magnify the diffraction pattern onto a fluorescent screen or a charge-coupled device (CCD) camera, which converts the electrons into visible light signal. The spacing between the diffraction spots in a diffraction pattern is directly linked to the interplanar distances in the crystalline material, which is governed by the Bragg's law:

$$2d \sin \theta = \lambda$$

In this formula, λ corresponds to the wavelength of the electrons, θ is the angle of incidence with respect to a set of crystallographic planes, d is the interplanar spacing of the atomic planes and constructive interference occurs when n is an integer. The angles and distances between the reflections (the values of θ and d) together with the presence or absence of certain reflections can be used to identify the crystal structure and orientation of a sample. In case of polycrystalline materials, the collection of the diffraction spots will yield rings, whose radii can also be used to identify the material investigated.

High resolution transmission electron microscopy

HRTEM is an important and widely used technique in TEM. Unlike low/medium magnification BFTEM, which employs mass-thickness or diffraction contrast, as mentioned previously, in HRTEM phase contrast is employed to show lattice fringes and atomic structures. Phase contrast occurs due to the interaction of an electron wave with thin specimens. This results in a phase shift of the electron wave due to the difference in inner potential of the material with respect to the vacuum, or of a specimen detail with respect to the surrounding matrix. As a result, a lattice image is formed. An example of a HRTEM image is given in Figure 10. From this image, the lattice fringes can be observed clearly from a crystalline TiO₂ nanoparticle. In general, phase-contrast images can be difficult to interpret since the contrast is sensitive to many factors including sample thickness, orientation, scattering factor and changes in the astigmatism and focus of the objective lens. Therefore, the lattice fringes are not direct images of the atomic structure but can give information on the lattice spacing and atomic structure of the crystal. To understand and interpret the experimental HRTEM images, image simulation is necessary. The detailed theoretical description on the formation and simulation of HRTEM images can be found in several textbooks^{73,74}.

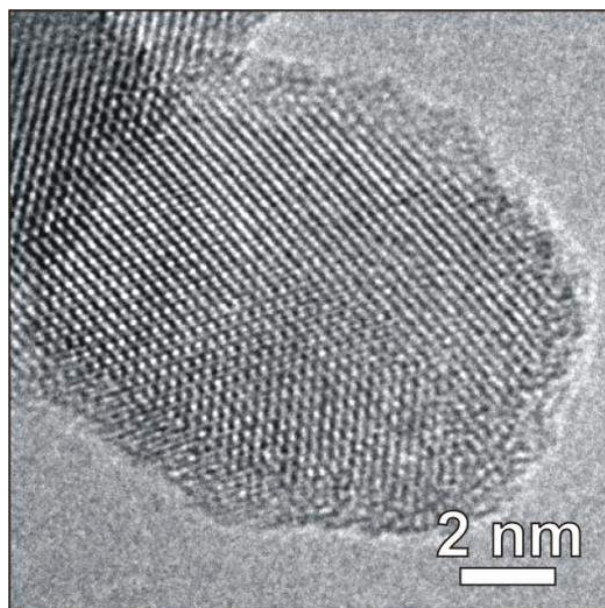


Figure 10 HRTEM image acquired from a TiO₂ nanoparticle depicts the lattice fringes.

Scanning transmission electron microscopy

Unlike TEM modes such as BFTEM and HRTEM in which a parallel electron beam is used, scanning transmission electron microscopy (STEM) mode makes use of a nano-sized probe, which is scanned across an area of interest. Upon interaction, the electrons are either transmitted through the specimen, or they interact with it. Another possibility is that they may be scattered to high angles (deflected by an angle (β)). This scattering can occur with or without a corresponding loss of energy of the electrons. The electrons that lose energy when deflected through the sample are inelastically scattered, while those that do not undergo a loss of energy are elastically scattered. In STEM imaging mode, the elastically scattered electrons are used. These electrons are scattered at an angle θ and are detected by either a bright field ($\theta < 10$ mrad) or annular dark field ($10 \text{ mrad} < \theta < 50 \text{ mrad}$) (ADF, usually a ring shaped scintillation detector to which a photomultiplier is attached) detector, as shown in Figure 11. For electrons scattered to high-angles ($\theta > 50 \text{ mrad}$), the intensity is almost proportional to the square of the atomic number, Z^2 , so that the strong chemical contrast (Z-contrast) is obtained. This type of imaging is referred to as high-angle ADF-STEM (HAADF-STEM)⁷⁵. When using HAADF-STEM mode, one of the main advantages over ADF-STEM and BF-STEM is that Bragg effects are avoided, since the HAADF detector only gathers electrons scattered to very high angles ($\theta > 50 \text{ mrad}$). Therefore, the strength of scattering is not strongly influenced

by diffraction. Often, scanning a probe in STEM mode may help to reduce specimen damage as the beam is not positioned at a specific specimen region for a long period of time⁷⁶. This was found to be quite advantageous, especially for the investigation of organic nanomaterials⁷⁷.

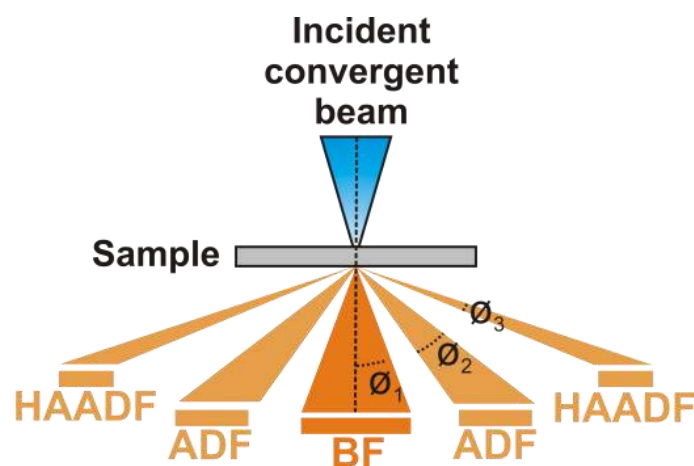


Figure 11 Scheme of the HAADF detector setup for Z-contrast imaging in a STEM.

Energy dispersive X-ray spectroscopy

The chemical investigation of a sample can be performed by the analysis of X-rays that are formed as a result of the interaction between the electrons and the sample. This technique is referred to as EDX. Through the combination of TEM imaging modes such as BFTEM or STEM with EDX, the presence of elements with atomic numbers between 4 (Be) and 92 (U) can be analysed and mapped. Especially the combination of EDX and HAADF-STEM imaging is nowadays widely performed. For instance, EDX-STEM can allow the identification of the coating materials deposited onto CNSs and CNTs templates with a site-specific approach, as will be shown in Part II of this thesis.

EDX analysis using a traditional single detector designs based on Si(Li) or SDD detectors has become a routine application. However, these detector systems usually suffer from the low collection efficiency of X-rays. To overcome this, the beam needs to be positioned on specimen regions for a relatively long time to obtain a significant signal-to-noise level (usually in the order of a few seconds at each pixel). This could result in specimen damage and become problematic, especially during the characterization of carbonaceous nanomaterials, which are prone to such electron beam induced damages.

Recently, a new EDX detector system (ChemiSTEM SuperX, FEI Company) was introduced⁷⁸. In this system, there are four silicon-drift detectors placed symmetrically around the specimen in a specially designed objective lens⁷⁸ (see Figure 12). Chemical mapping with this new type of detector system resolves many of the current problems of EDX analysis and enables the acquisition of chemical maps of many elements at high count rates⁷⁸. Since EDX maps can now be obtained using much smaller acquisition times, HAADF-STEM tomography can also be coupled with EDX. In this manner, 3D chemical analysis of nanomaterials becomes possible. An application of EDX-STEM tomography will be presented and discussed in Chapter 3.

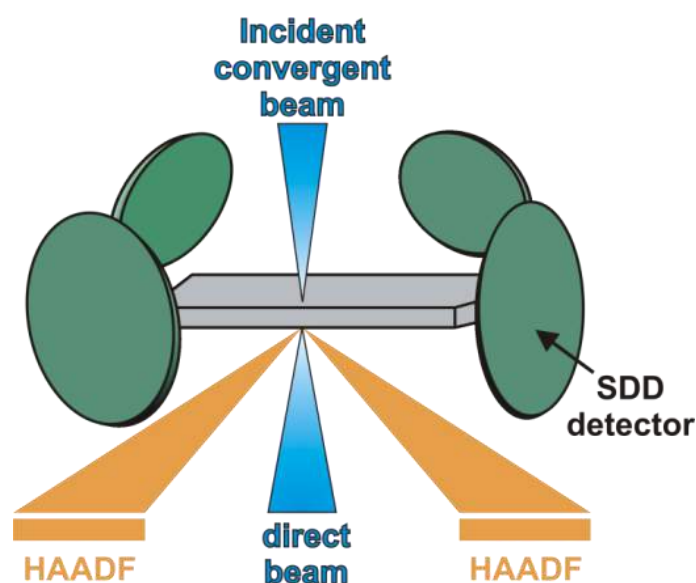


Figure 12 A schematic of the symmetrically arranged four EDX detectors around the specimen

Electron energy-loss spectroscopy

Electron energy-loss spectroscopy (EELS) is a TEM method, which measures the amount of inelastic energy lost by the electrons due to their interaction with the sample⁷⁹. The amount of the lost energy yields information concerning the composition and chemical properties of the investigated sample. For EELS, TEM should be equipped with a spectrometer either integrated into the column (in-column filter) or mounted under the projection chamber (post-column filter). Electrons which enter the spectrometer after their interaction with the sample are dispersed by a magnetic prism according to the amount of energy they lost in the scattering process⁸⁰. With an increasing electron energy loss, the deflection angle of the

electrons increases (see Figure 13). In this manner, a spectrum can be acquired. This spectrum consists of zero-loss, low-loss and core-loss regions. The first peak, which is observed at 0 eV, is referred to as zero-loss peak and it arises from the electrons that are transmitted without suffering a measurable energy loss. The low-loss region of an EELS spectrum, extending from 0 to ~50eV, corresponds to the excitation of electrons in the outermost atomic orbitals. The main contribution to the low-loss region stems from plasmon oscillations of the valence electrons. The high-loss (core-loss) portion of an EELS spectrum above ~50 eV contains information from inelastic interactions with the inner or core shells, providing chemical information from the more tightly bound, core-shell electrons and contains details about the bonding and atomic distribution.

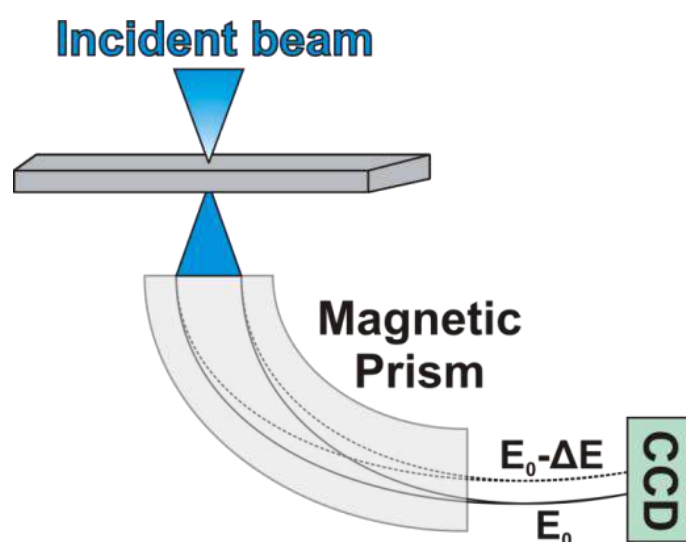


Figure 13 Schematic diagram showing the key components of electron energy-loss spectrometer⁸⁰.

EELS combined with STEM is nowadays used to detect single atoms, produce elemental maps with atomic resolution and explore the nature of the atomic bonds in many types of materials⁸¹. In this approach, either a line spectrum or a 2D spectrum image can be acquired. The EELS energy resolution that can be attained at medium primary voltages (100–300 kV) is approximately 0.1–0.5 eV with the use of monochromators.

Energy-filtered transmission electron microscopy

The most straightforward approach for elemental mapping by EELS is through the use of energy filtered transmission electron microscopy (EFTEM). In EFTEM, the parallel beam

imaging mode in TEM is coupled with the principles of EELS⁸², and the elemental mapping of different elements can be obtained using the energy-loss electron contributing to their ionization edges. Elemental mapping requires one or two pre-edge images and a post-edge image acquired for each element in the two-window or three window methods. The three-window method is more advantageous than the two-window method in the sense that it records two pre-edge images instead of one at a slightly different energy loss and determines the background at each pixel. Next, the background is fitted according to an inverse power law at each pixel in the two pre-edge images. The elemental map is finally generated by subtracting an extrapolated background from the post-edge image, which gives an accurate elemental map. This image can be used to estimate the concentration of a given element. An example of an EFTEM elemental map depicting the carbon and titanium contents of the nanosheets is presented in Figure 14.

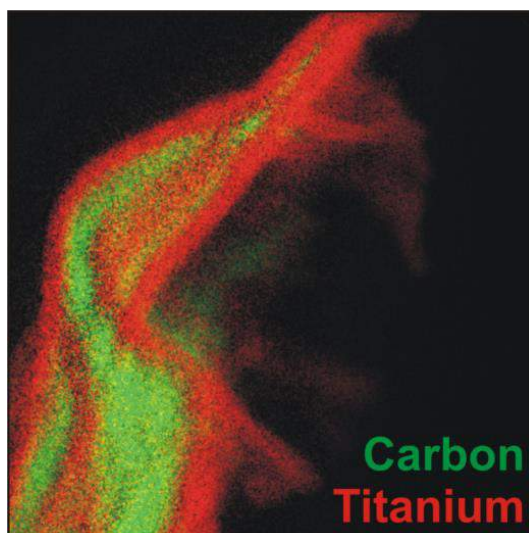


Figure 14 Carbon and titanium contents of the nanosheets are presented in the color-coded EFTEM elemental map.

Electron tomography

TEM is a very useful technique to determine the structure, morphology and composition of nanoparticles both in a qualitative and quantitative manner. However, one should never forget that the technique only provides 2D projections of a 3D object. This problem can be overcome by combining TEM with tomography, leading to electron tomography. Electron tomography

is a method which allows obtaining information from the interior as well as the exterior of a specimen using its 2D projections.

The initial step in an electron tomography experiment is to acquire a series of images of a sample recorded at different tilt angles. These images can be collected using different TEM modes. For instance, BFTEM and HAADF-STEM tomography are commonly performed in materials science to obtain the 3D morphologies of the nanomaterials. However, tomographic reconstruction is based on the assumption that the images acquired are ‘true projections of structure’. In other words, the intensity in the images must show, at least, a monotonic relationship with some function of the thickness or density of the structure⁸³. This requirement is known as the “projection requirement”⁸⁴. In particular, dynamic diffraction in crystalline materials violates the projection requirement in BFTEM images, since image intensities no longer increase monotonically with sample thickness⁸⁵ due to the diffraction contrast. As a result, for most crystalline samples in the physical sciences, HAADF-STEM tomography is preferred over BFTEM tomography.

During the acquisition of a tilt series, projections are recorded every few degrees by tilting the specimen over a certain angular range. Preferably, this angular step size is as small as possible. However, for beam sensitive samples the step size is often increased to minimize the total acquisition time and thus to reduce electron beam damage. On the other hand, the use of larger step sizes reduces the quality of the reconstruction. Another bottleneck during tilt series acquisition is the limited tilt range of the specimen because of the narrow spacing in between the pole pieces of the objective lens in TEM. Moreover, shadowing of the specimen can occur, which is caused by the edge of the holder or the clamping mechanism at high tilt angles in the direction of tilt. In order to overcome these limitations, dedicated tomography holders were fabricated. The widths of these holders were reduced (<1 mm) in order to enlarge the tilt range of up to 80° without the shadowing effects.

The angular range which is not sampled in a tilt series is the so-called “missing wedge” (see Figure 15). The missing wedge will lead to artefacts in the final 3D reconstruction that are referred to as “missing wedge artifacts”. The most apparent artefact corresponds to image features that are elongated in the direction parallel to the electron beam⁸⁶. Therefore, one

should be very careful in interpreting the results of a tomographic reconstruction based on an incomplete tilt series.

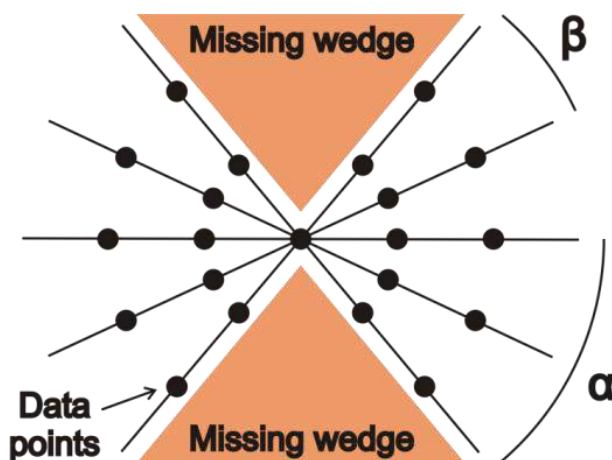


Figure 15 Representation in Fourier space of the ensemble of projections, indicating the missing wedge of information brought about by a restricted tilt range. β is the tilt increment between successive images and α is the maximum tilt angle⁸⁷.

After the tilt series is acquired, the projection images should be aligned with respect to each other⁸⁸. In the alignment stage, the individual images need to be shifted onto a common tilt axis, requiring both spatial (x - y) and rotational (θ) shifts⁸³. The most popular method being used to align tomography series is the cross-correlation alignment⁸⁹. Using this method, central peaks in Fourier Transforms of two subsequent projections are cross-correlated. Cross-correlation to correct for shift and rotation is performed along each axis in turns iteratively until the best fit is found between the central peaks of two adjacent Fourier Transforms. The advantage of cross-correlation is that it is a relatively simple and fast procedure, and that no pre-treatment of the specimen (e.g. application of nanogold clusters on the specimen surface to be used as fiducial markers) is required⁹⁰.

3D reconstruction is typically carried out using one of the widely accepted algorithms, such as weighted-back projection (WBP) or the simultaneous iterative reconstruction technique (SIRT). WBP assumes that the projection images represent the amount of mass density encountered by imaging rays. The method simply distributes specimen mass evenly over computed backprojection rays. When this process is repeated for all the projection images in the tilt-series, backprojection rays from the different images intersect and reinforce each other at the points where the mass is found in the original structure. In this manner, the 3D structure

of the specimen is reconstructed from a series of 2D projection images⁹¹. The disadvantage of WBP is its sensitivity to the limited tilt angle and noise. In order to overcome this limitation and improve the reconstruction, an iterative reconstruction algorithm is proposed, i.e. SIRT⁹². When using SIRT, starting from an initial estimate of the sample, the current estimate is refined in each iteration by reducing the distance between the measured TEM projection data and the projection data simulated from the current estimate⁹³. This process will continue iteratively until the re-projections from the final reconstruction converge to the original projections. A previous study has shown that after 30 iterations in SIRT, the numerical resolutions for two tomographic measurements are very much similar⁹⁴. Further details about SIRT can be found in⁹².

The reconstructed datasets of electron tomography require advanced software tools for the analysis and the visualization. Similar to 2D projections where each pixel has a grey level, in a 3D reconstruction the basic unit for visualization is referred to as a “voxel”. Each voxel has dimensions of 1 pixel at each edge of the cube and also has a grey level. The interpretation of the reconstruction is based on the correspondence between different grey levels in the reconstruction and different compositions in the original structure. The voxels of the reconstructed volume must be assigned to different classes, corresponding to the different compositions in the sample. This process is referred to as “segmentation” and is commonly performed either by thresholding or by manual selection. In case of the former, segmentation may become impossible for the cases where the grey levels of the components of nanomaterial are too close to each other. In such cases, manual segmentation becomes an option, keeping in mind that it can be time consuming and moreover subjective. More advanced reconstruction algorithms have therefore been proposed in which segmentation is part of the reconstruction process⁹⁵.

2.3 Transmission electron microscopy of materials comprising CNSs and CNTs

In the past, materials consisting of different components have been characterized by a variety of techniques, and often TEM has often considered as a very useful one. Previous studies have shown that TEM can be performed to determine size, distribution and composition of the

components from hybrid material systems^{59,60,96–99}, to identify and characterize any defects^{5,59,100}, and to understand the failure mechanisms involved in the composites as a whole¹⁰¹, or in the matrix and reinforcements¹⁰² individually. Moreover, TEM has been used to gain information on the degree of bonding between different components, and to relate those to the properties observed from the overall structures. It is obvious that TEM and associated techniques are tremendously powerful characterization tools when used to investigate materials. However, it should also be taken into account that despite all its advantages, there are some limitations to the resolving power of a TEM.

The basic limit to the resolution of a TEM is determined by the quality of the lenses¹⁰³, which are prone to aberrations that need to be corrected for. Nowadays, these aberrations could be reduced by spherical aberration correctors, such as STEM probe correctors and TEM image correctors, built especially for TEM. During the last decade, a rapid development and implementation of aberration correction in electron optics took place, which enabled sub-angstrom spatial resolutions. As an example, Figure 16 shows an aberration corrected high resolution HAADF-STEM image obtained at 120 kV from a single crystalline Si wafer which was used as substrate for the growth of CNSs and CNTs. From the image, it can be seen that an interplanar spacing of 0.136 nm can easily be distinguished with this technique.

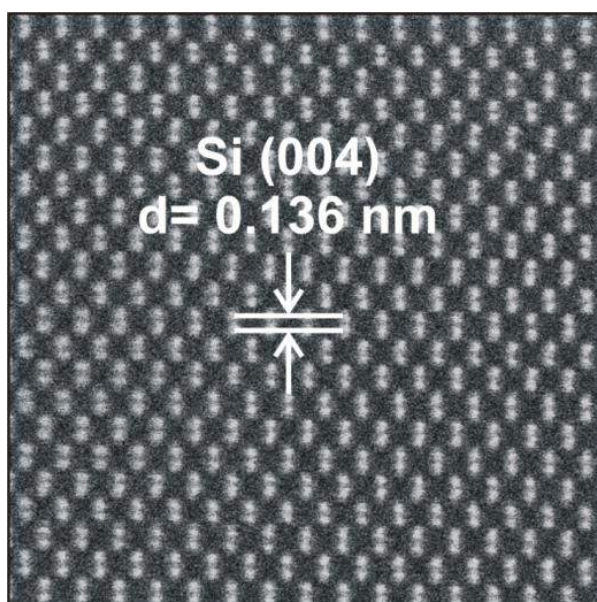


Figure 16 Aberration-corrected HAADF-STEM of single crystalline Si wafer. Bright dots correspond to the projections of columns of Si atoms.

High resolution imaging is commonly performed in both TEM and STEM modes to study CNSs and CNTs materials. For these materials, low-voltage HRTEM and STEM are attractive, since CNSs and CNTs are sensitive to beam damage via the knock-on process. Knock-on damage arises from the high-angle elastic scattering (deflection by the electrostatic field of atomic nuclei), which can transfer several eV of energy from an incident electron directly to a nucleus and results in the displacement of an atom from a crystal or from the surface¹⁰⁴. For SWCNTs, the threshold for knock-on damage has been determined both experimentally and theoretically to be 80kV¹⁰⁵. Therefore, by using low-voltage HRTEM or STEM, knock-on damage can be reduced or avoided¹⁰⁴. Taking this into account, an increasing number of researchers are using low operating voltages to stay below the threshold value to avoid the knock-on damage. However, the characterization of materials consisting of metals/metal oxides and CNSs/CNTs require resolving the atomic structures of both components. Consequently, depending on the materials characterized and the purpose of the investigation, a compromise needs to be made on the knock-on damage at carbon containing components by using medium and high-voltages. As mentioned previously, Figure 16 shows an example of an aberration corrected high resolution HAADF-STEM image obtained at 120 kV. In this example, it can be seen that the combination of aberration corrected STEM imaging with a medium ranged high-voltage value can be sufficient to yield the atomic columns of Si, which highlights the excellent image resolution of the combined technique. In this thesis, HRTEM and STEM characterizations were conducted to comment on the structure of as-grown CNSs/CNTs and to observe the crystallinity of the ALD processed layers. It will be hereby shown that both low and medium/high voltages are used depending on the necessary information to be obtained from the samples.

Combining aberration correction, HAADF-STEM imaging and low and medium voltage operation modes is proving to be a powerful characterization tool for materials comprising carbonaceous species¹⁰⁴. In this thesis, HAADF-STEM imaging accompanied with aberration correction is performed for atomic-resolution imaging, and HAADF-STEM accompanied with spectroscopy techniques, such as EELS and EDX, is used to obtain spatially resolved chemical characterizations. In addition, HAADF-STEM imaging is hereby preferred when acquiring tilt series for electron tomography experiments, both solitarily or combined with EDX, which is referred to as EDX-STEM tomography¹⁰⁶. This is mainly due to the fact that in

HAADF-STEM imaging, the effects arising from the diffraction contrast and specimen damage during long exposure time of an electron tomography experiment are reduced, as mentioned previously. Furthermore, the technique enables the acquisition of EDX elemental maps from any specified region within the sample.

PART I STRUCTURAL
CHARACTERIZATION OF ALIGNED
CARBON NANOTUBE BUNDLES
SYNTHESIZED THROUGH POROUS
MEMBRANES

Part I: Introduction

CNTs can nowadays be spun into fibers of several meters^{64,65}. However, the strength of fibers produced by these methods is significantly reduced when compared to individual CNTs (1-2 orders of magnitude). So far, great attention has been paid to the field of fabrication methods capable of producing long CNTs fibers with a high strength. An effective approach is based on template growth, in which CNTs are directly formed inside the pores of a self-organized template. In this respect, two types of templates can be used, which are anodized alumina (AAO) membranes and mesoporous silica. An advantage of using AAO membranes is that the alignment of the CNTs can be obtained during their synthesis in the direction of the gas flow through the large membrane pores. In Chapter 3 of this work, it will be demonstrated by TEM characterizations that for the first time, well aligned CNT bundles (aCNTb's) were directly grown through AAO membranes by means of the catalytic CVD technique (at the KU Leuven by the department of materials engineering (MTM) group (Prof. Mario Seo)).

In catalytic CVD, there are many different parameters that can affect the quality and growth of the CNTs. One of these parameters is the choice of the catalysts. In the past, numerous studies have been performed to select the ideal catalyst for the CNT growth, including Fe, Ni, Co or binary systems¹⁰⁷⁻¹¹⁰. Selecting the proper catalyst is quite important, since these catalyst particles would essentially initiate the nanotube growth¹⁰⁸, which in return affects the yield of the carbon deposit. A study on the use of a binary system of Fe-Ni catalysts for CNT growth has shown that the compound Fe₂Ni is one of the most efficient catalysts¹¹¹. Another important parameter that can change the quality and growth of CNTs is the choice of the precursor. The most commonly used CNT precursors are methane (CH₄), ethylene (C₂H₄), acetylene (C₂H₂), benzene (C₆H₆), xylene (C₈H₁₀) and carbon monoxide (CO). It was found that all these hydrocarbons permit the generation of high quality CNTs, provided that optimal catalysts and conditions were used¹¹². There are also other parameters, such as the growth temperature, carrier gas and gas flow rate, which are involved in the growth of CNTs. The effects of these parameters were also studied and can be found in earlier reports⁴⁶.

In this thesis, we investigated aCNTb's, which were synthesized through the pores of AAO membranes by means of CCVD (at the KU Leuven by MTM group (Prof. Mario Seo)).

Commercial AAO membranes (Whatman®) were used with diameters of 13 mm and a thickness of 60 μm together with pore diameter of 20 nm at their filter-side. SEM images of the back- and filter-sides of a membrane are presented in Figure 17. A set of these membranes was directly used for catalyst impregnation. Another set is prepared by first etching in NaOH prior to catalyst impregnation in order to investigate the effects of etching on the adhesion of the catalyst particles onto the walls of AAO membranes. Subsequently, Fe_2Ni catalysts were deposited by impregnation.

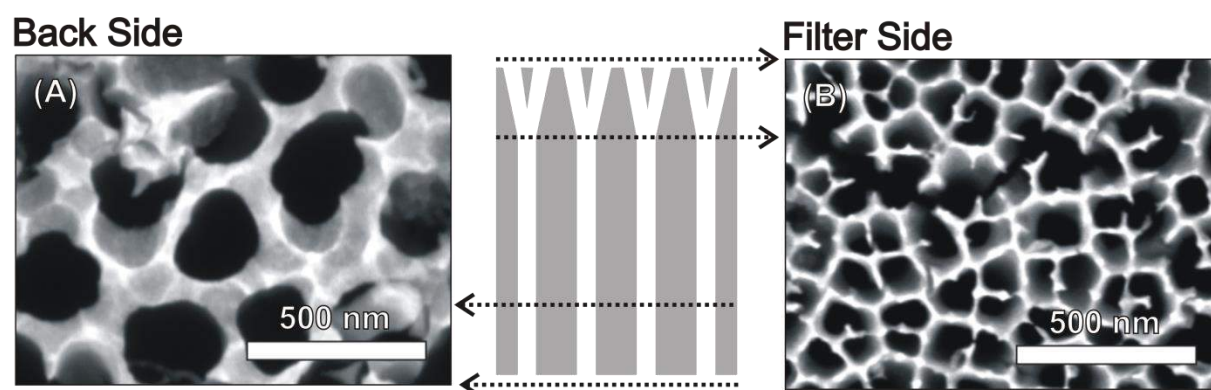


Figure 17 SEM images of (A) the back- and (B) the filter-sides of the membranes with ~ 20 nm pores.

For CNT growth, the AAO membranes containing the Fe_2Ni catalyst nanoparticles were inserted into the CVD reactor with the pores parallel to the precursor gas direction (see Figure 18). Subsequently, the heating temperature was adjusted to 730°C , and the flows of acetylene and Ar_2 carrier were initiated, which allowed the growth of CNTs in the cylindrical pores of AAO template. More details on the catalytic CVD process will be given in Chapter 3.

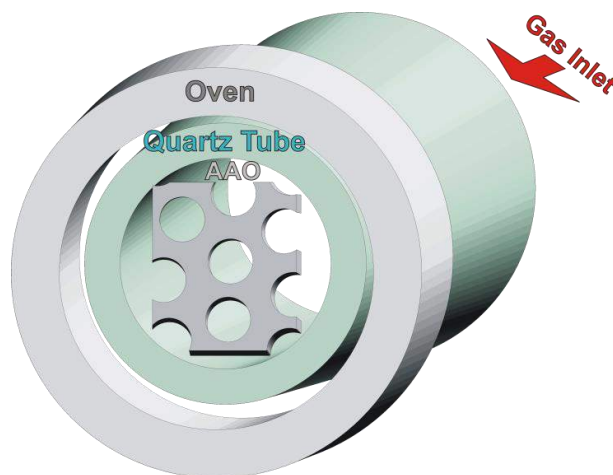


Figure 18 Schematic representation of CVD of CNTs inside AAO pores.

As mentioned previously, mesoporous silica materials can also be used as templates for the CNT growth. These materials already attracted considerable attention during the last decade because of their promising applications in many fields^{113,114}. A main challenge here is to synthesize 1-Dimensional (1D) mesoporous silica with ordered and vertical nanochannel structures because of their potential applications such as templates to grow functionalized ultrafine nanowire arrays^{115,116}. In this respect, an interesting pore ordering is the hexagonal columnar ordering (P6m symmetry), as observed in MCM-41 and SBA-15, in which the mesopores of silica are accessible from the surface¹¹⁷⁻¹¹⁹. In order to synthesize mesoporous silica with a hexagonal columnar ordering, a template method was widely adopted¹²⁰. Compared to other templates, AAO membranes are preferred due to their orderly arranged and vertical 1D channel structure. Previously, several research groups have synthesized mesoporous silica confined in the pores of the AAO templates^{117,121-123}. An alternative approach to produce these materials is the combination of soft and hard template methods¹¹⁷: Ordered mesoporous silica is formed inside the macropores of AAO membranes via the soft templated synthesis of silica through the evaporation induced self-assembly (EISA) method. In general, the EISA technique has proven itself to be useful^{117,121,122}. However, studies on the soft template part have shown that the parameters in the EISA process have great influence on the observed pore ordering of silica and that these parameters need to be optimized in order to preferentially obtain the hexagonal columnar ordering^{117,121,124-129}. Once such ordering is obtained, the idea of using AAO membranes directly as templates for the CNT growth can be extended by introducing mesoporous silica into a 1D channel structure of the AAO template and allowing the CNT growth through the mesopores of silica material (see Figure 19). It is however of crucial importance that the EISA process is optimized in such a manner that the desired pore architecture (hexagonal columnar ordering) of mesoporous silica is obtained.

In this thesis, we characterized mesoporous silica materials, synthesized inside the pores of AAO membranes by means of EISA (at KU Leuven by Dr. Filip de Clippel, Drs. Roel Locus and Prof. Bert Sels). Commercial AAO membranes were obtained from Whatman® anodisc membrane discs with diameters of 13 and 47 mm and a thickness of 60 μm . The minimum pore size of the AAO membranes was 200 nm at the filter-side (a top layer of few microns) and the back-side of the membranes contained pore diameters of about 300 nm. The EISA-

solutions were prepared, as reportedly in the literature¹²². More details on the experimental procedures of the EISA process will be given in Chapter 4.



Figure 19 Schematic representation of CVD of CNTs inside silica pores.

Chapter 3 TRANSMISSION ELECTRON

MICROSCOPY STUDY OF ALIGNED CARBON NANOTUBE BUNDLES SYNTHESIZED THROUGH ANODIZED ALUMINA MEMBRANE PORES

CONTENTS

CHAPTER 3 TRANSMISSION ELECTRON MICROSCOPY STUDY OF ALIGNED CARBON NANOTUBE BUNDLES SYNTHESIZED THROUGH ANODIZED ALUMINA MEMBRANE PORES	45
3.1 INTRODUCTION	45
3.2 EXPERIMENTAL DETAILS.....	47
<i>Synthesis of aligned carbon nanotube bundles</i>	47
<i>Characterization techniques</i>	48
3.3 RESULTS.....	50
3.4 DISCUSSION.....	56
3.5 CONCLUSIONS.....	59

Chapter 3 Transmission electron microscopy study of aligned carbon nanotube bundles synthesized through anodized alumina membrane pores

In this chapter, the structural characterization of aCNTb's grown through AAO membrane pores by catalytic CVD is presented. AAO template assisted and catalytic CVD based synthesis of CNTs enables the production of aCNTb's with several micrometers in length. Through this approach, the bundling of the CNTs takes places already during the synthesis, which has the potential to produce highly aligned CNT bundles with high density in one process that can be scaled up for industrial applications. TEM indicates that the AAO membrane pre-etching is here an important step in order to improve the attachment of the catalyst particles on the membrane side walls, which in return promotes the root growth process involved in the formation of individual CNTs of the bundles.

3.1 Introduction

The growth of CNT arrays has been realized on various substrates. Early studies reported the use of AAO as a template by taking advantage of its well-ordered, vertical and 1D channel structure^{59,130-133}. Especially the possibility to achieve precise control over the diameter, structure and length of AAO-CNTs has motivated this research. In general, two different types of AAO-templates can be used for CNT growth: free-standing AAO-templates with both ends open, or AAO-templates with one end open and the other closed, which remain attached to a substrate. The growth of CNTs using the latter AAO-templates (namely one-side-open) mainly involves the deposition of a catalyst into the bottom of the template channel. Owing to the catalytic pyrolysis of hydrocarbon, a CNT gets deposited into each pore. However, this growth of CNT is based on the deposition of carbon atoms that graphitize on the pore wall⁵⁹. The diameter of the CNT and the number of walls can be controlled by the selection of the AAO pore diameter and the precise growth condition, respectively. Alternatively, CNTs can be grown catalyzed from the catalyst surface leading to dense CNTs growing out of each pores^{134,135}.

In contrast, the use of free-standing AAO-templates with two sides open allows the reactive gas accessing the whole surface of the AAO pores and enables the growth of CNTs packed

into a tidy array with uniform lengths^{136,137} as well as multi-branched CNTs. The analysis of the structural features of these revealed that the branches point in the same direction of the film growth¹³⁶. The use of free-standing AAO-templates can also be advantageous for the continuous and large scale productions of CNTs, since the catalyst can fully be reached by the reaction gas as;

- (i) the gas entering direction differs from that of outgoing and
- (ii) the channel orientation is parallel with the gas flow.

Moreover, through these advantages, the use of free-standing AAO-templates offers a solution to the problems observed at the other traditional methods, which benefit from the use of plain substrates for the growth of CNTs forests (see Figure 20-(A)) with their surface parallel to the gas flow direction. In such cases, the length of the synthesized CNTs is limited due to the obstruction of the precursor gas as a result of the as-grown CNTs, which block the diffusion of the excess precursor gas. In our method, such problem was overcome by means of the arrangement of the AAO membrane pores being parallel to the gas flow direction. Even in the case of thick CNTs growth, catalyst particles remain accessible to the reaction gas as the CNTs growth will follow the flow direction (see Figure 20-(B)). This is the novel idea of the SIM-Nanoforce-SBO3 project, which has not been realized by any other research group in the world.

In this respect, we present here a systematic investigation to optimize this new CNTs growth process, which succeeded to grow high density of aCNTb's with ultra-long length. A CNT bundle is here referred to as an overall structure comprising several individual CNTs formed within each pore of AAO membranes (see Figure 20-(B)). The method is based on catalytic CVD. Prior to CVD, the free-standing AAO membranes are etched in NaOH in order to enhance the adhesion of the Fe₂Ni catalyst particles. The effect of AAO pre-etching on the interaction between the catalysts and the membrane is investigated by TEM. Furthermore, instead of placing the catalyst impregnated AAO-template into CVD reactor horizontally with its pores perpendicular to the gas flow direction, the AAO-template is placed vertically, so that the precursor passes through each and every pore of the AAO-template and the CNT growth initiates inside these pores. This is quite advantageous towards the use of free-standing AAO-templates for the CNT growth in continuous and large scale productions. In this

manner, multiple individual CNTs are aimed to be grown inside each of the pores of the AAO membrane, which then form with each other bundles following in their alignments the same direction with the gas flow. TEM is hereby used to demonstrate the growth of aCNTb's and to reveal which type of the growth mechanism is dominant for the individual CNTs.

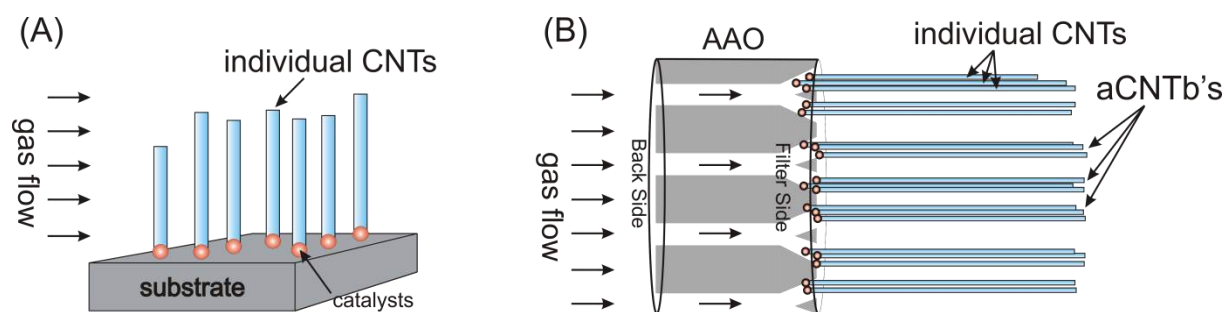


Figure 20 The schematic overviews of the growth mechanism by (A) traditional and (B) our proposed growth process.

3.2 Experimental details

Synthesis of aligned carbon nanotube bundles

As a starting material, commercially available AAO membranes (Whatman®) with pore diameters of 20 nm at their filter sides were used (see Figure 21-(A)). SEM images of these membranes were already presented in Figure 17. Although AAO membranes with larger pores can also be used, AAOs with small pore diameters are preferred, yielding CNT bundles with higher overall density at the membranes. Prior to catalyst nanoparticle impregnation, these membranes were cleaned in distilled water to remove any impurities present at their surface.

A set of these AAO membranes were directly used for catalyst impregnation, and another set was prepared by first etching in NaOH solution upon cleaning (~10 minutes) and then washing thoroughly with distilled water. Since two sets of membranes were obtained (with or without NaOH etching), the effects of etching on the adhesion of the catalyst particles onto the walls of AAO membrane pores can be investigated.

Subsequently, Fe₂Ni nanoparticles were deposited on the inner wall of the AAO template pores by impregnation. This process was accomplished by immersing the AAO membranes into a catalyst containing solution (Fe:Ni 2:1 0.2 M in ethanol) and keeping them at 4°C during 8h. To avoid the deposition of catalyst particles at the back-side (see Figure 21-(B)),

the membranes were placed in a beaker with back-sides facing the beaker bottom during the impregnation. After this step, the membranes were placed in an oven and dried at 120°C during 2h for the adhesion of the catalyst particles and the evaporation of the excess catalyst solution. Finally, the membranes were annealed during 10 min in Ar/H₂ at 700°C.

The catalyst containing AAO membranes were inserted into the quartz tube CVD reactor with back-side facing the incoming reaction gas and the pores parallel to the gas direction in the reactor (see Figure 21-(C)). Subsequently, the heating temperature was adjusted to 730°C, and a flow of acetylene was initiated at 20 mL/min and Ar₂ carrier gas at 600mL/min. This step allowed the growth of CNTs in the cylindrical pores of AAO template by deposition of carbon atoms from decomposition of acetylene. After deposition, the acetylene and Ar₂ flows were terminated, then the heating was turned off and the reactor was cooled to room temperature.

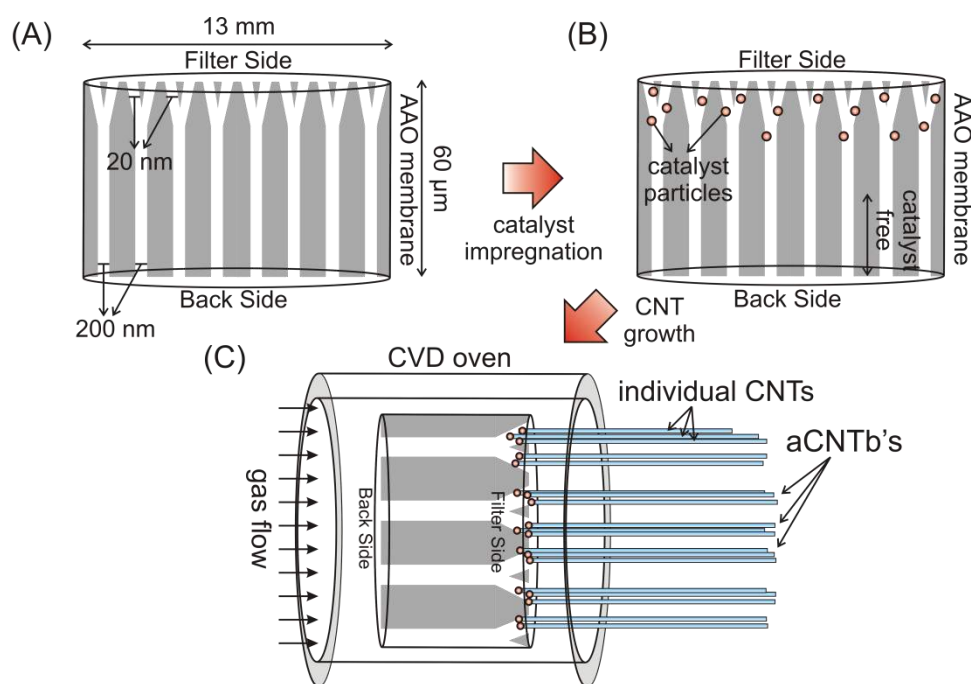


Figure 21 The dimensions of the AAO membrane are schematically presented in (A). (B) Fe₂Ni catalyst particles are impregnated into AAO membranes. (C) AAO membranes were placed into CVD reactor with AAO pores parallel to the precursor gas flow direction.

Characterization techniques

In order to resolve the surface morphology of the membranes and to observe the effects of pre-etching upon catalyst impregnation, the samples were first investigated using a SEM (FEI Quanta) operated at 10 kV. For TEM investigation, cross-section and plan-view samples were

prepared from the membranes prior to catalytic CVD of CNTs. The details of both cross-section and plan-view TEM sample preparation techniques can be found in Section 2.2.1. In addition, FIB lamella was prepared from the AAO-CNTs sample after catalytic CVD. The main steps of FIB lamella preparation can also be found in Section 2.2.1.

BFTEM, HAADF-STEM, electron tomography and EDX elemental mapping were performed using a FEI Tecnai Osiris operated at 200 kV. Tilt series for electron tomography was acquired by collecting HAADF-STEM images with tilt increments of 2° over a range of $\pm 70^\circ$ on cross-section TEM samples using an advanced tomography holder from Fischione Instruments. Automated acquisition, alignment and reconstruction of the data using the SIRT were carried out through the FEI Inspect3D software package. Amira (Visage Imaging GmbH) was used for the visualization of the reconstructed volume.

For EDX-STEM tomography experiments, an aberration corrected cubed FEI Titan microscope was used for acquiring EDX elemental maps and simultaneous HAADF-STEM imaging operated at 200 kV, equipped with a Super-X detector for EDX analysis and an advanced tomography holder from Fischione Instruments (Model 2020). HAADF-STEM images were recorded using convergence semi-angles in the range of 21–25 mrad with a probe size of approximately 1 Å. The material system in our study consists of constitutional elements such as C, O, Al, Fe and Ni with atomic numbers (Z) of 6, 8, 13, 26 and 28, respectively. The elemental mappings of these elements were obtained by scanning of individual frames of same location and summing multiple frames with varying dwell times for different tilt angles. Data acquisition consisted of a STEM tomography procedure where each 256×256 pixel EM was acquired on cross-section TEM sample for changing collection times using Bruker Esprit™ software together with simultaneous HAADF-STEM images. The elemental maps were hereby acquired at beam current of 0.2 nA. The total acquisition time was ~ 4 h which is the total duration for simultaneous HAADF-STEM and EDX-STEM tilt series acquisition including the tracking/focusing. Each tomography tilt series consisted of 29 HAADF images and EDX elemental maps acquired at the tilt range of $\pm 70^\circ$ and tilt increment of 5° . Alignment of the data was carried out using a cross correlation method for image shift and tilt alignments through the FEI Inspect3D software package. The reconstruction was

performed using SIRT with 25 iterations implemented in FEI Inspect3D. Amira (Visage Imaging GmbH) was used for visualization of the reconstructed volume.

3.3 Results

Representative TEM images from plan-view and cross-section TEM samples of the AAO membrane are presented in Figure 22-(A) and (B). From the images, it can be seen that the AAO membrane has highly-oriented porous structure with very uniform and nearly parallel pores.

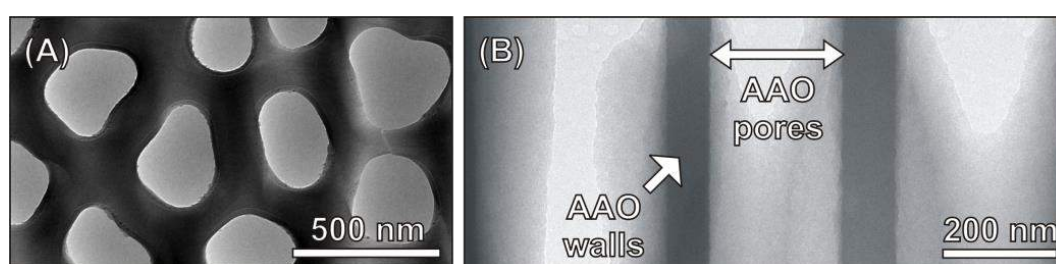


Figure 22 TEM images of the back-side of AAO from (A) plan-view and (B) cross-section samples.

As mentioned previously, a set of AAO membranes were directly used for catalyst deposition, and another set was first exposed to NaOH etching whether to observe any improvements in the adhesion characteristics of the catalysts with the membranes. Figure 23 shows SEM images of these AAO membranes after the catalyst deposition. These images reveal that the NaOH etching process did not lead to the dissolution of the membrane. From the images, it is also observed that the filter-side of the AAO membrane (20 nm pore diameter) with standard cleaning subsequent to catalyst impregnation is almost completely covered by the catalyst solution, and that the pores of AAO membrane are not visible (see Figure 23-(A)). On the other hand, the back-side of this membrane appears to be catalyst-free, which proves that the placement of the membranes with the back-sides facing beaker bottom indeed hinders the catalysts to be deposited on the back-side. If the filter-sides of the two AAO membranes with different treatment conditions are compared (See Figure 23-(A) and (C)), it is observed that the NaOH etching process enhances the distribution of the catalyst solution onto the filter-side of the membrane. Moreover, the comparison of the back-sides of both of the membranes reveals a difference in the pore diameters (see Figure 23-(B) and (D)). It is observed that the membrane which was subjected to NaOH etching step has bigger pores (see Figure 23-(D)).

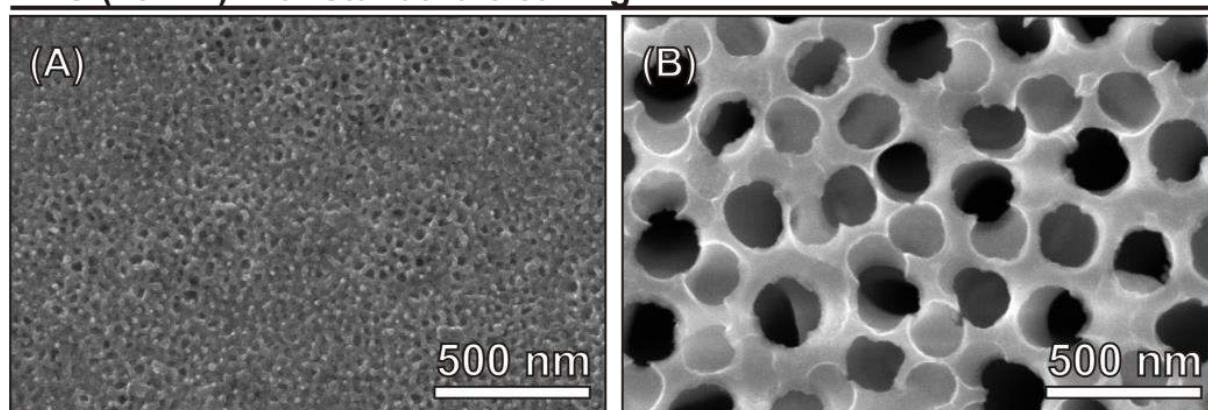
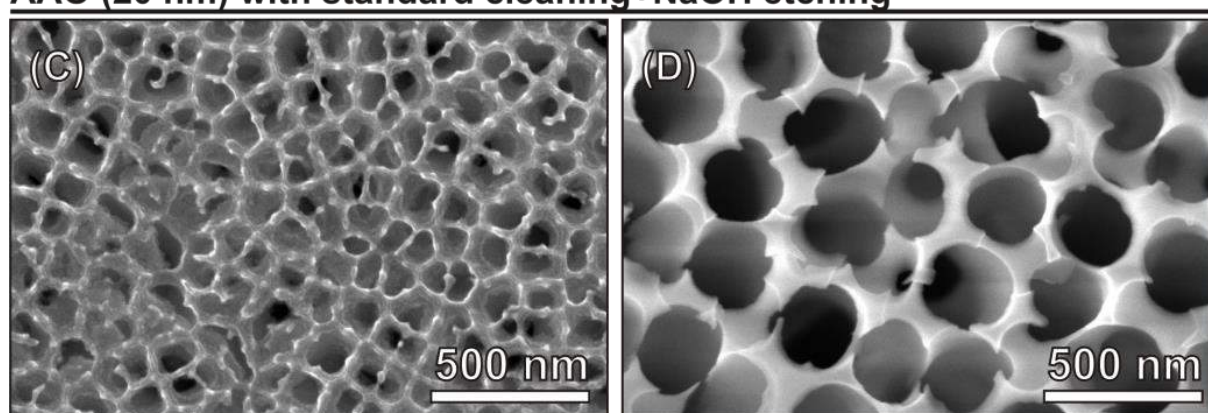
AAO (20 nm) with standard cleaning**AAO (20 nm) with standard cleaning+NaOH etching**

Figure 23 SEM images of AAO membranes: (A) Filter-side and (B) back-side of the AAO membrane (20 nm pore diameter) with standard cleaning subsequent to catalyst impregnation. (C) Filter-side and (D) back-side of the AAO membrane (20 nm pore diameter) with standard cleaning and NaOH etching subsequent to catalyst impregnation.

In order to understand the growth of the CNTs, it is important to determine the position, distribution as well as the composition of the catalyst particles. Therefore, a detailed characterization was carried out by TEM. A HAADF-STEM image acquired near the surface of the filter-side of the catalyst impregnated AAO membranes (20 nm pore diameter) with NaOH etching is presented at Figure 24-(A). From the image, it is observed that the catalyst particles are concentrated in the vicinity of the membrane surface on the filter-side. Moreover, the study revealed that the rest of the membrane is almost entirely catalyst-free. Both findings confirm the SEM findings suggesting that placing the membranes with their back-sides facing the beaker hinders the catalyst particles being deposited on the back-sides. Next, the chemical composition of the membranes was studied using EDX. From EDX map collected from the area indicated by the HAADF-STEM image in Figure 24-(A), it is clear that the catalyst particles consist of iron and nickel elements, as expected (see Figure 24-(B-F)).

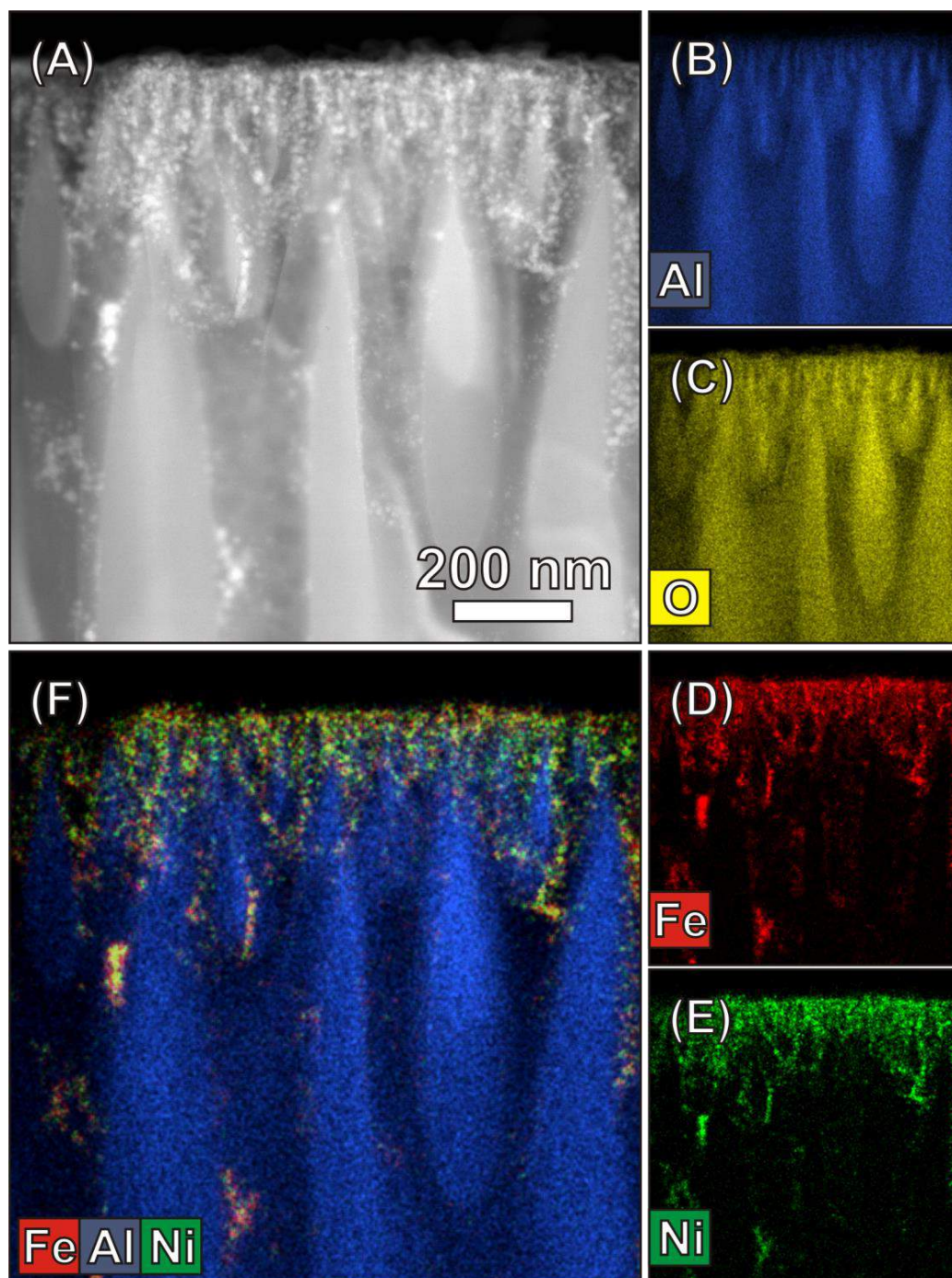


Figure 24 HAADF-STEM image (A) reveals the membrane morphology. (B) Aluminum, (C) oxygen, (D) iron and (E) nickel compositions of the material can be seen on (F) the EDX mixed color elemental map.

In order to image the interior of the AAO pores, also crushing TEM samples were prepared and characterized. A BFTEM image given in Figure 25-(A) exhibits the presence of catalyst particles attached to AAO membrane walls. Moreover, from the HRTEM image (see Figure 25-(B)), the lattice fringes are observed, which prove the crystallinity of the catalysts.

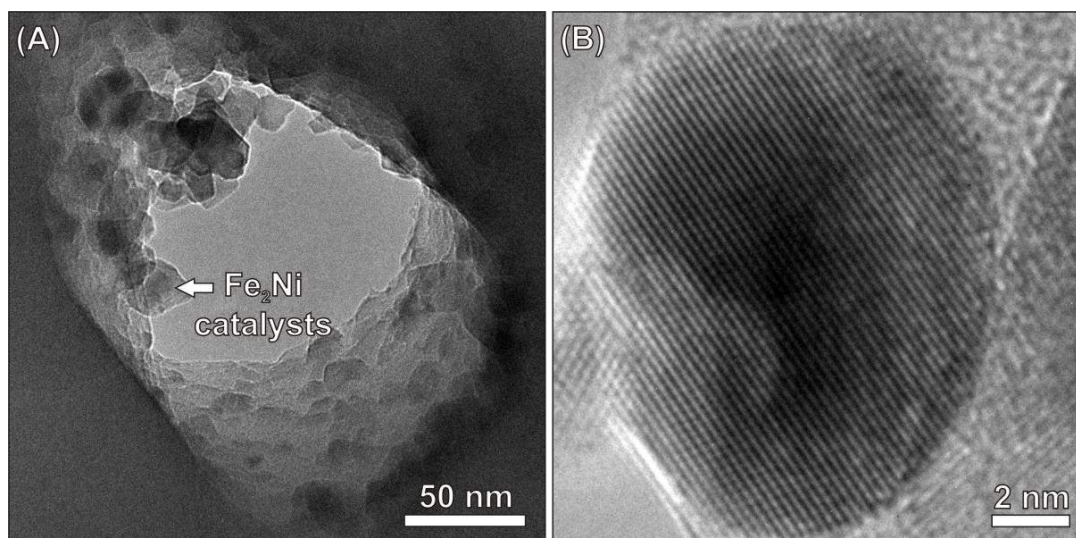


Figure 25 (A) BFTEM image reveals the presence of catalysts attached to AAO membrane pores. (B) HRTEM image proves the crystallinity of catalyst particles.

To investigate the 3-D structure of the material, HAADF-STEM electron tomography was performed. A visualization of the 3-D reconstructed volume of the catalyst deposited AAO membrane is presented in Figure 26. By inspecting orthoslices through the 3D reconstruction (see Figure 26-right), it is revealed that the catalyst particles attached to the walls of the AAO channels.

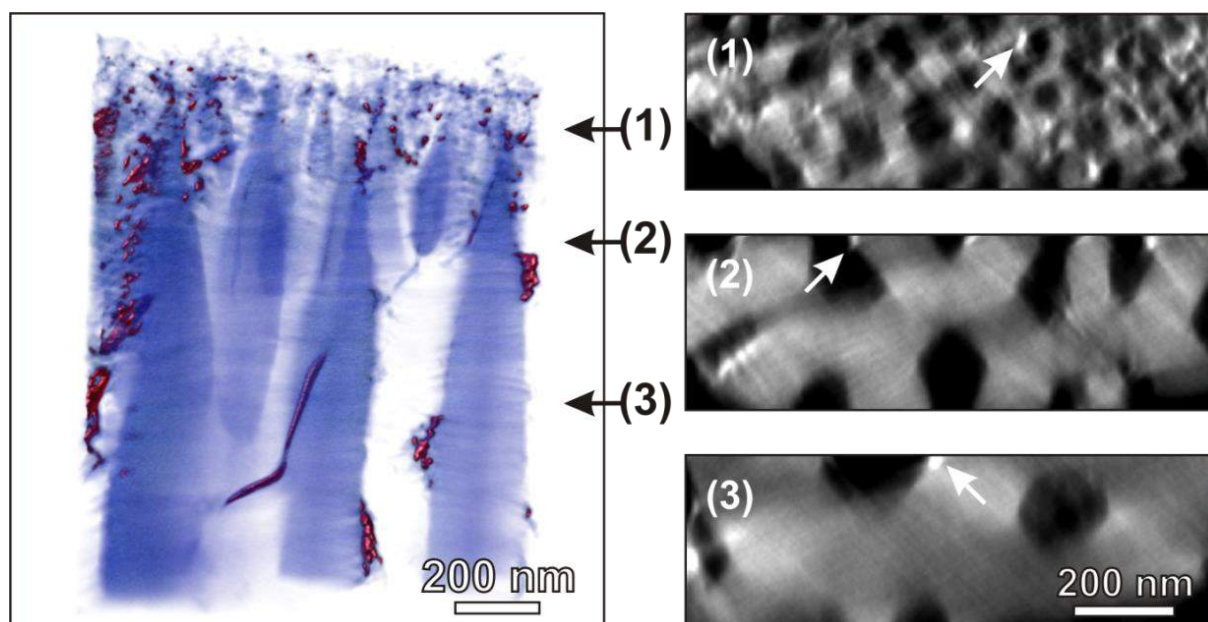


Figure 26 Visualization of the 3-D reconstruction of the catalyst deposited membrane is given on the left. The slices (orthoslice) through the 3-D reconstruction from positions specified on the left by arrows are given on the right. The attachment of the catalysts on the AAO membrane pores are indicated at the orthoslices.

Next, the catalyst deposited membrane was placed in CVD oven with AAO pores parallel to the gas flow direction and the back-side of the membrane facing the incoming acetylene gas. In this manner, CNTs were grown inside the AAO membrane pores. The detailed description of the experimental procedure is provided in Section 3.2. Figure 27 presents SEM images after the CNTs growth. Figure 27-(A) shows that the CNTs are mostly located at the filter-side of the membrane, and that the back-side is almost entirely CNT-free. In addition, SEM image given in Figure 27-(B) and (C) demonstrates that the CNTs emerging from the AAO membrane pores have formed bundles. These bundles are well-aligned, and their alignment follows same direction with the gas-flow. The latter is important because in this manner, these aCNTb's can be used to obtain CNT fibers if the experimental set-up is further optimized.

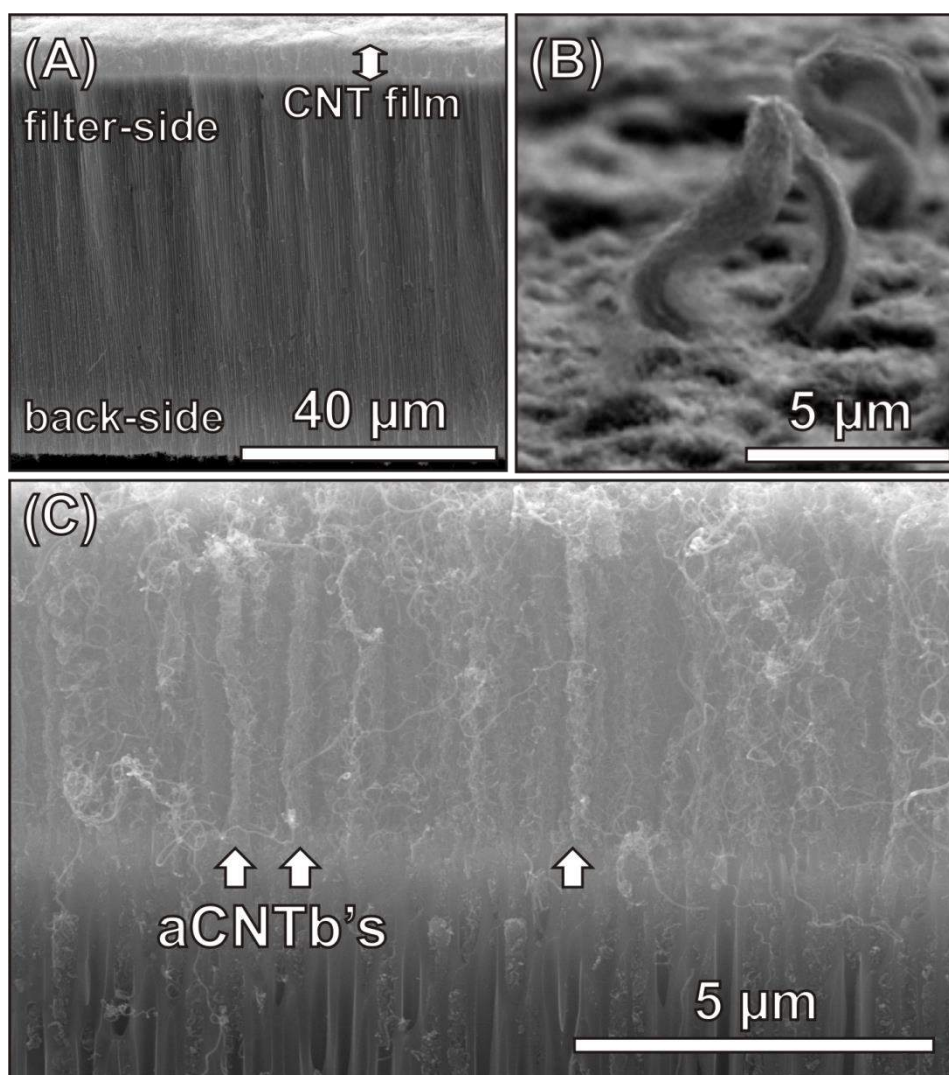


Figure 27 SEM images of CNTs grown through AAO membrane: (A) Cross-sectional view of AAO-CNTs, (B-C) aCNTb's grown through AAO pores in direction of the gas flow.

Cross-sectional HAADF-STEM image obtained from a FIB sample prepared from the AAO-CNTs after catalytic CVD is presented in Figure 28-(A). It can be observed that the aCNTb's are extruding from the AAO membrane pores in the direction of the gas flow. It is also clear that these aCNTb's have diameters comparable to the pore size of the AAO. In addition, the presence of Fe₂Ni catalyst particles at the starting points of the aCNTb's can be observed clearly. From the HRTEM image presented in Figure 28-(B), the graphitic layers of the individual CNTs of the aCNTb's can be seen, which points at their multiwalled nature.

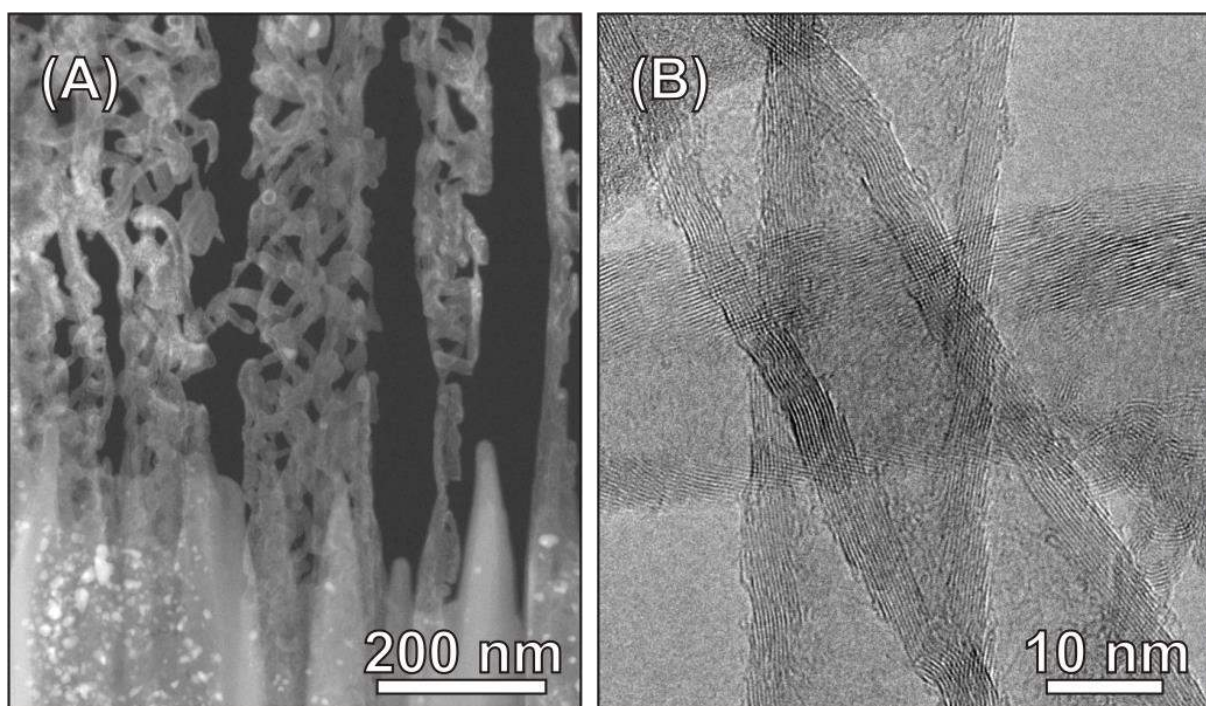


Figure 28 (A) HAADF-STEM image acquired from a FIB sample prepared from the AAO-CNTs. (B) HRTEM image reveals the graphitic layers of the MWCNTs.

EDX-STEM tomography was applied to investigate the composition of the AAO-CNTs. The results are presented in Figure 29. 3D reconstructions were generated by processing of Al, C and Fe elemental map tilt series of K α X-ray ionization edges. From the results, it is obvious that the catalyst particles are mostly located at the start of the aCNTb's, indicating that the root growth mechanism is dominant over the tip growth mechanism on the CNTs.

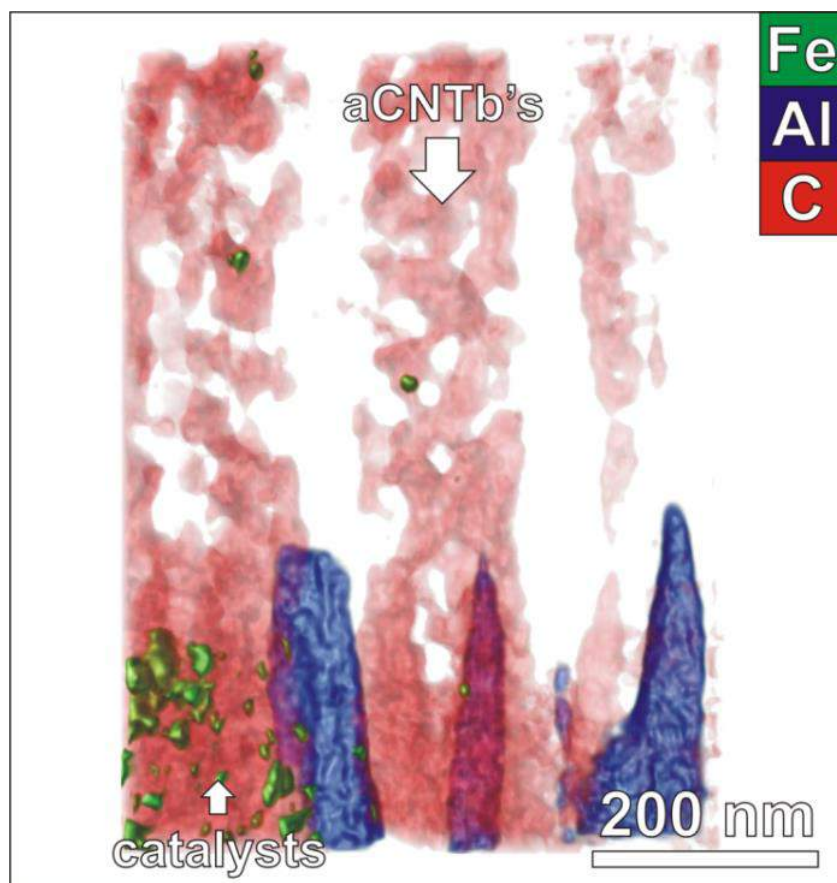


Figure 29 Volume rendered 3D visualization of EDX-STEM reconstruction: superimposition of 3D elemental distributions of Fe, Al and C.

3.4 Discussion

As stated previously, commercially available AAO membranes, which were used as the catalyst support, have highly-oriented porous structure with very uniform and nearly parallel pores normal to the surface of the AAO membrane (see Figure 22-(A) and (B)). These features are quite advantageous, since it is expected that the structure of these pores have an effect on the orientation and the arrangement of the aCNTb's.

Previous studies have shown that the support material plays an important role in yielding high-quality CNTs. Up till now, various support materials have been tested for the CVD of CNTs. In general, Al_2O_3 has been observed to be a superior support compared to SiO_2 , TiN or TiO_2 materials^{148,149}, which is appointed to the stronger chemical interaction between Al_2O_3 and the metal catalysts¹¹¹. Moreover, it was previously shown that the influence of the alumina support on the growth of CNTs can be tuned by controlling the acid-base character of

the support surface¹⁴⁰. In this respect, acid and base properties of the AAO membranes were modified by immersing them into the catalyst solution with a pH adjusted between 4 and 12 by the addition of HCl or NH₄OH and keeping them for 12 hours at 60°C. However, it was observed that this process would lead to the dissolution of the AAO membranes both in strong acid (pH=4) or base solutions (pH=12). This is attributed to the highly porous nature of the material, since these solutions enter the AAO channels and etch away material from the inside of the channels, which weakens the membrane. Therefore, such long exposures of these membranes to strong acid/base solutions eventually lead to their dissolution. A solution to this problem was proposed by the NaOH etching for a much shorter period of time (5-15 minutes). In this respect, the SEM images (see Figure 23-(C) and (D)) revealed that the NaOH etching process did not lead to the dissolution of the membrane. Moreover, the comparison of the both filter- and back-sides of the membrane reveals a difference in the pore diameters (see Figure 23-(A-D)). This is attributed to the fact that the additional NaOH etching process would yield a greater pore/surface ratio on the membranes, since this process would lead to the removal of the material from the membrane walls, which could also help the catalyst solution penetrate into the narrow AAO channels (20 nm).

SEM characterization of AAO after the CNTs growth (see Figure 27-(A)) has revealed that the CNTs are mostly located at the filter-side of the membrane, and that the back-side is almost entirely CNT-free. This is attributed to the distribution of catalyst particles, being located mostly at the filter-side. Once the acetylene precursor enters the membrane pores from AAO back-side, it would lead to the CNT growth presumably when it encounters a catalyst particle on its path. This is more likely to occur at the filter-side as a result of the high concentration of the catalysts in this region. In this manner, the obstruction of the precursor gas due to the possibility of obtaining as-grown CNTs at the back side is also hindered, and aCNTb's were mostly grown on the filter side of the membranes.

For CNTs, two different growth mechanisms can occur depending on the catalyst-support interaction (see Figure 4-(B) and (C)). The tip-growth, where the catalyst is lifted off the support while CNT grows, takes place when the metal-support interaction is weak. In contrast, the root growth process occurs, when the metal-support contact is preserved and the catalyst particles remain on the support during the CNT growth¹¹¹. In our case, tip growth is not

desirable, since one wants to avoid that the catalyst particles would be present inside the aCNTb's. These would represent weak structural points, finally leading to a reduced strength. Therefore, it is of crucial importance to understand which growth mechanism was more dominant during the growth of the aCNTb's. In this respect, the results from EDX-STEM tomography experiments (see Figure 29) revealed that the catalyst particles are mostly located at the start of the aCNTb's, indicating that the root growth mechanism is dominant over the tip growth mechanism on the CNTs.

Previously, several groups have attempted to produce aligned fibers consisting of long CNTs with various approaches. For instance, fibers were produced in a continuous manner by mechanically drawing CNTs directly from the gaseous reaction zone of a CVD oven using a liquid source of carbon and an iron nanocatalyst⁶⁴. Preliminary mechanical measurements of these materials indicated that the fibers have a range of strengths, dependent on process conditions, between 0.10 and 1.0 GPa. In another study, multi-ply and torque-stabilized yarns were obtained by introducing twist during spinning of multiwalled CNTs from as-grown nanotube forests⁶⁵. Here, the achieved yarns had strengths at around 0.46 GPa. When compared to the strength of individual MWCNTs (11 to 63 GPa¹⁴¹), these strength values are quite low. One of the main reasons for such lower strength is that the fibers formed through both approaches consist of individual CNTs, which are very short when compared to the final length of the formed fiber. Since the toughness of the fibers is mainly determined by the length of the individual CNTs composing them, the strength of the fibers diminishes drastically with the reduced length of CNTs. In addition, in the former approach 5-10% metal catalyst particles are present in between the individual CNTs. These metal catalyst particles embedded in CNT bundles also represent weak structural points leading to a reduced strength, as mentioned previously. The approach described here can be considered as an alternative way to produce highly aligned CNT fibers without the major drawbacks of the currently existing technologies, such as the presence of catalyst particles and limited length of CNTs. For instance, a possible approach would be that these aCNTb's can be mechanically drawn during their synthesis at the filter-side by a spindle from the reaction zone continuously while the precursor gas is introduced into the system. In this manner, aligned CNT fibers can be formed.

3.5 Conclusions

In conclusion, TEM characterizations showed that a large-scale synthesis of aCNTb's standing perpendicularly to the AAO substrate aligned with respect to the precursor flow direction was achieved. The CNTs were grown by catalytic CVD of acetylene from Fe₂Ni particles deposited onto the walls of AAO membrane pores via impregnation. Prior to catalyst deposition, NaOH etching was used to enhance the adhesion of the catalyst particles. TEM revealed that a preferential deposition of the catalysts was present at the filter-side of the membrane obtained by placing the membrane into catalyst solution with the back-side facing the beaker bottom before adding the catalyst solution. The position, distribution and chemical analysis of the catalyst particles was furthermore investigated by advanced TEM techniques, such as electron tomography and EDX analysis. The results showed that the Fe₂Ni nanoparticles are randomly dispersed inside the pores of AAO attached to the membrane walls, mostly concentrated at the filter-side. Moreover, EDX-STEM tomography results were used to confirm that the growth mechanism of the CNTs corresponds to the root growth. This newly developed CNT growth method has a high potential as it may produce CNT bundles in a one-step process, which can be scaled up in a straightforward manner for industrial applications.

Chapter 4 CHARACTERIZATION OF HIERARCHICAL

MESOPOROUS SILICA SYNTHESIZED THROUGH ANODIZED ALUMINA MEMBRANES

CONTENTS

CHAPTER 4 CHARACTERIZATION OF HIERARCHICAL MESOPOROUS SILICA SYNTHESIZED THROUGH ANODIZED ALUMINA MEMBRANES	63
4.1 INTRODUCTION	63
4.2 EXPERIMENTAL PROCEDURES.....	65
<i>Evaporation induced self-assembly (EISA)</i>	65
<i>Sample preparation for transmission electron microscopy</i>	66
<i>Transmission electron microscopy</i>	66
4.3 RESULTS.....	67
4.4 DISCUSSIONS.....	71
4.5 CONCLUSIONS	72

This chapter will be submitted for a publication as:

Mert Kurttepli, Roel Locus, Sara Bals, Bert Sels, “Tailored Synthesis of Hierarchical Mesoporous Membranes by Evaporation Induced Self-Assembly”.

Chapter 4 Characterization of hierarchical mesoporous silica synthesized through anodized alumina membranes

The incorporation of aluminum into hierarchical mesoporous membranes (HMMs) was studied by TEM. The HMMs were synthesized by a combination of hard and soft templating methods, forming mesoporous silica columns inside the pores of AAO membranes via EISA. TEM analysis showed that the incorporation of aluminum into the HMMs led to a change in the mesopore ordering of silica from circular hexagonal (donut-like) to columnar hexagonal. The columnar mesopore ordering of silica is advantageous towards the pore accessibility and is therefore preferential for many possible applications, including their use as templates for aCNTb's growth.

4.1 Introduction

Due to their thermal, chemical and mechanical stability, as well as high specific surface area, ordered mesoporous silica systems (OMSs) synthesized within the channels of AAO membranes are widely used in many applications, such as drug adsorption and release¹¹⁴, controlled separation and release of molecules¹⁴², or fabrication of highly ordered mesostructured nanowires and nanowire arrays¹¹⁵. During the past decades, different synthesis methods of OMSs confined in AAO pores have been proposed. One of the main demands in this field is to obtain OMSs with preferentially oriented channel structures at the nanoscale¹¹⁷. An interesting pore ordering in view of materials applications is the hexagonal columnar ordering (P6m symmetry), as observed in MCM-41 and SBA-15, in which the mesopores of silica are accessible from the surface of the materials¹¹⁷⁻¹¹⁹. Such pore architecture is also advantageous towards their use as templates for aCNTb's growth, provided that they are in parallel with the pores of AAO membranes.

So far, great progress has been made during the preparation of silica columns inside AAO membrane pores¹⁴³⁻¹⁴⁵. An alternative manner to produce hexagonally ordered mesoporous silica systems is the combination of soft and hard template methods¹¹⁷: OMSs are formed inside the macropores of AAO membranes via the soft templated synthesis of silica through the EISA method, in which micelles of surface active agents (surfactants) act as a structure directing agent. It was already shown that in such synthesis route the size of the AAO pores

has a major influence in the mesopore ordering¹⁴⁶. On the other hand, studies on the soft template part are fundamentally focused on the parameters of the EISA process^{117,121,124-129}, where different surfactants such as ionic hexadecyl-trimethyl-ammonium bromide (CTAB), nonionic block copolymers Pluronic P-123 or Brij 56 were tested. Earlier reports indicated that the use of CTAB as surfactant promotes mainly the columnar hexagonal mesophase formation^{124,125}, whereas the use of nonionic block copolymers Pluronic P-123 or Brij 56 favour more the mixed phases^{121,126}. For the latter, the *in-situ* grazing-incidence small-angle X-ray scattering (SAXS) and TEM studies suggested that at the initial steps of the synthesis, the circular hexagonal phases are favoured. The circular hexagonal phases are then transformed into more thermodynamically stable phases, such as the columnar hexagonal and lamellar mesophases either during solvent evaporation or during the period of constant sample weight (until about 45 and 60 min after immersing the membranes in synthesis solution for the samples at 20 and 60% relative humidity, respectively). Therefore, these phase transitions are strongly dependent on the relative humidity and on the amount of water present during the aging process¹²¹. In general, the EISA technique has proven itself to be useful for the synthesis of OMSs inside the AAO membranes. The materials systems produced in this manner also offer the possibility of functionalization through the incorporation of different heteroatoms, such as aluminum¹⁴⁷, or organic groups in the silica¹⁴⁸. In case of aluminium, it is additionally possible to obtain the desired columnar hexagonal mesophase without the control over the relative humidity, as will be discussed here.

To optimize the synthesis of OMSs in an efficient manner, it is of crucial importance to carefully characterize the HMMs and to study the connection between different synthesis parameters and the resulting structure. One of the main challenges here is that HMMs contain only a very small fraction of silica material yielding mesopores with diameters of only a few nanometres. TEM is therefore a valuable technique to investigate the structure of these materials at nano-scale^{120,123,149}. Here we used different TEM techniques to investigate the tailored synthesis of hierarchical mesoporous membranes by the EISA process, which enables the production of silica columns inside the vertical channels of AAO membranes. We demonstrate that the incorporation of aluminium in the mesoporous silica phase results in a structure with a preferential orientation of the silica columns shifting from circular hexagonal towards columnar hexagonal without controlling of the relative humidity.

4.2 Experimental Procedures

Evaporation induced self-assembly (EISA)

The EISA-solutions were prepared (KU Leuven), as reported by Bein et al¹²², from 3.0 g of 0.2 M HCl solution that was mixed with 1.8 g (0.1 mol) of distilled water in a glass bottle. Next, 2.08 g (0.01 mol) of tetraethoxysilane (TEOS) and 3.95 g (0.086 mol) of ethanol were added to this solution. This mixture was prehydrolyzed at 60 °C for 1 h and then cooled to room temperature. In an additional glass bottle, 0.750 g of pluronic P123 (0.13 mmol) was mixed with 11.85 g of ethanol. These two solutions were then mixed with the addition of 42.5 mg LiCl (1 mmol). For Al-incorporation into the solutions, the 0.01 mol of TEOS (above mentioned) was replaced by mixtures of TEOS and Al-isopropoxide (AliPO) with Si/Al molar ratios of 50/1 and 100/1. To ensure a full dissolution the AliPO was added to the HCl-H₂O mixture first and heated overnight at 80 °C. The mixture was cooled to room temperature before TEOS and ethanol are added.

AAO membranes were obtained from Whatman® anodisc membrane discs with a diameter of 13 mm and a thickness of 60 µm. The minimum pore size of the AAO membranes was 200 nm at the filter-side (a top layer of few microns) and the back-side of the membranes contained pore diameters of about 300 nm. The AAO membranes were placed on Teflon Swagelok® ferrules (¼ in) for easy recuperation after the synthesis with the back-side (with ~300 nm pore size) facing upwards. 1 mL and 0.1 mL of the EISA solutions were dropped onto the back-side, respectively. In the remainder of this chapter, the back- and the filter-side of the membrane are referred as the casting and the non-casting side. The membranes were aged overnight in an oven at 30 °C without controlled relative humidity in contrast to earlier reports¹²². After carefully removing the HMMs from the ferrules, the samples were calcined in two steps: 1 °/min to 80 °C (stay 12 h) and then 1 °/min to 550 °C (stay 8 h). For simplification, 100 % Si HMMs is denoted as HMM-Si. HMMs with a Si/Al ratio of 50/1 and 100/1 are denoted as HMM-50/1 and HMM-100/1, respectively.

Sample preparation for transmission electron microscopy

For TEM investigation, dedicated sample preparation was applied to obtain electron transparent TEM samples. Plan-view TEM samples (electron beam parallel with the AAO-pores) were prepared by gluing the AAO-silica material onto a TEM sample preparation holder with the pores of the membrane facing upwards (see Figure 30-(A)). Similarly, cross-section TEM samples were prepared in which the pores of the AAO membrane were perpendicular to the electron beam (see Figure 30-(B)). The details of both cross-section and plan-view TEM sample preparation techniques can be found in Section 2.2.1.

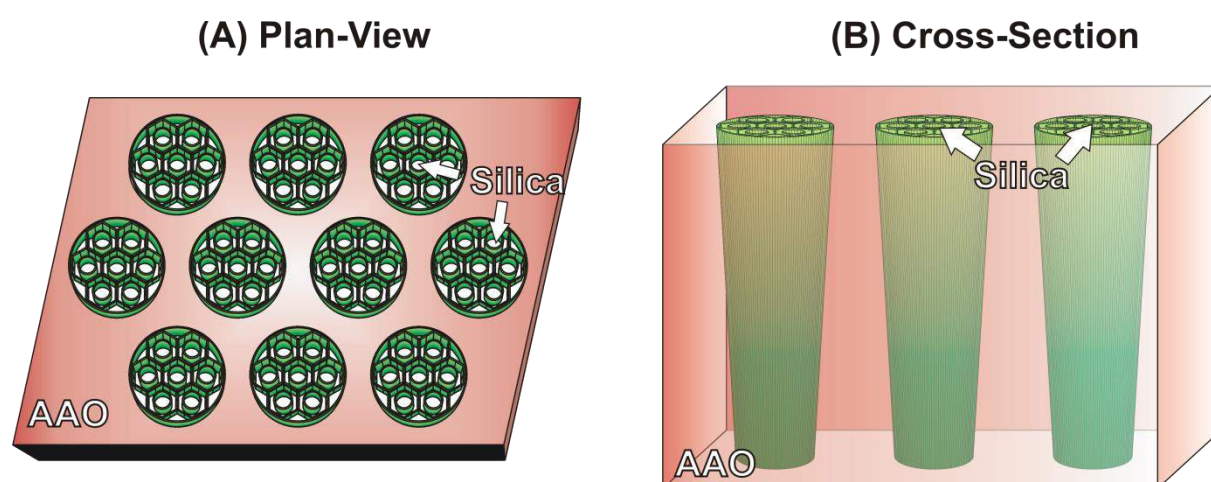


Figure 30 The schematics represent the orientations of the (A) plan-view and (B) cross-section TEM samples according to the electron beam.

Transmission electron microscopy

BFTEM, HAADF-STEM, electron tomography and EDX elemental mapping were performed using a FEI Tecnai Osiris operated at 200 kV. HAADF-STEM images were recorded using convergence semi-angles in the range of 21–25 mrad with a probe size of approximately 1 Å. Tilt series for electron tomography was acquired by collecting HAADF-STEM images with tilt increments of 2° over a range of $\pm 74^\circ$ on cross-section TEM samples using an advanced tomography holder from Fischione Instruments. Automated acquisition, alignment and reconstruction of the data using the SIRT were carried out using the FEI Inspect3D software package. Amira (Visage Imaging GmbH) was used for the visualization of the reconstructed volume.

4.3 Results

The casting and non-casting side of the membranes were characterized using SEM (FEI Quanta) in order to resolve their resulting morphology and pore fillings. A thin layer of carbon (~8-10 nm) was deposited on the samples in order to reduce the charging of the samples during electron beam irradiation. It was discovered that the casting side of the HMMs is often covered by a thin layer of silica, which is in contrast to the non-casting side. Furthermore, SEM analysis showed that the casting side of the membranes (see Figure 31-(A)) is less frequently filled with silica in comparison to the non-casting side (see Figure 31-(B)). On the non-casting side of the membrane (see Figure 31-(B)) a relatively complete pore filling (90-95 %) is present over large areas. High-resolution SEM (Nova NanoSEM 450 (FEI)) of HMM-50/1 samples additionally indicates the presence of the columnar hexagonal pore ordering inside the pores of AAO membranes (see Figure 31-(C) and (D)).

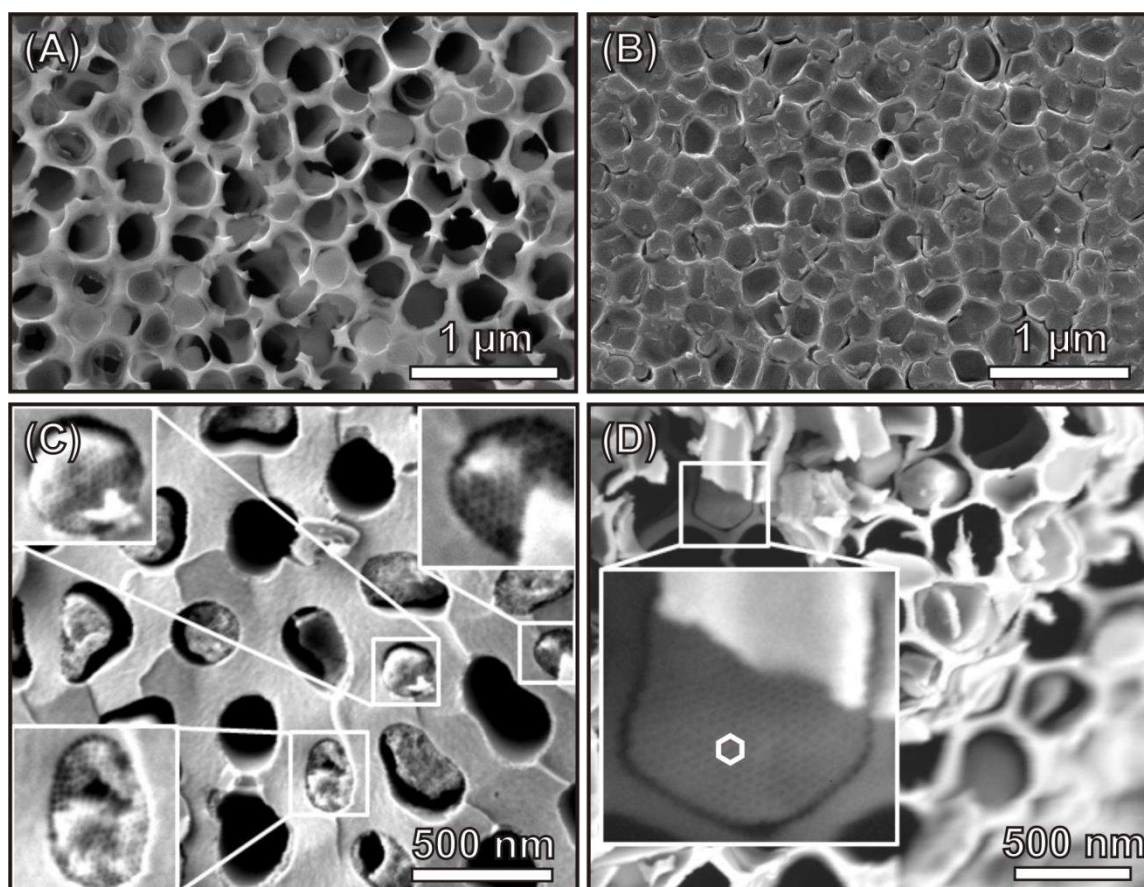


Figure 31 SEM images of the casting side (A) and the non-casting side (B) of HMM-50/1. High-resolution SEM images at (C) and (D) clearly indicate the columnar hexagonal pore ordering of the mesoporous silica.

A more detailed investigation of the HMMs was performed using TEM. In order to image the interior of AAO-pores, plan-view TEM samples were prepared from the HMM-50/1, HMM-100/1 and HMM-Si samples. Figure 32-(A) shows that not all the pores of AAO are filled entirely with the silica columns. In addition, gaps between the silica columns and the walls of AAO membrane with various sizes are observed independent of the phase of the silica column. The study revealed that different types of mesopore orderings are observed for the silica columns including the columnar hexagonal (see Figure 32-(C)) and circular hexagonal (see Figure 32-(B)) phases. It is important to note that the desired columnar hexagonal pore ordering was dominant for HMM-50/1 and HMM-100/1 samples, whereas the circular hexagonal pore ordering was dominant for HMM-Si sample.

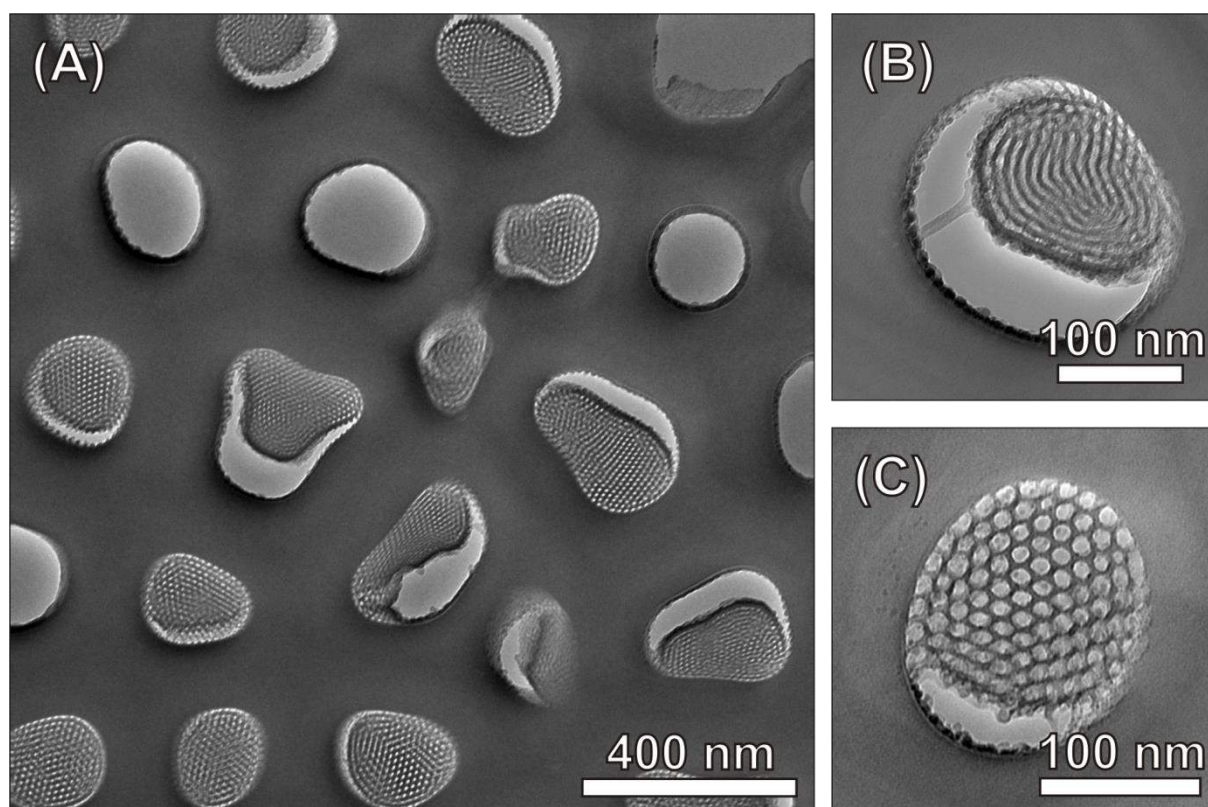


Figure 32 Plan-view TEM-images (A-C) of the membrane prepared by EISA-mixture with Si/Al ratio of 50/1 are given above.

To obtain a complete understanding of the pore alignment, also cross-section TEM samples were investigated. HAADF-STEM reveals that both circular and columnar hexagonal pore orderings occur inside the AAO membranes, but yet the parallel arrangement is more prominent for HMM-50/1 sample (see Figure 33-(A) and (B)). A composition analysis

performed by EDX confirms that the silicon containing interior (silica) is surrounded by the aluminum containing support material (AAO membrane) (See the insets at Figure 33-(A) and (B)). It is also observed that a small amount of aluminum is present within the silica columns (see Figure 33-(B)). Such presence of aluminum is attributed to the 2% of incorporated aluminum (50/1) in the silica material.

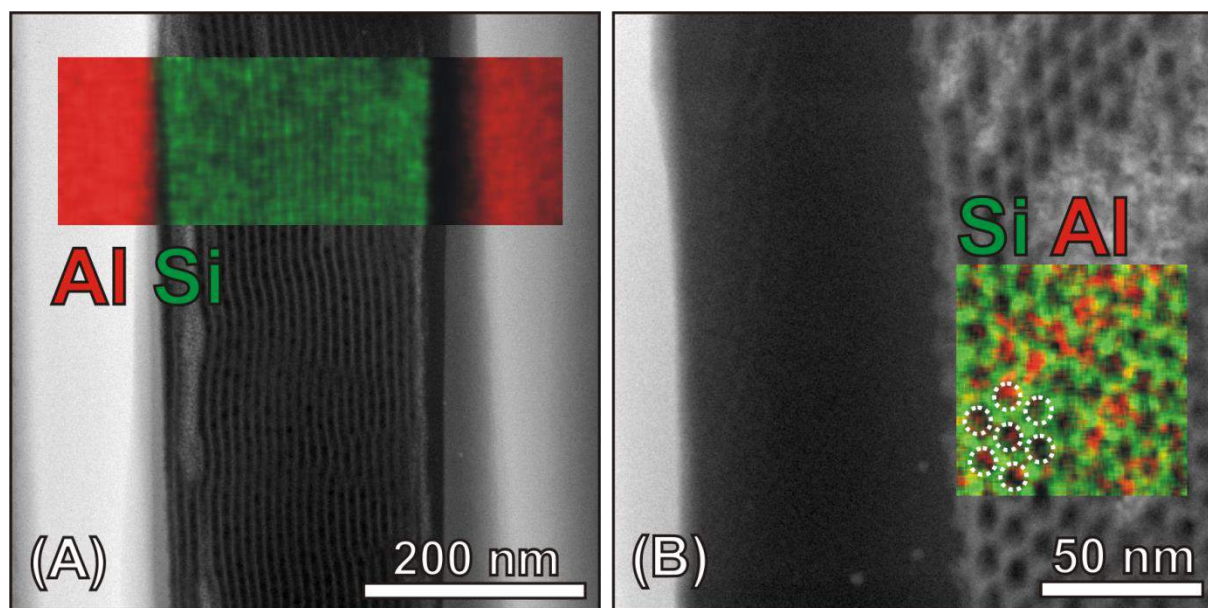


Figure 33 Cross-sectional HAADF-STEM images given at (A) and (B) reveal the morphology of the HMM-50/1 sample. (A) shows the columnar pore ordering and (B) shows the circular hexagonal pore ordering. The aluminum and the silicon compositions of the sample can be seen on the EDX mixed color elemental maps.

As shown previously, HAADF-STEM suggests the presence of columnar hexagonal mesopore ordering inside the pores of AAO membranes for HMM-50/1 and HMM-100/1 samples. However, in order to attribute such parallel ordering of the silica columns to the columnar hexagonal form (see Figure 34-(A)), electron tomography is required. Therefore, 3D reconstructions were obtained for HMM-50/1 sample by electron tomography from the same location where the EDX analysis was performed (see Figure 34-(A)). 3D visualizations of the tomogram indicate that the hexagonal pore ordering is present (see Figure 34-(A)) along the entire silica material. A slice through the reconstruction is given in Figure 34-(B), which clearly confirms such hexagonal pore ordering parallel to the AAO pores.

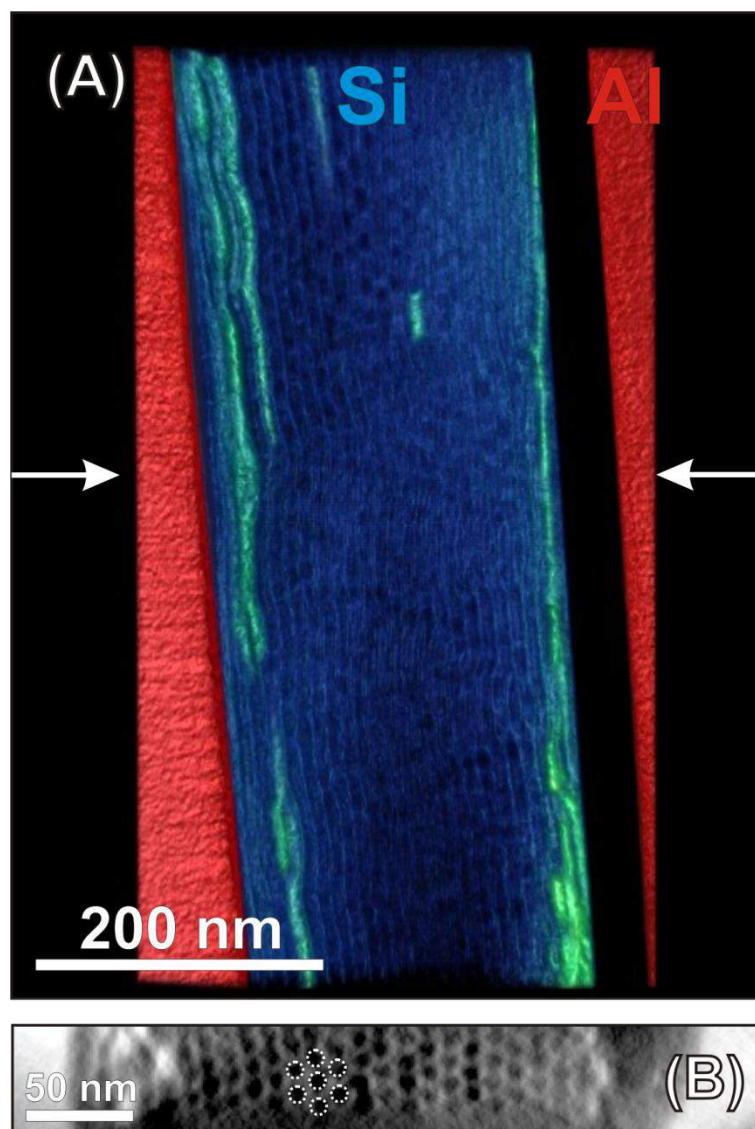


Figure 34 (A) Volume rendered 3D visualization of HAADF-STEM reconstructions from for HMM-50/1 sample. (B) A slice through the 3D reconstruction collected from the position indicated by the arrows given at (A). The hexagonal silica pore orderings is indicated.

To understand the effect of Al-incorporation at the growth of mesoporous silica inside the AAO membrane pores, several plan-view TEM samples from the HMM-Si, HMM-50/1 and HMM-100/1 samples with different Al-concentrations were prepared. These samples were then characterized in a quantitative manner as a function of increasing Al content. These results are summarized in Table 2. Here, it should be kept in mind that not all the AAO-pores were filled by silica columns, as mentioned previously. Therefore, such quantification was obtained solely through the characterization of the AAO-pores that are filled by the silica columns. From the results, it is clear that the filled pores of the HMM-Si sample showed a

complete circular hexagonal pore ordering. On the other hand, the ratio of circular hexagonal phases decreased to 0.12 in HMM-100/1 and to 0.02 in HMM-50/1 samples. Moreover, the ratio of filled AAO pores with a complete columnar hexagonal pore ordering increased to 0.46 and to 0.63, respectively. Furthermore, it needs to be noted that the total ratio of filled AAO pores where columnar hexagonal pore ordering is present either partially or completely does not change substantially for HMM-100/1 and HMM-50/1 (varies between 0.61 and 0.69). However, the total ratio of circular hexagonal pore ordering (complete or partial) drops significantly from 0.34 in HMM-100/1 to 0.08 in HMM-50/1.

	HMM-50/1	HMM- 100/1	HMM-Si
columnar	0.63	0.46	0
circular	0.02	0.12	1
Undefined *	0.15	0.05	0
Mixed columnar/circular	0.07	0.35	0
Mixed columnar/undefined	0.12	0.02	0
Mixed circular/undefined	0.01	0.00	0
Total columnar	0.69	0.61	0
Total circular	0.08	0.34	1
Total undefined	0.23	0.05	0

(*) silica phases were denoted undefined when no pores were present/visible

(**) not all the AAO-pores were filled by silica columns. Therefore, results here are obtained solely through the characterization of the AAO-pores that are filled by the silica columns.

Table 2 The ratios of the different types of mesopore orderings present in the AAOs.

4.4 Discussions

SEM analysis of the morphology of the HMMs hereby revealed that the non-casting sides of the AAO membranes were filled more frequently (90-95 %) with silica than the casting sides (see Figure 31-(A) and (B)), which were occasionally covered with a thin silica layer. This difference in filling might be attributed to the movement of the EISA mixture through the pores of the AAO which is governed by gravitational and capillary forces. From high resolution SEM analysis (see Figure 31-(C) and (D)), it was discovered that the silica material fills the pores of the support with hexagonal columnar ordering in HMM-50/1. SEM and TEM

confirmed the earlier results by Meoto et al.¹⁵⁰ that the challenge remains to synthesize HMMs with all AAO-pores filled and without the shrinking of the silica columns, causing gaps between the AAO-walls and the silica columns.

In order to investigate the mesopore ordering in the HMMs more thoroughly, the HMMs were examined by TEM from both plan-view and cross-section samples, as shown in Figure 32, Figure 33 and Table 2. It was concluded that the incorporation of Al in the silica columns of HMMs caused a shift from pure circular hexagonal pore orderings in HMM-Si to mixed phases with predominantly a columnar hexagonal pore ordering in HMM-50/1 (63 % of the filled AAO-pores contained pure columnar hexagonal phases and 69 % contained partially columnar phases). After Al-incorporation especially the drop in the amount of circular phases was substantial and thus it is suspected that Al inhibits the formation circular phases and by those means promotes the formation of columnar phases without controlling the relative humidity as was the case in earlier studies¹²⁷.

To observe the accessibility and continuity of the mesopores and to image the columnar hexagonal ordered mesopores at the micrometer scale a combination of cross-section TEM samples and electron tomography experiments was executed. These experiments proved long and continuous columnar mesopores at a micrometer range (see Figure 34). The hexagonal columnar mesopore ordering of silica over such large scale is advantageous towards the pore accessibility and therefore preferential for many possible applications.

4.5 Conclusions

In conclusion, TEM analysis showed that the incorporation of aluminum into HMMs led to a change in the mesopore ordering of silica material from circular hexagonal (donut-like) to columnar hexagonal. From these results (both in 2D and in 3D), it can be concluded that without changing the relative humidity and the amount of water present during the aging process, such columnar hexagonal pore ordering of silica can be obtained.

PART II CHARACTERIZATION OF CARBON
NANOSHEETS/NANOTUBES TEMPLATE
ASSISTED AND ATOMIC LAYER
DEPOSITION BASED SYNTHESIS OF
POROUS MATERIALS

Part II: Introduction

Atomic layer deposition (ALD) is a method based on successive, surface-controlled reactions from the gas phase to produce thin films and over-layers in the nanometer range with perfect conformality and process controllability¹⁵¹. The main steps of ALD are schematically presented in Figure 35 for the thin film growth cycle of a binary compound (Al_2O_3) using trimethylaluminum (TMA) and water¹⁵². The first step of ALD involves the substrate surface with OH groups to be exposed to precursor molecules (TMA) which are adsorbed as a monolayer on the surface by forming $\text{Al}(\text{CH}_3)_2$ molecules and releasing CH_4 as reaction products. Appropriate substrate heating supplies adequate energy for enabling this reaction (1\AA per ALD cycles at 300°C for Al_2O_3). Next, residual TMA and CH_4 are pumped or purged away before the incoming water pulse. The subsequent water pulse replaces the CH_3 ligands attached to the Al with OH groups and therefore prepares the surface for the next TMA pulse. These steps are repeated until the desired thickness of the layer is reached.

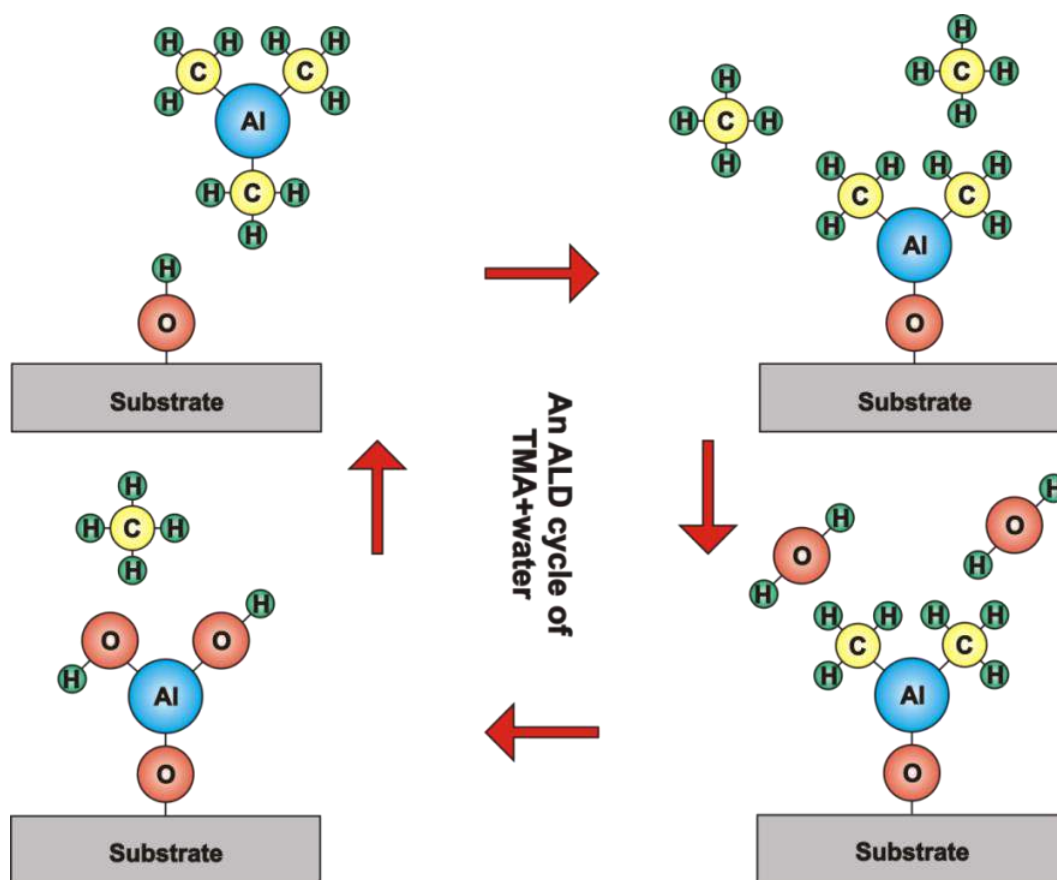


Figure 35 Schematic illustration of the ALD process of Al_2O_3 using TMA and water¹⁵².

In recent years, ALD attracted great attention due to its excellent capability of conformal coating of very complex porous materials. So far, different types of templates have been tested and applied. Some of these examples are summarized in Table 3. For instance, AAO is a widely used template for ALD of various metals and metal oxides, such as TiO_2 , Al_2O_3 , V_2O_5 , ZnO , Pd, etc. The main advantages of using AAO as a template are their highly ordered porous features and the simplicity of their synthesis. However, their surface areas are not comparable to e.g. CNTs or silica aerogels. On the other hand, a silica aerogel is another type of template that usually contains pores of all three sizes¹⁵³ (according to IUPAC classification for porous materials, the pores less than 2 nm in diameter are termed “micropores”; those with diameters between 2 and 50 nm are termed “mesopores”, and those greater than 50 nm in diameter are termed “macropores”¹⁵³). Attempts to use silica aerogel for ALD have been demonstrated by several groups (See Table 3). Although these materials can offer pore sizes of ~20 nm, which is much lower than the ones observed in AAOs, a disadvantage of using silica aerogel templates is that their pores are disordered. Furthermore, other inorganic templates, such as Ni nanowires or colloidal crystal templates, such as polystyrene, were used as templates for ALD coating, as indicated in Table 3.

CNSs flakes and CNTs forests can also be used as a template for ALD. Previous studies showed that it is not very straightforward to perform ALD on CNTs and CNSs due to their inert nature. For instance, ALD of CNTs was usually found to yield nanoparticle morphologies grafted on the CNTs⁹⁷. It was similarly shown for CNSs that the growth of oxide coatings initiates only at the defect sites at the graphene surface, which results in a distribution of nanoparticles instead of a conformal layer⁹⁹. In order to overcome these limitations, CNTs and CNSs can be synthesized by PECVD at relatively low temperatures and thus offer a higher amount of defect sites for ALD growth^{8,16}. These defect sites can enable the nucleation of ALD of metal oxides during the first few cycles of ALD. Earlier studies which reported the use of CNTs and CNSs as templates for ALD are listed in Table 3.

ALD of porous nanomaterials			
Templates	Coatings	Applications	References
	TiO ₂	Photocatalytic activity	154
	Al ₂ O ₃ , TiO ₂ , V ₂ O ₅ , ZnO, Pd	Catalytics	155
AAO	TiO ₂	electrostatic capacitance (nano-scale electrostatic capacitors, electro-chemical dye-sensitized photovoltaics and biosensors)	156
	TiO ₂	N.A.	157
	TiO ₂	N.A.	5
CNSs	ZrO ₂	electrochemical capacitance (supercapacitors, fuel cells, batteries and electronics)	21
	TiO ₂	Supercapacitors	99
	TiO ₂	lithium-ion batteries	20
	V ₂ O ₅	high-power supercapacitor electrodes	158
CNTs	Pt	Proton-Exchange Membrane Fuel Cells	159
	Al ₂ O ₃ , Al ₂ O ₃ -W	N.A.	97
	TiO ₂	Photocatalytic activity	160
Ni nanowires	TiO ₂	Photocatalytic activity	154
Polystyrene	TiO ₂	N.A.	161
	TiO ₂	Photoanodes for Dye-Sensitized Solar Cells	162
SiO ₂ Aerogels	TiO ₂ -ZnO	Photoanodes for Dye-Sensitized Solar Cells	163

Table 3 Examples of templated ALD for porous nanostructures.

CNSs samples used in this thesis were synthesized at IMEC by Dr. D. Cott by using PECVD. The substrate consisted of 200 mm p-type silicon wafers. CNSs were grown at low pressure (0.45 Torr) in a capacitive coupled (CC) PECVD reactor with a 13.56 MHz RF generator (Oxford Instruments plasma technology UK, NANOCVD). In a typical CNS growth experiment, a wafer was allowed to reach a heater temperature of 750 °C under vacuum (1.10^{-5} Torr) for 1 minute. To prepare the wafer surface, a H₂ plasma pretreatment (300 W) was carried out for 15 min at 0.45 Torr. Then C₂H₂/H₂ (1:10) was introduced into the chamber and a 300 W plasma at a total pressure of 0.45 Torr is maintained. As mentioned previously, plasma is preferred to enhance chemical reaction rates of the precursors. After CNSs growth, the substrate was removed from the chamber and allowed to cool under vacuum (1.10^{-4} Torr) for 5 minutes⁸.

Similarly, MWCNTs were grown at IMEC by Dr. D. Cott through catalyst-enhanced PECVD. The main difference between the growth of CNSs and MWCNTs is that the starting Si substrate (200mm diameter) was initially covered by a 1 nm thick (nominal) Co layer for the catalyst enhancement of the process. To avoid diffusion of Co catalyst layer into the Si substrate, a 70 nm TiN was first sputtered onto the Si surface (Endura PVD tool, Applied Materials, USA). MWCNTs were grown in a microwave (2.45 GHz) plasma enhanced chemical vapor deposition chamber (PECVD, TEL, Japan). In a typical experiment, the Co catalyst layer was exposed to NH₃ plasma for 5 minutes to transform the film into active metal nanoparticles for CNT growth. Then a C₂H₄+H₂ mixture was introduced into the chamber at a temperature 550 °C for 30 minutes. Upon MWCNTs growth, the substrate was removed from the chamber and allowed to cool. As pointed out earlier, such low temperature synthesis of CNTs enables the production of MWCNTs forests with the individual nanotubes having a large amount of defect sites, which is preferential for the ALD process, since these defects give rise to nucleation sites for ALD, allowing conformal deposition^{20,66}.

All the ALD processes in this thesis were carried out at Ghent University by Dr. Shaoren Deng and Prof. Christophe Detavernier. Experimental parameters of the ALD processes used in this thesis are listed in Table 4¹⁵². For the ALD of TiO₂ onto CNSs, as-grown CNSs on a Si substrate were loaded into a homemade ALD tool with a base pressure in the low 10^{-7} mbar range. The sample was placed onto a chuck and heated to 100 °C. Tetrakis (dimethylamido)

titanium (TDMAT) (99.999% Sigma-Aldrich) and O₃ gas generated by an ozone generator (Yanco Industries LTD) were alternately pulsed into the ALD chamber at pressures of 0.3 and 0.5 mbar, respectively. In the flux the concentration of the ozone was 145 µg mL⁻¹. 20 sec pulse time and 40 sec pump time were used for a conformal coating of TiO₂ on the entire CNSs and to prevent the occurrence of chemical vapor deposition-type reactions. In case of the ALD of TiO₂, ZnO and Al₂O₃, VO_x and Pt onto MWCNTs, the as-grown MWCNTs were similarly loaded into a homemade ALD system with a base pressure of 2*10⁻⁷ mbar, except for Pt a base pressure of 5*10⁻⁷ mbar was used. Metalorganic precursors and ozone were alternatively pulsed into the chamber while the MWCNT sample was heated up to 100 °C for TiO₂, ZnO and Al₂O₃, 150 °C for VO_x and 200 °C for Pt. Tetrakis-(dimethylamido)titanium (TDMAT) (99.9%, Sigma Aldrich), tetrakis-(ethylmethylamino) vanadium (TEMAV) (Air Liquide), diethylzinc (DEZn) (≥52 wt%, Sigma Aldrich), trimethylaluminum (TMA) (97%, Sigma Aldrich) and (methylcyclopentadienyl) trimethylplatinum (MeCpPtMe₃) (Sigma Aldrich) were used as metal precursors for TiO₂, VO_x, ZnO, Al₂O₃ and Pt, correspondingly. To achieve a conformal coating on the MWCNT forest, 20–40 sec precursor pulses at a pressure of 0.4–0.8 mbar were applied. The pumping time was chosen as twice the pulse time to ensure sufficient evacuation of the residual precursor vapor and reaction products, thus avoiding chemical vapor deposition inside the films. More details on the ALD processes applied to the materials studied in this thesis can be found in ¹⁵².

ALD process	Precursor I	Precursor II	Deposition Temperature	Pulse Time	Templates
TiO ₂	TDMAT, 0.3 mbar (s. p.)	Ozone, 145 µg/mL, 0.5 mbar (s. p.)	100°C	20 sec	CNSs
TiO ₂	TDMAT, 0.4 mbar (s. p.)	Ozone, 150 µg/mL, 0.5 mbar (s. p.)	100°C	20 sec	MWCNTs
Al ₂ O ₃	TMA, 0.4 mbar (s. p.)	Ozone, 150 µg/mL, 0.5 mbar (s. p.)	100°C	20 sec	MWCNTs
VO _x	TEMAV, 0.4 mbar (s. p.)	Ozone, 150 µg/mL, 0.5 mbar (s. p.)	150°C	20 sec	MWCNTs
ZnO	DEZn, 0.4 mbar (s. p.)	Ozone, 150 µg/mL, 0.5 mbar (s. p.)	100°C	20 sec	MWCNTs
Pt	MeCpPtMe ₃ , 0.8 mbar (s. p.)	Ozone, 150 µg/mL, 0.5 mbar (s. p.)	200°C	40 sec	MWCNTs

Table 4 ALD processes used in this work. *s. p.= static pulse

XRD is a technique utilizing the scattered X-rays at parallel crystal planes to identify the phases present inside the materials. For XRD studies under non-ambient conditions (changes in the ambient gas environment and/ or temperatures increases up to 1600°C), special modifications can be made to the XRD instruments. This enables the study of phase transformations induced by temperature or ambient gas change in a material, which is referred to as *in situ* XRD. In this work, both *In situ* and *ex situ* XRD measurements were carried out in a home modified Bruker D8 Discovery system (see Figure 36).

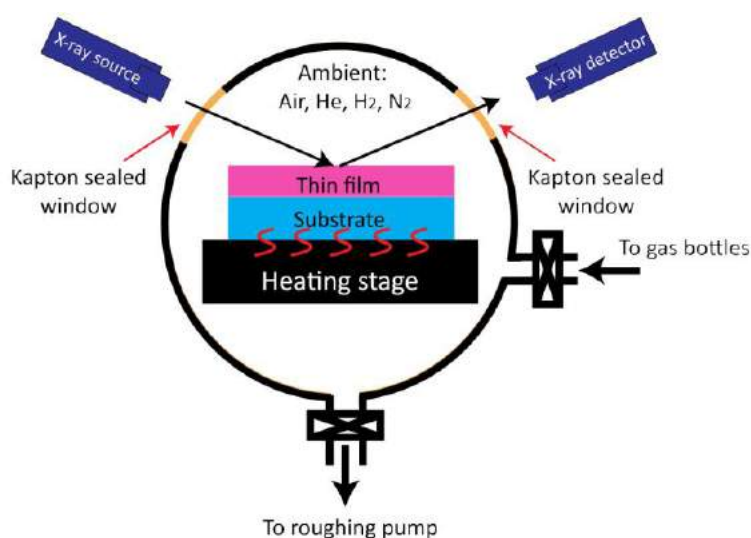


Figure 36 Schematic illustration of the *in situ* XRD setup¹⁵².

The annealing of the ALD processed CNSs and MWCNTs materials were conducted and simultaneously monitored by *in situ* XRD measurements performed at Ghent University by Dr. Shaoren Deng and Prof. Christophe Detavernier. The parameters of involved in the calcination processes of all the samples are given at Table 5.

ALD process	Calcination Temperature (°C)	Calcination Environment	Templates
TiO ₂	550	In air	CNSs
	600	In helium	
TiO ₂	500	In air	MWCNTs
	400-500		
Al ₂ O ₃	600	In air	MWCNTs
VO _x	450	In air	MWCNTs
ZnO	450	In air	MWCNTs
Pt	450	In air	MWCNTs

Table 5 Calcination procedures used in this work.

Chapter 5 SYNTHESIS AND CHARACTERIZATION OF PHOTOREACTIVE TiO₂/CARBON NANOSHEET MATERIALS

CONTENTS

CHAPTER 5 CHARACTERIZATION OF PHOTOREACTIVE TiO ₂ /CARBON NANOSHEET MATERIALS.....	83
5.1 INTRODUCTION	83
5.2 EXPERIMENTAL DETAILS.....	85
<i>SEM and TEM characterizations</i>	85
<i>Photocatalytic activity tests</i>	85
<i>Carbon nanosheets growth on silicon substrate</i>	86
<i>ALD-based synthesis and annealing of TiO₂ nanostructures</i>	86
5.3 RESULTS.....	88
<i>Post-ALD calcination in air environment</i>	88
<i>Post-ALD calcination in helium environment</i>	89
5.4 DISCUSSION.....	96
5.5 CONCLUSIONS	98

This chapter has been published as:

Mert Kurttepli, Shaoren Deng, Sammy W Verbruggen, Giulio Guzzinati, Daire J. Cott, Silvia Lenaerts, Jo Verbeeck, Gustaaf Van Tendeloo, Christophe Detavernier, Sara Bals, “Synthesis and Characterization of Photoreactive TiO₂–Carbon Nanosheet Composites”, **2014**, *The Journal of Physical Chemistry C*, Volume 118, Issue 36, Pages 21031-21037.

Sammy W Verbruggen, Shaoren Deng, Mert Kurttepli, Daire J Cott, Philippe M Vereecken, Sara Bals, Johan A Martens, Christophe Detavernier, Silvia Lenaerts, “Photocatalytic acetaldehyde oxidation in air using spacious TiO₂ films prepared by atomic layer deposition on supported carbonaceous sacrificial templates”, **2014**, *Applied Catalysis B: Environmental*, Volume 160, Pages 204-210.

Chapter 5 Characterization of photoreactive TiO₂/carbon nanosheet materials

This chapter reports the structural characterization of CNSs templates coated by titanium dioxide (TiO₂) using ALD. Also, the effects of post-deposition annealing in a helium environment on the final structure are investigated. In order to reach this goal, different TEM techniques are applied. It will be shown that the annealing of the ALD processed and CNSs templated TiO₂ layers in helium environment results in the formation of a porous, nanocrystalline and photocatalytically active TiO₂-CNSs film.

5.1 Introduction

Since the discovery of the photocatalytic splitting of water on a TiO₂ electrode under ultraviolet (UV) light, TiO₂ materials have been subject to extensive research for many promising applications, such as photovoltaics and photocatalysis^{164–166}. For such applications, the surface area and crystallinity are two important material properties which affect the photovoltaic and photocatalytic efficiency of mesoporous TiO₂ materials¹⁶⁷. In order to synthesize TiO₂ with a large surface area, a variety of methods has been employed, including sol-gel, magnetron-sputtering and chemical vapor deposition^{168–170}. As mentioned previously, ALD is an alternative method to produce TiO₂ with a large surface area using different template structures⁵. Amongst others, CNSs are widely used templates for metal/metal oxide depositions due to their distinct properties, such as high surface area. As illustrated in Figure 37-(A), CNSs consist of several graphene layers that are slightly curved at the nano-scale, which in return builds up the CNSs morphology that is highly corrugated at the micro-scale (see Figure 37-(B) and (C)). The presence of the CNSs between the substrate and TiO₂ coating also permits having a conducting pathway, which is attractive for photovoltaics and battery applications^{5,171}. It was previously found that post-deposition annealing of ALD-processed TiO₂ materials can lead to a phase transformation from amorphous to anatase-TiO₂, which is the phase that yields the most ideal photocatalytic properties¹⁷². On the other hand, the annealing environment is known to have a significant effect on the preservation of carbonaceous species. Post-deposition calcination in ambient air, which is a typical choice as an annealing environment for mesoporous TiO₂ materials, usually results in the removal of

carbonaceous species, such as CNTs, through air oxidation¹⁷³. Therefore, the use of different annealing environments, such as Argon and Helium, can be interesting, especially in those cases where preservation of carbonaceous templates are of concern.

In this chapter, we investigate the structure of TiO₂ deposited by ALD on CNSs templates. Also, the effects of post-deposition annealing in a helium environment are studied using different characterization techniques. The crystallization of the TiO₂ coating upon annealing is observed using *in situ* XRD (by Dr. Shaoren Deng and Prof. Christophe Detavernier, Ghent University). The influence of annealing on the structure and morphology of the ALD deposited TiO₂ layer is investigated by SEM and TEM. It will be here revealed that the annealing in helium results in the formation of a porous, nanocrystalline TiO₂-CNSs film. The photocatalytic activity of this material is evidenced through the degradation of acetaldehyde in the gas phase under UV illumination (by Dr. Sammy Verbruggen and Prof. Silvia Lenaerts, University of Antwerp), and the underlying mechanism is discussed.

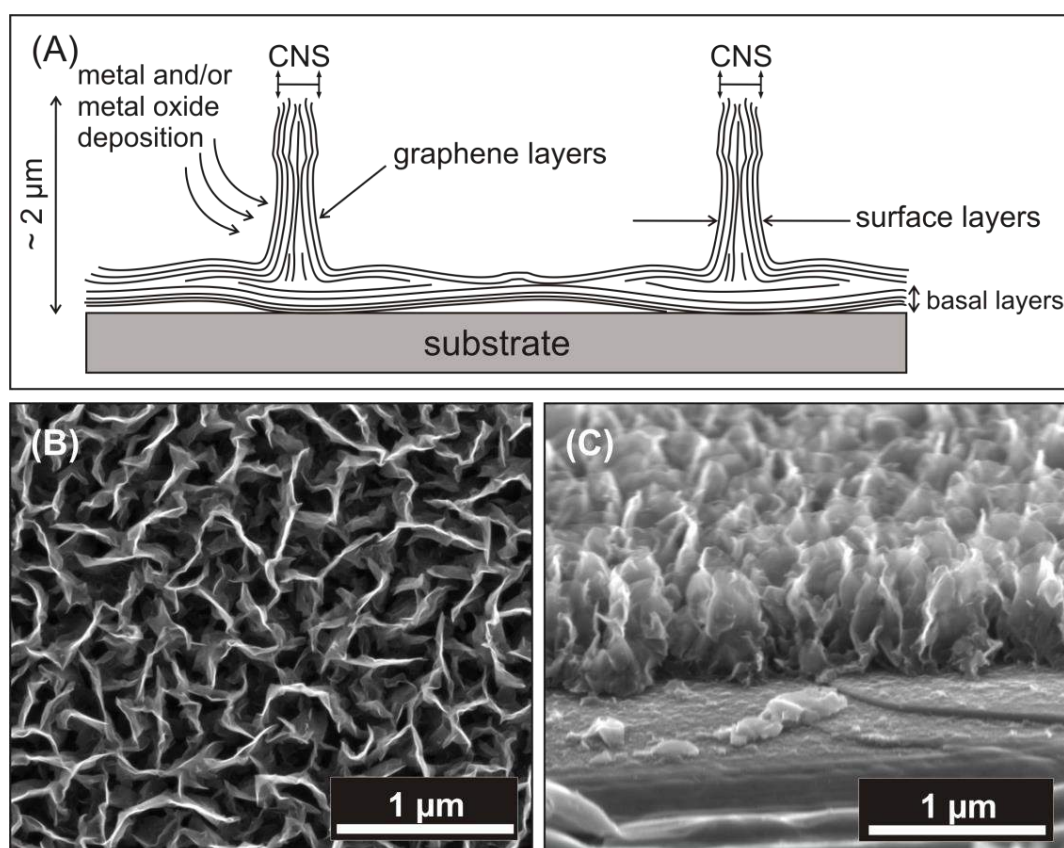


Figure 37 (A) Schematic figure of the CNSs structure. Both top-view (B) and cross-sectional (C) SEM images of pristine CNSs on Si substrate reveal a corrugated morphology.

5.2 Experimental details

SEM and TEM characterizations

SEM was performed using a FEI Helios NanoLab 650 dual-beam system to resolve the morphology of the films during the synthesis and after annealing. For TEM characterizations, several samples were prepared by crushing and cross-section samples, as described previously (see Section 2.2.1). BFTEM and HRTEM were performed using a FEI Tecnai F20 operated at 200 kV. HAADF-STEM images and EDX elemental maps were collected using an aberration corrected cubed FEI Titan operated at 300 kV, equipped with a Super-X detector for EDX analysis. EFTEM elemental maps were collected using a Philips CM30-FEG microscope operated at 300 kV.

Tilt series for electron tomography were acquired on cross-section TEM specimen with the aberration corrected cubed FEI Titan operated at 200 kV in combination with an advanced tomography holder from Fischione Instruments and the FEI XPlore3D acquisition software. Tilt series consisting of 71 HAADF-STEM images were acquired with tilt increments of 2° over a range of $\pm 70^\circ$ on cross-section TEM samples. Alignment of the data was carried out using the FEI Inspect3D software package. The reconstruction was performed using SIRT with 25 iterations implemented in Inspect3D. Amira (Visage Imaging GmbH) was used for the visualization of the reconstructed volume.

STEM-EELS experiments were carried out on cross-section TEM specimens using a double aberration corrected cubed FEI Titan operated at 120 kV, equipped with a monochromator to optimize the energy resolution for EELS measurements. Quantitative elemental maps were collected by subtracting a power law background from the spectra and fitting the corresponding core-loss excitation edges to reference spectra. The fitting for the acquired spectra was carried out using the EELSModel software package¹⁷⁴.

Photocatalytic activity tests

The evolution of the acetaldehyde concentration together with CO₂ formation as the degradation product was continuously monitored using on-line FTIR spectroscopy (by Dr.

Sammy Verbruggen and Prof. Silvia Lenaerts, University of Antwerp). More details on the photocatalytic test can be found in a previous study¹⁷⁵.

Carbon nanosheets growth on silicon substrate

CNSs samples used in this thesis were synthesized (by Dr. D. Cott, imec) through PECVD, as described previously. The morphology and structure of the as-grown CNSs (without TiO₂) were investigated by TEM. BFTEM confirm the presence of the corrugation observed for the nanosheets by SEM (see Figure 38-(A)). In order to investigate the interface between the Si substrate and the CNS in more detail, HRTEM images were acquired. Figure 38-(B) shows that the sheets are composed of several graphene layers both parallel (basal layers) and perpendicular (surface layers) to the substrate. The interplanar spacing between two layers corresponds to 0.34 nm, which is the typical distance between two graphene layers in graphite (see Figure 38-(B)-inset). EFTEM elemental mapping of carbon presented in Figure 38-(C) reveals the presence of carbon in the nanosheets.

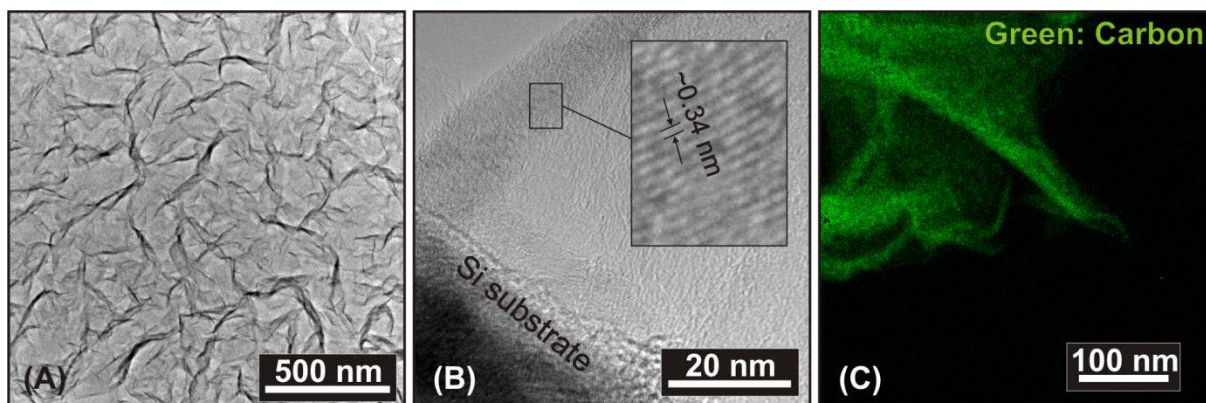


Figure 38 BFTEM image of CNSs presented in (A) reveals the corrugated morphology. The individual graphene layers of the CNSs are clearly seen in the HRTEM image (B) as shown at the inset. The EFTEM carbon elemental map in (C) indicates the presence of carbon.

ALD-based synthesis and annealing of TiO₂ nanostructures

The ALD process of TiO₂ onto CNSs was carried out at Ghent University (Dr. Shaoren Deng and Prof. Christophe Detavernier). The details of the ALD parameters can be found in Table 4. In total, 200 ALD cycles were applied on the CNSs template. The characterization of the resulting surface by SEM revealed that both the corrugation and the perpendicularity of the film relative to the substrate were preserved after ALD (see Figure 39-(A) and (B)). Figure

39-(C) presents a low magnification BF-TEM image, illustrating that the ALD process results in a fibrous structure. From the HRTEM images (Figure 39-(D)-inset and (E)), it can be seen that these structures consist of graphene layers surrounded by a thin, amorphous coating. The color-coded superposition of the titanium and carbon EFTEM elemental maps in Figure 39-(F) identifies these fibrous structures consisting of a carbon containing interior (CNSs) surrounded by a titanium containing coating (ALD processed TiO_2). It is also observed that there are parts at which the TiO_2 coating and the graphene layers are separated (See Figure 39-(D)). However, this might be attributed to the delamination of the TiO_2 coating from CNSs template during crushing, which could result in some interstitial voids in the material.

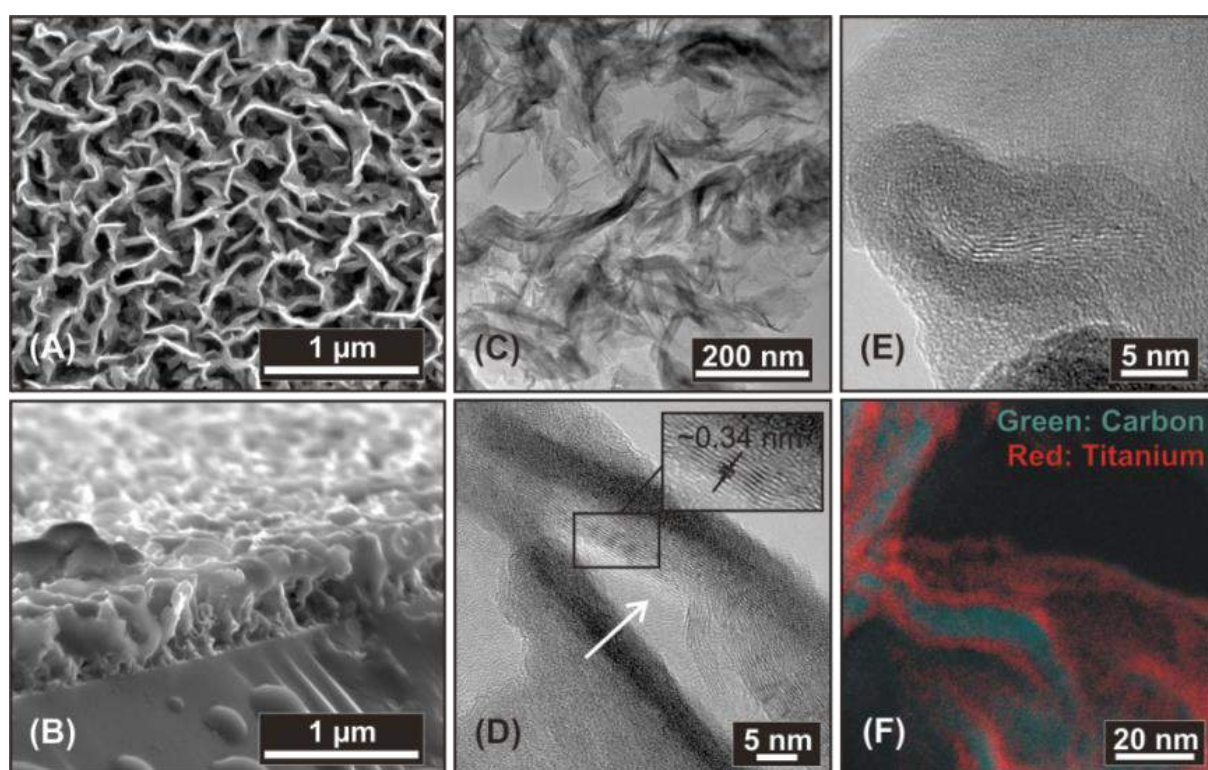


Figure 39 Top-view (A) and cross-sectional (B) SEM images of TiO_2 coated CNSs on Si. A low magnification BFTEM image is shown in (C). The amorphous TiO_2 coating and the graphitic layers of the CNSs are visible on the HRTEM images in (D) and (E). The separation of the TiO_2 coating and the graphene layers is indicated by an arrow. The carbon and titanium content of the nanosheets are presented in (F) at the color-coded EFTEM elemental map.

The occurrence of the phase transformations in the TiO_2 films upon annealing was monitored using *in situ* XRD with a dedicated Bruker D8 system¹⁷⁶ at the Ghent University. The sample was annealed from 20°C to 600°C at a rate of 1°C per minute in helium and this process was monitored by a K-type thermocouple. Once the temperature of 600°C was reached, the sample

was kept at this temperature for 3 hours while being illuminated by Cu K_{α} radiation (wavelength 0.154 nm). Diffracted X-rays were captured by a linear detector covering a range of 20° in 2θ set to a collection time of 5 sec.

5.3 Results

Post-ALD calcination in *air* environment

The number of cycles in ALD process is an important experimental parameter, which determines the total content of the deposited material. This, in return, leads to a difference in the performance of the material, for instance, in photocatalytic applications. Such effect was observed and reported in one of our previous studies¹⁷⁷. In order to prevent misunderstanding, it should here be kept in mind that this previous study was based on the TiO_2 ALD coated CNSs and MWCNTs in air environment rather than helium, where the latter will be reported in the following section. In this previous study, after calcination of the ALD processed films at $550^{\circ}C$ in air environment, CNTs and CNSs templates were removed and the as-deposited continuous amorphous TiO_2 layers transformed into a network of crystalline TiO_2 anatase nanoparticles, commensurate to the overall template morphology (see Figure 40-(B-E)). Subsequently, the photocatalytic activity of the TiO_2 films in relation to the number of ALD cycles and the type of template used (CNTs or CNSs) were investigated. The results are presented in Figure 40-(A). In both types of carbonaceous templates an initial increase in photocatalytic activity was observed with increasing amounts of deposited TiO_2 (i.e. increasing number of ALD cycles). However, further increase in ALD cycles was observed to cause excessive amounts of TiO_2 , which then leads to less open films and consequently lower photocatalytic activities. The application of 100 ALD cycles led to the optimum amount of TiO_2 deposited on CNTs, where this sample showed the highest activity. However, concerning the films prepared using the CNS sacrificial template, only the sample with 200 cycles performed better than the reference PC500, in other words showing the optimum photocatalytic activity. Therefore, 200 ALD-cycles have been likewise applied on the CNSs template in this study, as stated earlier. To understand the connection between the physical properties and the structure, a structural characterization was performed using *in situ* XRD, SEM and TEM, which are shown in the following section.

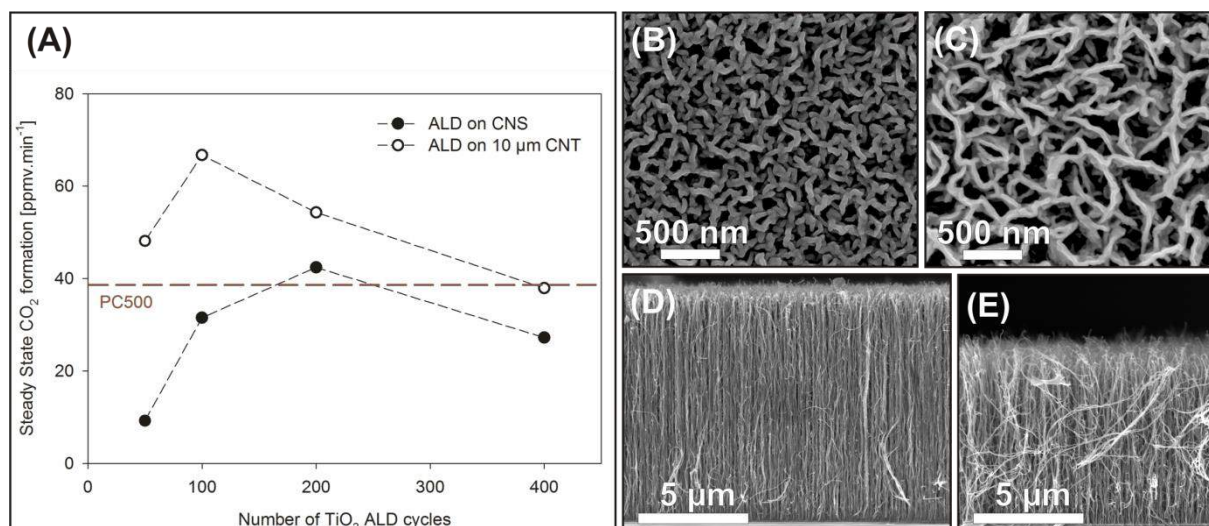


Figure 40 (A) Steady state CO₂ formation in function of the number of ALD cycles on CNSs (filled symbols) or CNTs (open symbols) by the photocatalytic mineralization of a continuous flow of 50 ppmv min⁻¹ acetaldehyde in air. The red dashed line represents the activity of the PC500 reference. SEM images of 200 TiO₂ ALD cycles on CNS template as deposited (B), after calcination (C). Cross section SEM images of 100 TiO₂ ALD cycles on CNT template as deposited (D), after calcination (E).

Post-ALD calcination in *helium* environment

In this present study, TiO₂ coated CNSs were annealed in helium environment while simultaneously monitoring the formation of different phases through *in situ* XRD. The results are presented in Figure 41-(A). It can be seen that the as-deposited TiO₂ film, which was gradually heated to a temperature of 600°C in He with a ramp rate of 1°C per min, starts to transform into crystalline anatase at a temperature of 425°C. The broad-band which is centered at $2\theta = 25.1^\circ$ corresponds to (101) crystallographic planes of the anatase phase. A preliminary characterization of the resulting film morphology was carried out using SEM (see Figure 41-(B)-(C)). From the images, it can be seen that the film consists of highly corrugated, interlaced sheets that are standing on the Si substrate. The comparisons of the as-grown and ALD-processed CNSs (see Figure 37-(B) and (C) and Figure 39-(A) and (B)) with the annealed films (see Figure 41-(B) and (C)) thereby disclose that the film morphology upon annealing was substantially preserved at the micro-scale and that neither ALD nor the post-deposition calcination led to a collapse of the structure. However, it should be noted that in general not all carbon nanosheets that grew upwards reached the full height equal to the average film thickness as observed by cross-sectional SEM study of as-grown CNSs (see

Figure 37-(C)). In fact due to 'overcrowding', many sheets stop growing or merge with another.

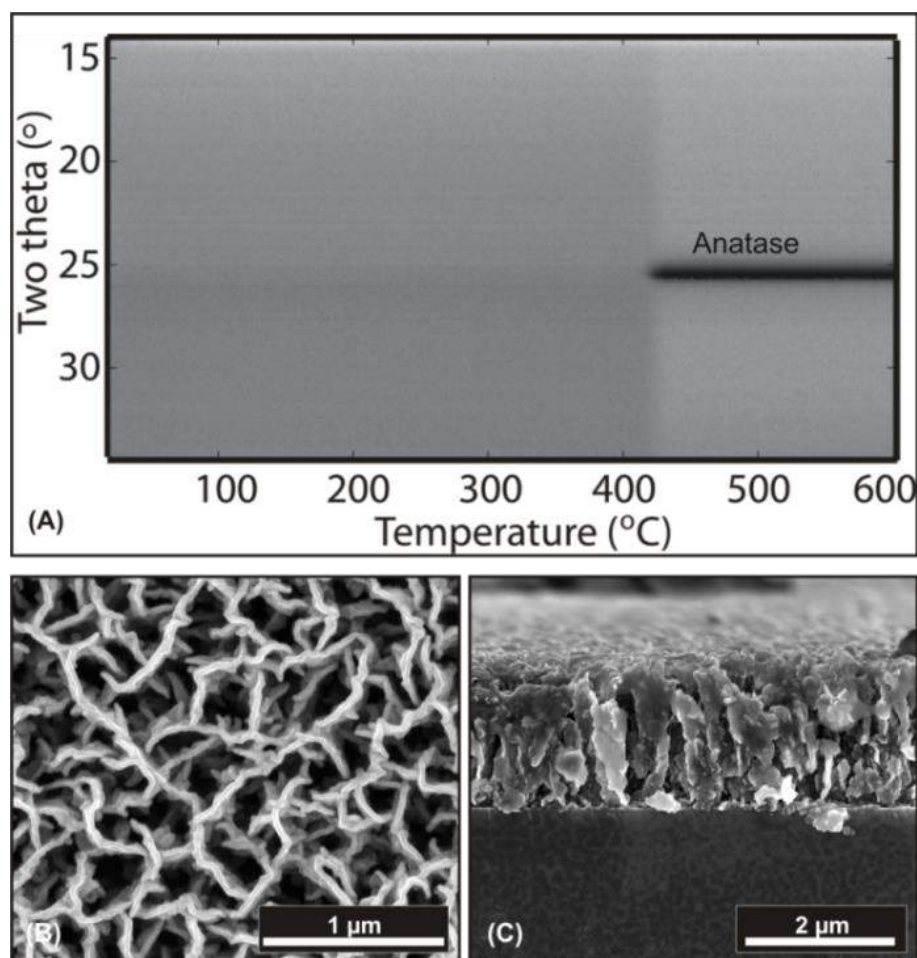


Figure 41 (A) *In situ* XRD data of TiO₂ coated CNSs heated at 1°C·min⁻¹ in helium ambient as a function of the temperature and diffraction angle 2 Θ . The appearance of the anatase phase is indicated. Top-view (B) and cross-sectional (C) SEM images of TiO₂-CNSs on Si.

A more detailed investigation of the film was performed using HRTEM. This study showed that the annealing changed the structure of the film remarkably at the nano-scale. HRTEM micrographs from locations in the vicinity of the Si substrate as well as the film surface (at inset) are presented at Figure 42. The micrographs show an interplanar spacing of 0.35 nm at the coating, corresponding to the (101) interplanar distance of anatase-TiO₂, and 0.34 nm inside the coating, which is the typical distance between two graphene layers in graphite. It is hereby observed that the annealed film contains anatase crystallites that are predominantly connected to the graphitic layers of CNSs, which is different compared to the as-deposited TiO₂ film that was observed to be amorphous (see Figure 39).

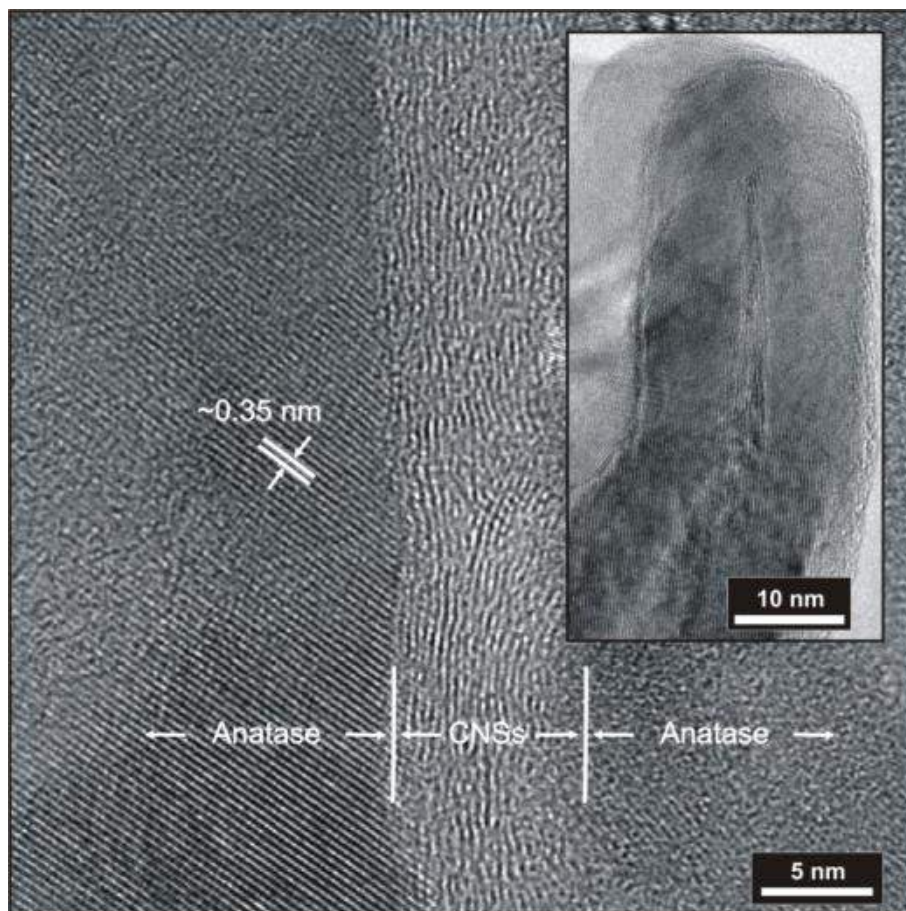


Figure 42 Anatase crystallites attached to graphite walls are visible on the HRTEM micrographs.

The chemical composition of the film was studied using EDX. From the HAADF-STEM image overlapped with the EDX map collected from the area indicated by the green square in Figure 43-(A), it is clear that the carbon containing layers are still present inside the titanium containing coating (See Figure 43-(B)). Such appearance of carbon within the film was attributed to the preservation of CNSs, as shown previously during HRTEM study. The high resolution HAADF-STEM image given in Figure 43-(C) additionally reveals that the crystallization of the amorphous coating started already around the carbon containing layer in vicinity of the Si substrate. Furthermore, a gap (~10 nm) between the Si substrate and the TiO₂ film is observed from the same image. The EDX map in Figure 43-(B) clearly points at the presence of carbon in this region. In HAADF-STEM imaging mode, the high-angle scattering scales with Z , where Z is the atomic number of the element under the electron beam. Therefore, the appearance of the gap stems from the presence of carbon at this region,

which has much lower atomic number compared to titanium. Moreover, an amorphous layer with a thickness of a few nanometers is observed on top of the silicon substrate.

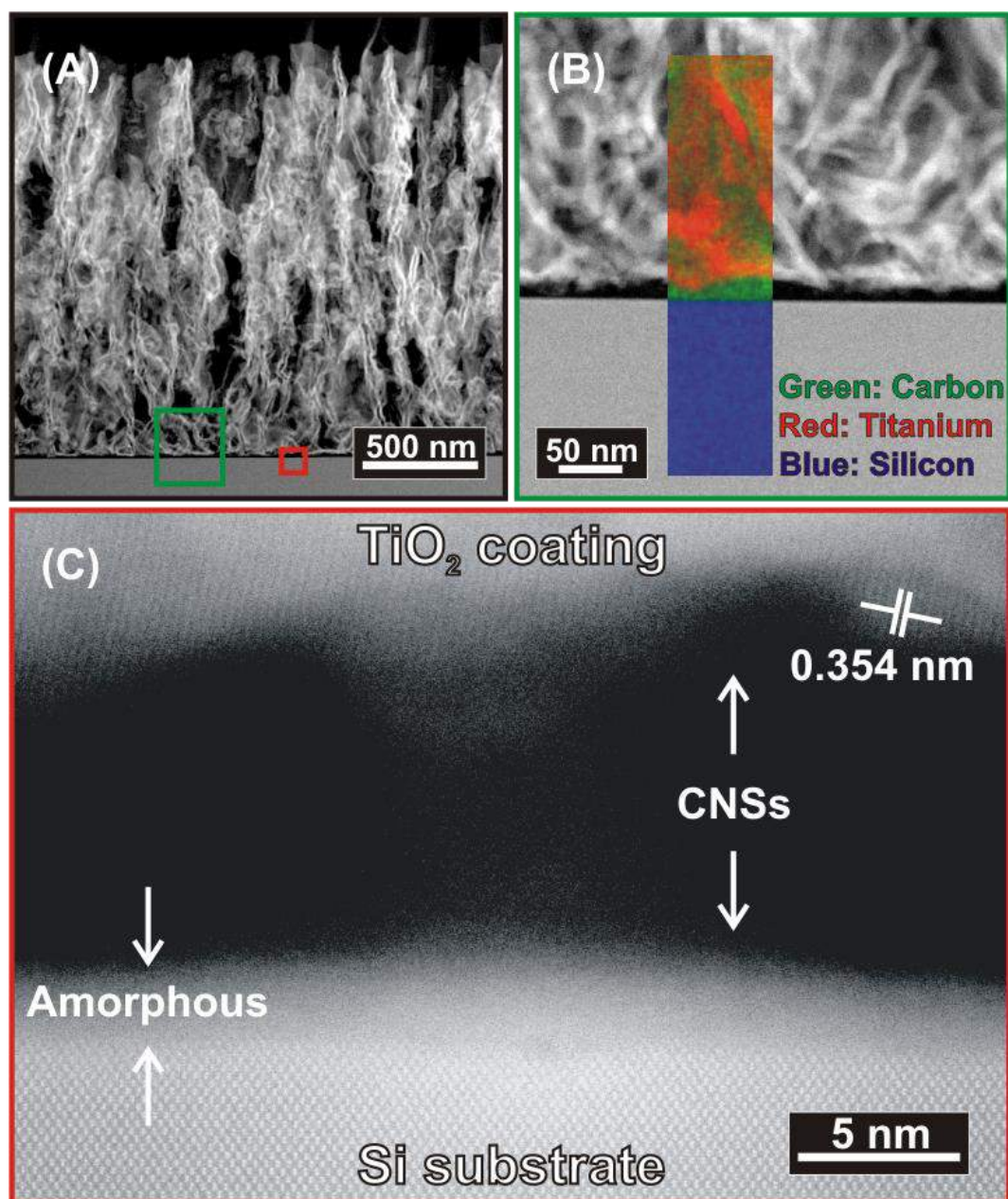


Figure 43 (A) Cross-sectional HAADF-STEM image. The carbon, silicon and titanium composition of the nanosheets can be seen on (B) EDX mixed color elemental map from region in (A) highlighted by green square. HAADF-STEM image (C) from a region highlighted by the red square at (A) reveals the crystallinity of TiO₂ coating.

To investigate the 3-D structure of the material, HAADF-STEM tomography was performed. A visualization of the 3-D reconstructed volume of TiO₂/CNSs film is shown in Figure 44-(A). The study revealed that the film yields a highly porous structure. An orthoslice acquired

through the 3D reconstruction and perpendicular to the substrate is displayed in Figure 44-(C). The orthoslice indicates the fibrous appearance of the film, which originates from the fine TiO_2 layer surrounding the preserved CNSs upon annealing. As mentioned previously, due to 'overcrowding' many sheets stop growing or merge with one another. Therefore, there is a denser CNSs content closer to the substrate than at the surface of the film. This contributes to the slight change of the thickness of the ALD processed layer. In order to comment on the conformity and uniformity of the ALD processed TiO_2 layer, we examined several orthoslices from the xy -planes of the reconstructed volume in the z -direction. In this manner, we obtained the TiO_2 coating thickness distribution; starting from the silicon substrate and reaching to the film surface (see Figure 44-(B)). The results indicate that there is a small increase in mean coating thickness at the positions close to the Si substrate. This is followed by slight fluctuations of the mean value, until it reaches the film surface, where it tends to increase rapidly. Based on the orthoslices through the 3D reconstruction, the mean coating thickness was estimated to be 9.4 ± 2.3 nm.

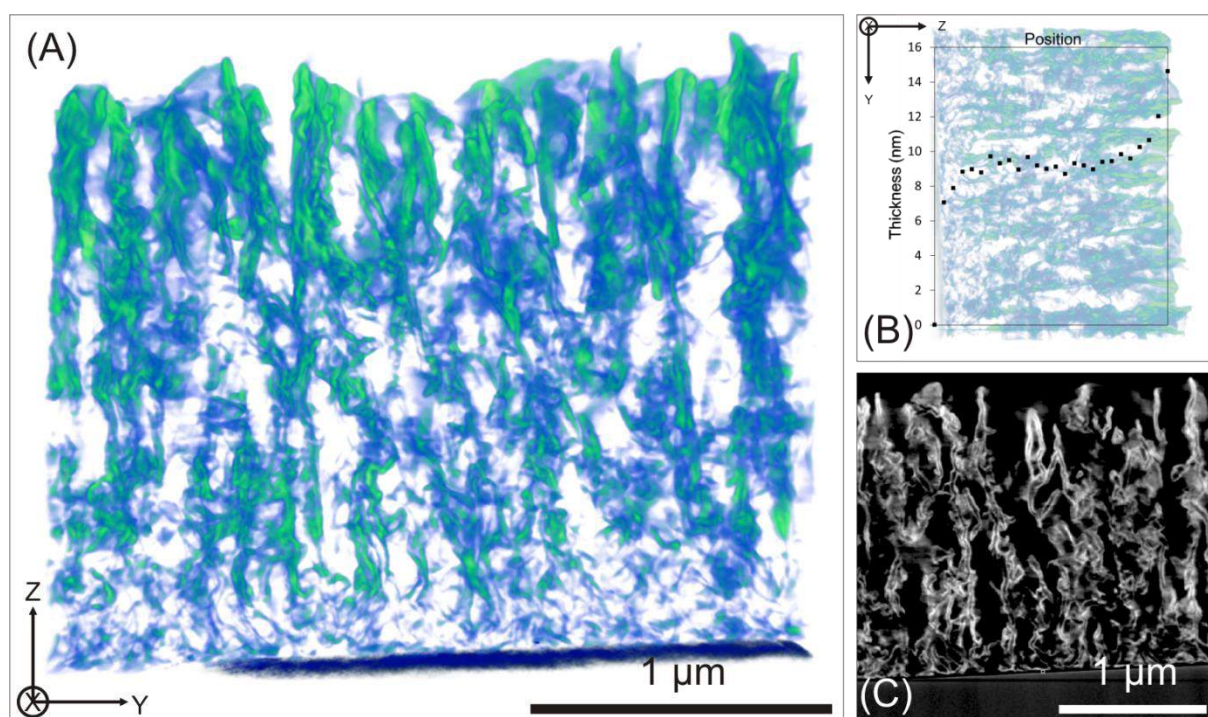


Figure 44 Visualizations of the 3-D reconstruction of the sample annealed in helium depicted along different orientations are given in (A) and (B). A slice (orthoslice) through the 3-D reconstruction is presented in (C).

In an earlier study, it was shown that the crystalline versus amorphous content in mesoporous materials can be measured by EELS¹⁷⁸. 2D STEM-EELS spectrum-images were accordingly acquired to investigate the spatial distribution of the elements and their phases within the sample. Quantitative elemental maps corresponding to titanium L_{2,3} and carbon K edges and the regarding color map with Ti-anatase (red) and graphitic C (green) of same region embedded on the HAADF-STEM image are given in Figure 45. By performing monochromated STEM-EELS characterization of the sample, areas with TiO₂ in anatase and amorphous forms and graphitic carbon have been identified. From these maps, it is observed that the coating is mostly in anatase form, and there is only a small amount of amorphous TiO₂ present after annealing (See Figure 45-(B) and (C)). From the quantification of the acquired spectra using EELSModel¹⁷⁴, it was determined that the content of the amorphous-TiO₂ layer corresponds to a percentage below 10%, and that the layer exhibits high crystallinity after annealing. The graphite distribution map additionally indicates the presence of graphite throughout the complete film inside the anatase-TiO₂ coating (See Figure 45-(D)).

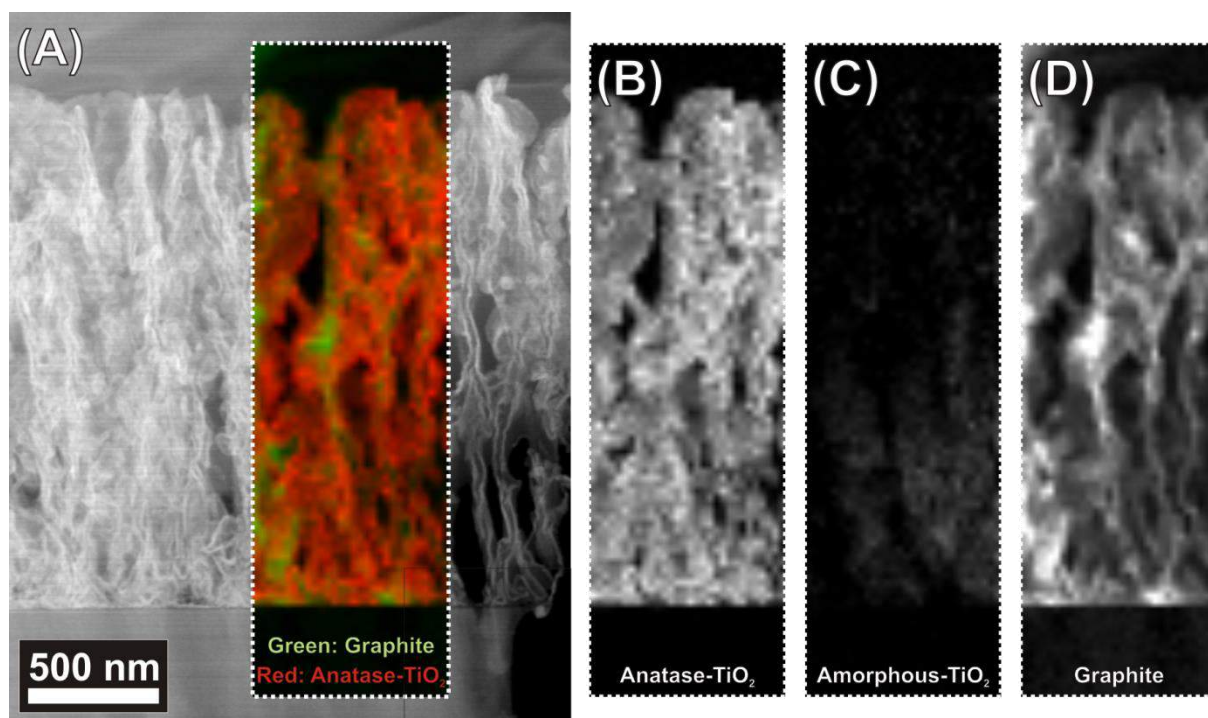


Figure 45 (A) HAADF-STEM overview image and colored elemental STEM-EELS map with (B) anatase-TiO₂ (red) and (D) graphite (green). The amorphous-TiO₂ elemental map is given in (C) for comparison with its anatase counterpart.

It has been previously mentioned that open, porous, rigid TiO₂ films would be of interest in many applications^{164–166}. As a proof of concept, the sample was tested for the photocatalytic degradation of acetaldehyde in a continuous gas flow. During the test, the continuous flow concentration profiles of acetaldehyde and CO₂ were measured at the reactor outlet monitored using on-line FTIR spectroscopy, as shown in Figure 46. Our results show that the sample exhibits a clear photocatalytic activity towards the degradation of acetaldehyde in the gas phase. From Figure 46, it can be seen that a drop in the acetaldehyde level coincides with a steep increase of the CO₂ concentration during UV illumination. Using recently established calibration curves, it was determined that the acetaldehyde concentration entering the reactor was $(13 \pm 1) \mu\text{L L}^{-1}$. The drop in the acetaldehyde concentration during UV illumination corresponds to $(2.5 \pm 1) \mu\text{L L}^{-1}$. The increase in CO₂ level was $(9.3 \pm 0.4) \mu\text{L L}^{-1}$. Assuming that every acetaldehyde molecule gives rise to two CO₂ molecules, this leads to a CO₂ excess of roughly $4 \mu\text{L L}^{-1}$ when the carbon balance is completed. In order to explain this excess CO₂, it should be considered that the sample was annealed in an inert gas atmosphere. Together with the black appearance of the sample, it is clear that a certain amount of (in)organic carbon is still present. It has also been previously shown that the carbon is present in graphitic form throughout the complete layer (see Figure 45). The excess in CO₂ production could therefore be attributed to the degradation of a graphitic carbon fraction present in the sample. This was confirmed by performing the same photocatalytic experiment as before, but in the absence of any pollutant (i.e. in air only). Indeed, a CO₂ production of $(3.8 \pm 0.4) \mu\text{L L}^{-1}$ was detected under these conditions. Correcting the results from Figure 46 with the latter observation, the steady state conversion of the $(13 \pm 1) \mu\text{L L}^{-1}$ acetaldehyde spiked air flow was calculated as $(21 \pm 2)\%$ at a total gas flow rate of $200 \text{ cm}^3\text{min}^{-1}$. This indicates that the sample is photocatalytically active and can be applied in the development of promising photocatalytic applications, when further optimized.

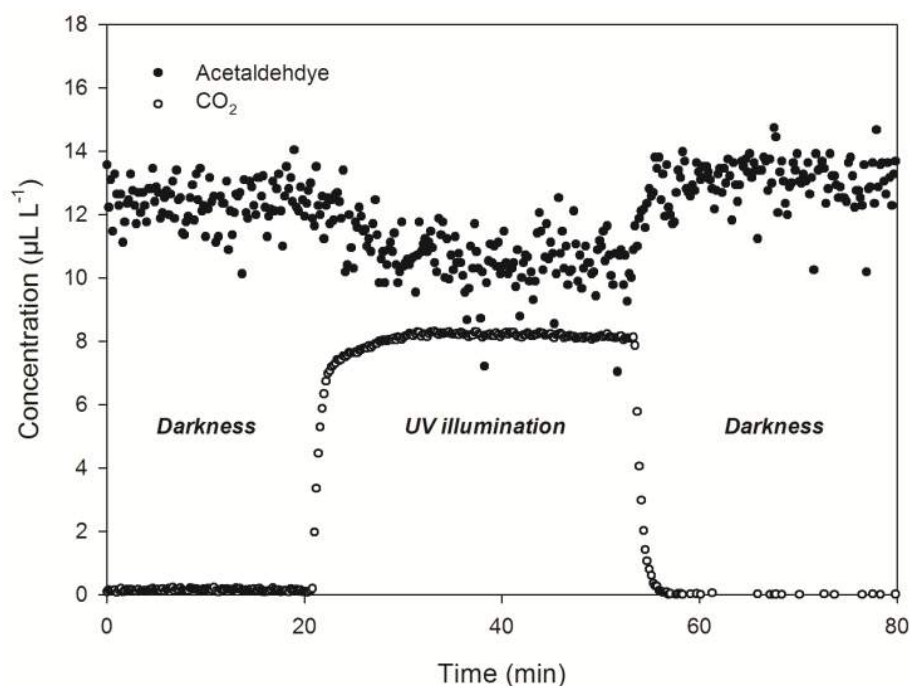


Figure 46 Continuous flow concentration profiles of acetaldehyde and CO₂ measured at the reactor outlet monitored using on-line FTIR spectroscopy. Dark and UV conditions are indicated in the graph.

5.4 Discussion

The characterization performed in this chapter shows that the ALD-process results in the formation of an amorphous TiO₂ coating surrounding the CNSs (see Figure 39). In a related study¹⁷⁹ in which TiO₂ films were grown from TiCl₄ and H₂O in a flow type low-pressure ALD reactor, it was demonstrated that crystalline anatase phase only appears at growth temperatures above 150°C. TEM measurements show that ALD of the TiO₂ on CNSs using TDMAT as precursor forms a fine, amorphous coating of TiO₂ at a growth temperature of 100 °C, which explains the lack of crystallinity of the as-deposited film.

The crystallinity of the TiO₂ film plays an important role at enhancing the photocatalytic activity¹⁸⁰ and charge transport and photocurrent in dye-sensitized TiO₂ solar cells¹⁸¹. The *in situ* XRD measurements indicate that the post-deposition annealing process modifies the film by a phase transformation from amorphous to crystalline anatase TiO₂ (see Figure 41-(A)). STEM-EELS characterization of the sample (see Figure 45) furthermore reveals that the TiO₂ film exhibits high crystallinity after annealing. In terms of the phase transformation, the

annealing of ALD processed TiO_2 shows resemblance to the annealing of TiO_2 nanostructured films deposited via sol-gel¹⁸² or magnetron sputtering¹⁸³ methods.

The annealed film, as shown by the electron tomograph presents a uniform, conformal TiO_2 coating. Electron tomography results indicate that the mean thickness of the coating only slightly varies throughout the film (see Figure 44-(B)). The small variation of the coating thickness can be ascribed to the inability of the precursor vapor to flow through the pores of the template surface which is blocked by the coating material during ALD¹⁵⁴. It is also worth mentioning that some graphene layers gradually merge into one sheet at the bottom of the film, thus creating pores or slots with very small openings. In this case, some interior spaces would not accept more ALD cycles since their bottle necks would be sealed by TiO_2 coating after e.g. 50 cycles¹⁸⁴. On the other hand, the porosity is known to be an important property for an efficient photovoltaic operation, which eases the penetration of light deep into the film. Based on the electron tomography results, it is revealed that the annealing of the ALD-processed film results in the formation of a highly porous structure.

With a deeper investigation performed through HRTEM (see Figure 42) and STEM-EELS (see Figure 45), it is discovered that the annealed film still yields graphene layers of CNSs in addition to the anatase crystallites formed at the walls of CNSs. For dye-sensitized TiO_2 solar cell applications, the preservation of the CNSs upon annealing in helium environment is particularly important, since this plays a significant role as a conducting template to facilitate charge transport in the films for improving the efficiency of nanostructure-based solar energy conversion devices consisting of CNTs/ TiO_2 systems^{185,186}. It is shown here that this can be obtained by annealing the film in helium environment. As a consequence, the potential of these materials in photovoltaic applications is obvious.

Such thin and porous TiO_2 films are of particular interest for several applications such as photocatalysis, as shown in Figure 46 for the photocatalytic degradation of acetaldehyde in a continuous polluted air stream. The morphology of the discussed sample is particularly well suited for gas phase applications, as it presents a very accessible, open and porous TiO_2 structure in mostly anatase form, offering a lot of available active sites¹⁸⁷.

5.5 Conclusions

In this study, the influence of annealing on ALD processed TiO₂ nanostructured film in an inert gas (helium) environment was investigated by TEM. The morphology of the film was visualized using conventional TEM imaging techniques, whereas the complex 3D structure of TiO₂ nanostructured films was revealed by HAADF-STEM electron tomography. The annealing was found to cause the ALD processed film to undergo a phase transformation from amorphous to anatase TiO₂. The calcination resulted in highly crystalline TiO₂ nanostructures with a porous network and a large surface area, which are desirable properties for photocatalytic and photovoltaics applications. TEM characterization indicated that the removal of carbon nanosheets template is hindered, and thin, porous, nanocrystalline and photocatalytically active TiO₂-CNSs film is produced.

Chapter 6 TEM INVESTIGATION OF POROUS

NANOSTRUCTURED METAL OXIDES SYNTHESIZED THROUGH ATOMIC LAYER DEPOSITION ON A CARBONACEOUS TEMPLATE FOLLOWED BY CALCINATION

CONTENTS

CHAPTER 6 TEM INVESTIGATION OF POROUS NANOSTRUCTURED METAL OXIDES SYNTHESIZED THROUGH ATOMIC LAYER DEPOSITION ON A CARBONACEOUS TEMPLATE FOLLOWED BY CALCINATION	101
6.1 INTRODUCTION	101
6.2 EXPERIMENTAL DETAILS	102
6.3 RESULTS AND DISCUSSION	102
<i>Al₂O₃ hollow nanotubes</i>	103
<i>TiO₂ nanoparticle chains</i>	104
<i>V₂O₅ and ZnO network of interconnected nanoparticles</i>	107
<i>Kinetics of carbon removal</i>	112
6.4 CONCLUSIONS	113

This chapter has been published as:

Shaoren Deng, Mert Kurttepli, Daire J Cott, Sara Bals, Christophe Detavernier, “Porous nanostructured metal oxides synthesized through atomic layer deposition on a carbonaceous template followed by calcination”, **2015**, *Journal of Materials Chemistry A*, Volume 3, Issue 6, Pages 2642-2649.

Chapter 6 TEM investigation of porous nanostructured metal oxides synthesized through atomic layer deposition on a carbonaceous template followed by calcination

Porous metal oxides with nano-sized features attracted intensive interest in recent decades due to their high surface area which is essential for many applications, e.g. Li ion batteries, photocatalysts, fuel cells and dye-sensitized solar cells. Various approaches have so far been investigated to synthesize porous nanostructured metal oxides, including self-assembly and template-assisted synthesis. For the latter approach, forests of MWCNTs are considered as particularly promising templates, with respect to their one-dimensional nature and the resulting high surface area. In this chapter, we systematically investigate the formation of porous metal oxides (Al_2O_3 , TiO_2 , V_2O_5 and ZnO) with different morphologies on MWCNTs using XRD, SEM accompanied by EDX and TEM. We focus on the morphological and structural transitions at the micro- and nano-scale during the calcination process in air environment. The crystallization temperature and the surface coverage of the metal oxides and the oxidation temperature of the carbon nanotubes were found to produce significant influence on the final morphology.

6.1 Introduction

Porous metal oxide nanostructures with high surface area are attractive for photocatalysis, dye-sensitized solar cell and lithium ion battery applications and have been investigated intensively in recent years^{188–190}. Various porous nanostructures can therefore be synthesized by ALD onto different porous templates such as peptides, anodized alumina, nanofibrillar aerogels, mesoporous block copolymers and MWCNTs. After template removal, TiO_2 nanotubes, RuO_2 nanotubes, Pt nanotubes and interconnected hollow metal oxide nanotubes were successfully synthesized^{191–195}. Usually, the removal of the CNTs results in hollow metal oxide tubes. However, in a previous study, the synthesis of photocatalytically active TiO_2 nanoparticle chain forests was demonstrated by coating MWCNTs with TiO_2 using ALD and subsequent calcination in air to remove the carbon⁶⁶. The resulting material offered a high photocatalytic activity towards the degradation of acetaldehyde under UV light¹⁷⁷. Such morphological transformations of various metal oxide layers deposited onto MWCNTs into

different resulting morphologies warrants further investigation. In this chapter, we systematically studied the calcination of Al_2O_3 , TiO_2 , V_2O_5 and ZnO ALD-coated vertically aligned MWCNTs in air environment and investigated the kinetics of the carbon removal and the morphological and structural changes at the micro- and nano-scale before and after calcination.

6.2 Experimental Details

Prior to MWCNTs growth, 70 nm TiN and 1 nm Co as catalysts were sputtered on an 8 inch Si wafer (Endura PVD tool, Applied Materials, USA). MWCNTs were synthesized at IMEC by Dr. D. Cott through catalyst-enhanced PECVD, as described previously. The ALD processes of TiO_2 , ZnO , Al_2O_3 and VO_x onto MWCNTs were carried out at Ghent University (by Dr. Shaoren Deng and Prof. Christophe Detavernier). The details of the ALD parameters can be found in Table 4. After ALD coating, the samples were calcined in air environment at a ramp rate of 5°C per min to remove the carbonaceous template. *In situ* XRD (adapted Bruker D8 system) was used to characterize the crystallization behavior during the calcination. SEM accompanied by EDX was performed using a FEI Quanta 200 F to resolve the morphology of the samples before and after annealing. TEM specimens were prepared by crushing (see section 2.2). BFTEM and HRTEM images as well as selected area electron diffraction (SAED) patterns were collected using a FEI Tecnai F20 operated at 200 kV. EFTEM elemental maps were obtained using a Philips CM30-FEG microscope operated at 300 kV. In addition, the crystallization temperature of metal oxide and oxidation temperature of MWCNTs were defined as T_{cry} and T_{ox} , respectively.

6.3 Results and Discussion

Forests of MWCNTs with a thickness of $6.5\ \mu\text{m}$ were coated with 100 cycles of Al_2O_3 , TiO_2 , ZnO and VO_x . After ALD, these samples were calcined at respectively 600°C , 500°C , 450°C and 450°C in air for 3 hours to remove the carbon. In Figure 47-(A)-(D), SEM images show that all samples still exhibit a forest-like structure at the micro-scale upon calcination. The thicknesses of Al_2O_3 , TiO_2 and VO_x coated CNT forest films measured from the images collected by SEM analysis are similar to the original thickness of the as-grown MWCNTs ($6.5\ \mu\text{m}$), but there is a noticeable shrinkage of the ZnO film ($4.7\ \mu\text{m}$). With the exception of the

minor changes in their thicknesses, there is no remarkable collapse observed in these films. EDX characterizations of the calcined samples indicated that these metal oxide forests are free standing nanostructures without the carbon support.

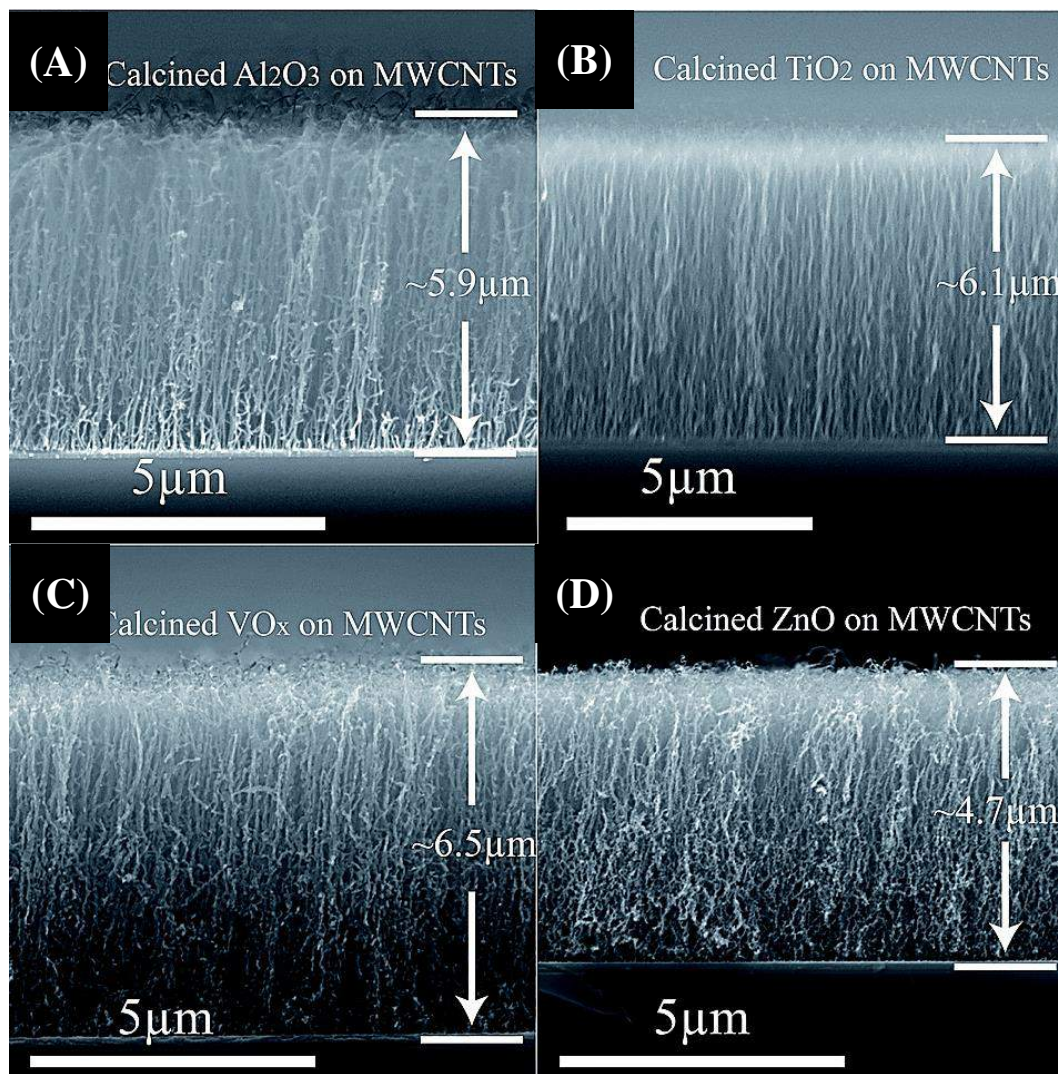


Figure 47 (A), (B), (C) and (D) SEM images showing the Al₂O₃, TiO₂, VO_x and ZnO coated MWCNTs after annealing in air, respectively.

Al₂O₃ hollow nanotubes

A detailed TEM study combined with EFTEM elemental mapping applied to the as deposited Al₂O₃ coated MWCNT sample shows that a uniform layer of amorphous Al₂O₃ was deposited on the surface of the MWCNTs (see Figure 48-(A)–(D)). The HRTEM image in Figure 48-(A) shows that the thickness of the Al₂O₃ coating on MWCNTs is smaller than a few

nanometers. The uncoated section of the MWCNT indicated in Figure 48-(B) by a circle in the color-coded EFTEM elemental map might be due to overlapping of neighboring MWCNTs during the deposition which hampers the exposure of this section to the precursors. After the deposition, the sample was annealed at 600°C in air for 3 hours to remove the MWCNTs. As can be seen in Figure 48-(E), hollow Al₂O₃ nanotubes were formed successfully. The calcination process appears to have no effect on the tubular morphology, which is in agreement with an earlier work¹⁹⁶.

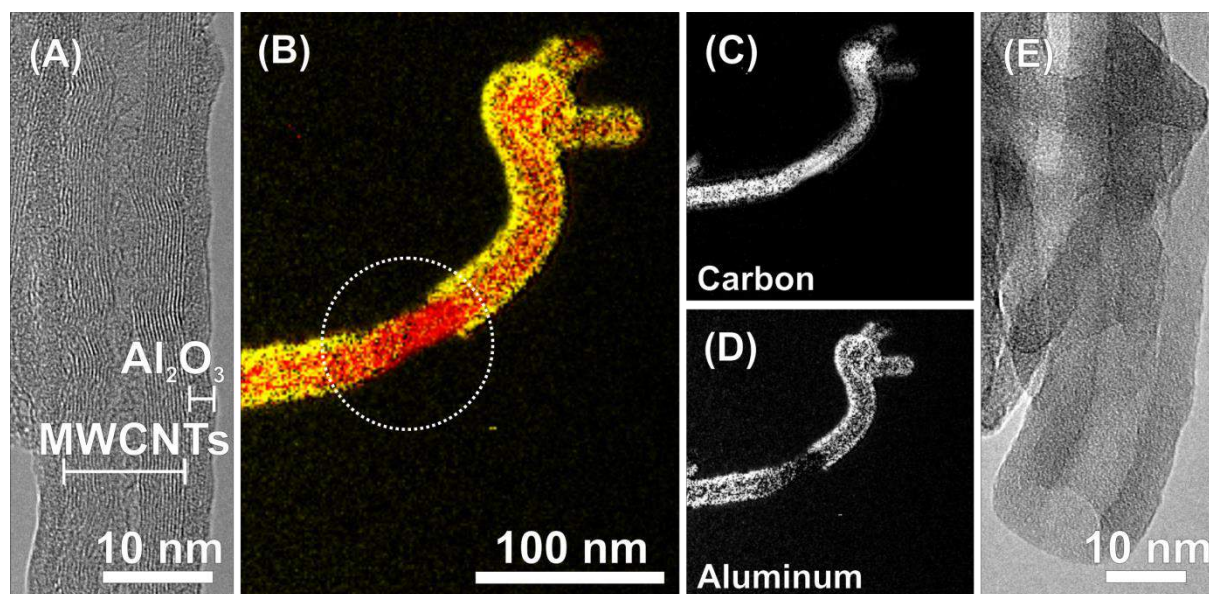


Figure 48 The amorphous Al₂O₃ coating and the graphitic layers of the MWCNTs are visible in the HRTEM image in (A). The carbon and aluminum contents of the nanotubes are presented in (B) showing the color-coded EFTEM map generated from individual (C) carbon (red) and (D) aluminum (yellow) elemental maps. A white circle in (B) indicates a part that is not coated by Al₂O₃. TEM image of Al₂O₃ nanotubes after annealing in air at 600°C for 3 hours is given in (E).

TiO₂ nanoparticle chains

Calcination of MWCNTs coated with continuous TiO₂ layers resulted in a remarkably different morphology at the nano-scale compared to MWCNTs coated with Al₂O₃ after the carbon removal. Figure 49-(A) indicates that prior to calcination in air, a continuous layer of amorphous TiO₂ is present at the MWCNTs. After the calcination, the TiO₂ coating surrounding the MWCNTs transforms into TiO₂ nanoparticles that are interconnected to each other. Figure 49-(B) indicates that these TiO₂ nanoparticles are fully solid and crystallized (e.g. not hollow).

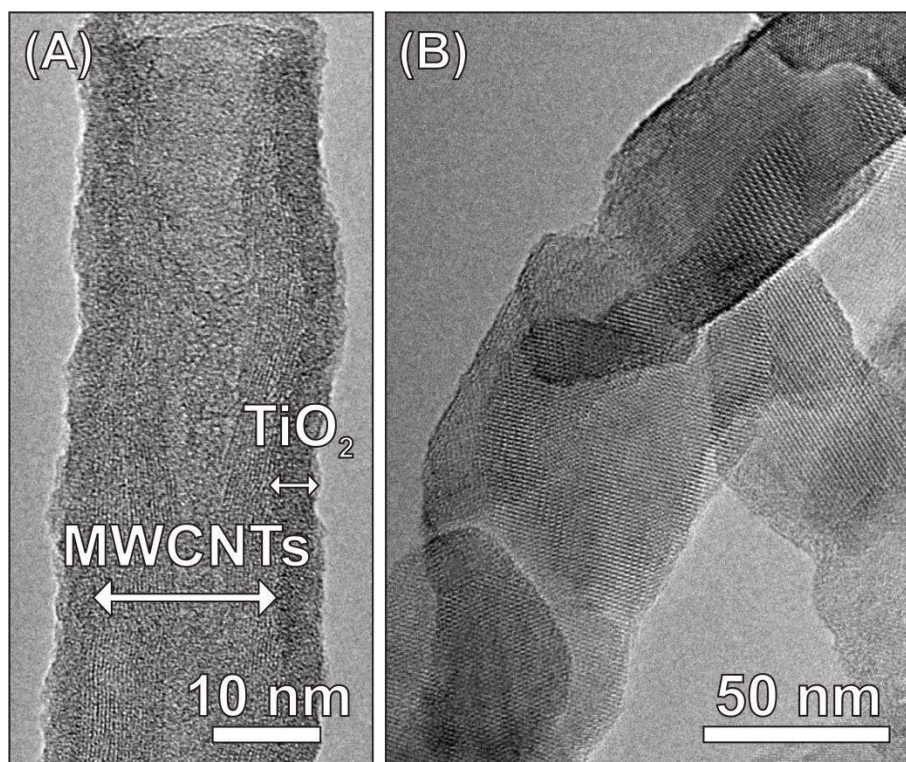


Figure 49 Amorphous TiO₂ coating and the graphitic layers of the MWCNTs are visible on the HRTEM image in (A). HRTEM image (B) after calcination reveals the crystalline TiO₂ nanoparticle chains.

To understand the evolution of this transformation, a detailed HRTEM characterization accompanied by chemical elemental mapping was carried out on samples that were quenched at different temperatures during calcination in air. According to the results of *in situ* XRD, the crystallization temperature (T_{cry}) of ALD TiO₂ coating is ~ 425 °C, as shown previously for ALD TiO₂ of CNSs (see Figure 41-(A)). Thus, a series of samples was made by taking quenches at 400, 425, 450 and 475 °C for HRTEM characterization. In this manner, the morphological transformation during calcination can be investigated. HRTEM images show that until 475 °C, the MWCNTs are still intact. However, for the sample quenched at 475 °C (Figure 50-(C)–(E)), the carbon content starts to decrease remarkably. As can be seen in Figure 50-(D) and (E), only a small amount of carbon is present inside the nanotube (indicated by white arrows). It should be noted here that the intense carbon signal (indicated by red arrows) stems from the holey carbon of the TEM grid. On the other hand, the TiO₂ coating retains its tubular shape. This indicates that the carbon removal precedes the morphological transformation. Figure 50-(A) shows that even though the TiO₂ coating is still surrounding the partly removed MWCNTs, the coating starts to transform from amorphous to continuous and

waved crystallized sections, with a rougher surface than that of the as deposited sample. As shown in Figure 50-(B), some hollow TiO_2 nanotubes already appear.

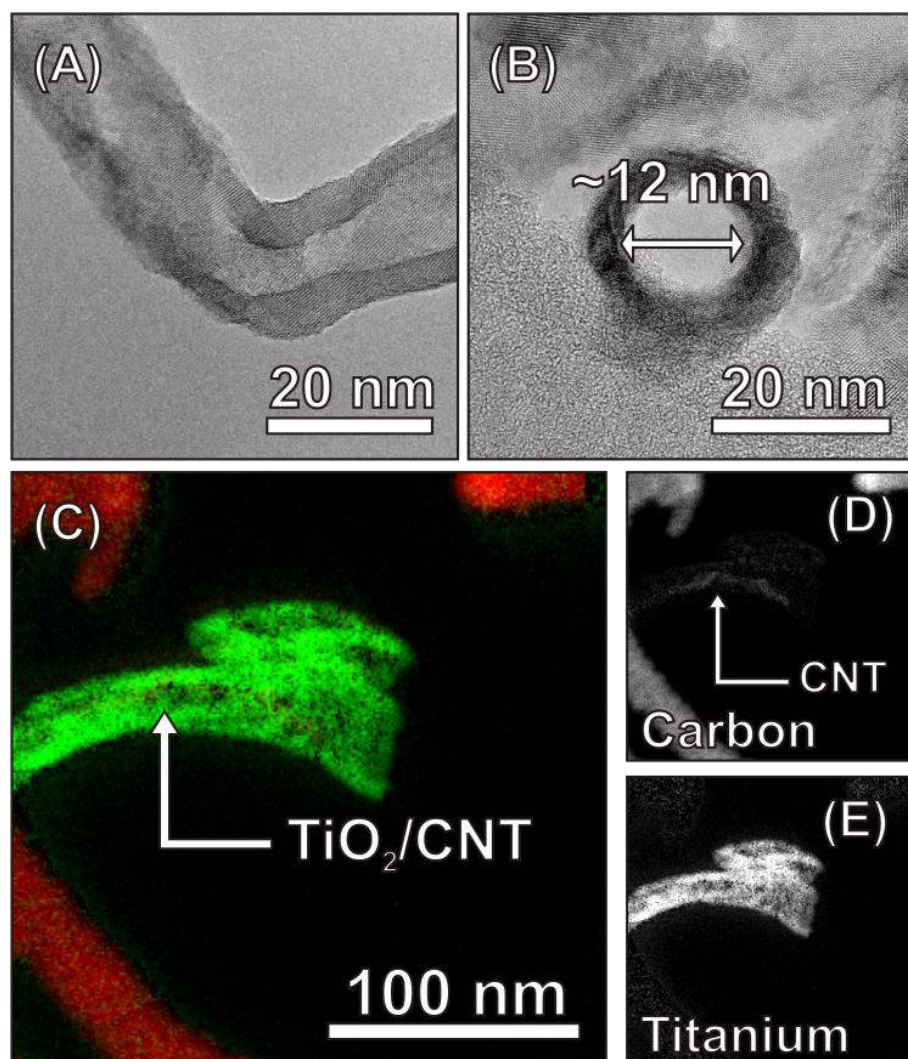


Figure 50 HRTEM images (A and B) of a 475 °C quenched sample show tubular morphology of TiO_2 coating. Carbon (red) and titanium (green) contents of the nanotubes are presented in (C) showing the color-coded EFTEM map generated from individual (D) carbon and (E) titanium elemental maps.

XRD results on these samples further reveal that the TiO_2 coating started crystallizing at a temperature 425°C and this crystallization proceeded more intensely at higher temperatures (Figure 51). It was expected that the calcination at 500°C in air for 3 hours is necessary to fully crystallize the TiO_2 . From the HRTEM analysis, we know that the transformation of TiO_2 from tubular coating to nanoparticles started from ~475°C, which is higher than the oxidation temperature (T_{ox}) of MWCNTs, which will be discussed further later on. Upon

exceeding this temperature, the crystallized TiO_2 sections began to sinter into interconnected nanoparticles when the MWCNTs were fully removed, causing the tubular morphology to collapse into chains of crystallized nanoparticles. Comparing with previous results of Al_2O_3 coated nanotubes; we can conclude that the lower T_{cry} of TiO_2 allows the sintering of crystallized TiO_2 into nanoparticles instead of maintaining a tubular morphology. The thickness of the coating and the diameter of the MWCNT are also important parameters in determining the final morphology. When the coating is too thick, merging of TiO_2 crystalline grains into nanoparticles is not likely since the tubular coating is thick enough to maintain its own structure. Also, when the tube is too thick, it will be more difficult for the metal oxide walls to merge together^{173,193,197}.

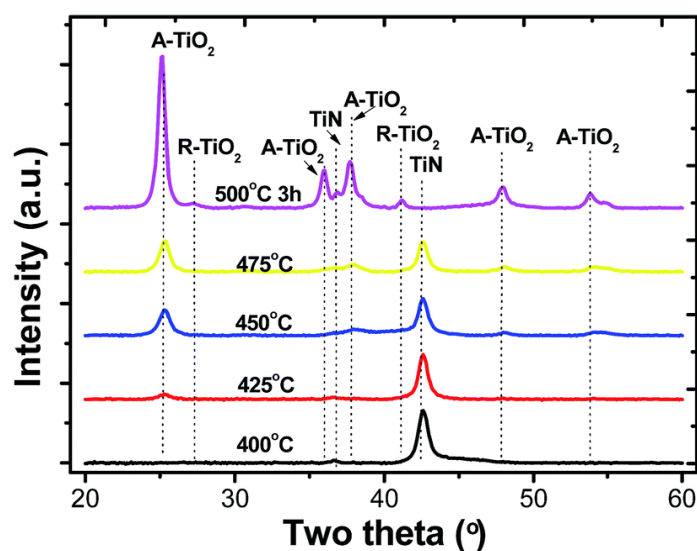


Figure 51 XRD patterns of TiO_2 coated MWCNT samples 400, 425, 450, 475 °C quenched and 500 °C calcined for 3 hours. A- TiO_2 and R- TiO_2 stand for TiO_2 of the anatase and rutile phases, respectively.

V_2O_5 and ZnO network of interconnected nanoparticles

When applying ALD on MWCNTs to synthesize porous metal oxides, the homogeneity of the initial coating is usually considered to be crucial for preserving the whole structure after carbon removal¹⁹⁸. If the metal oxide coating is discontinuous, the whole structure is generally expected to collapse after the carbon removal. However, the following results of synthesizing porous V_2O_5 and ZnO nanostructures using the same approach employed above show that a continuous and homogeneous coating is in fact not indispensable for structural preservation. HRTEM characterization together with element mapping on 100 ALD cycles of VO_x or ZnO

coated MWCNTs show that ALD resulted in a non-uniform coating of VO_x or ZnO on the surface of the MWCNTs, which is due to the inhomogeneity of the MWCNTs^{199,200}. Figure 52-(A)–(D) show VO_x layers on parts of the MWCNTs, whereas other sections remained uncoated (Figure 52-(D)). The HRTEM image in Figure 52-(E) (see the inset) shows that in some regions, the as deposited VO_x coating has already crystallized into the V_2O_5 phase.

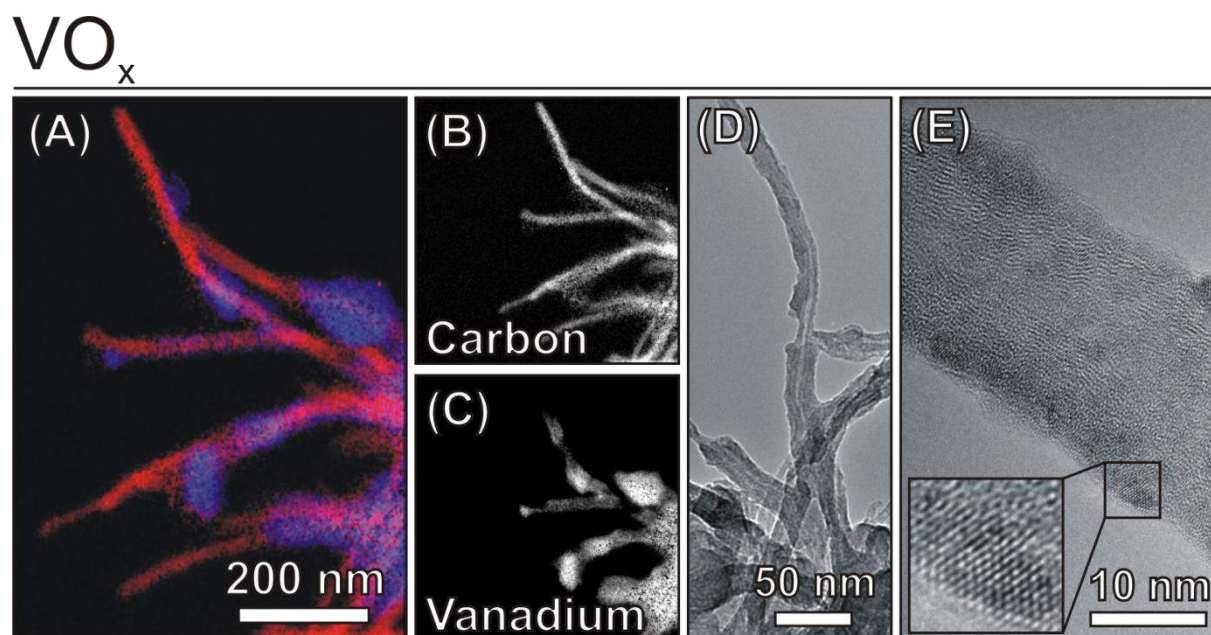


Figure 52 (A) EFTEM maps of carbon and vanadium in the VO_x nanotubes generated from individual (B) carbon (red) and (C) vanadium (dark blue) elemental maps. The TEM image in (D) depicts the uncoated and coated MWCNTs after ALD VO_x . (E) This HRTEM image reveals crystalline VO_x coating in some areas before calcination (see inset).

ALD of ZnO on MWCNTs shows similar results. ZnO nanoparticles are attached to the surface of MWCNTs (see Figure 53-(A)–(C)). The coverage of ZnO on the MWCNTs is even less than that of VO_x . Figure 53-(D) shows that the ZnO nanoparticles are already crystallized as deposited.

In order to remove the carbon, the samples were calcined at 450°C in air for 3 hours. SEM images in Figure 47-(E) and (F) show that after the calcination, the VO_x and ZnO samples still exhibit a similar forest like morphology at the micro-scale. The VO_x forest has the same overall thickness of $\sim 6.5\ \mu\text{m}$ as that of the original MWCNTs, whereas the ZnO slightly shrinks to $\sim 4.7\ \mu\text{m}$. However, in spite of the particle-type nature of the metal oxide ALD coating, the structures do not collapse or disintegrate upon removal of carbon.

ZnO

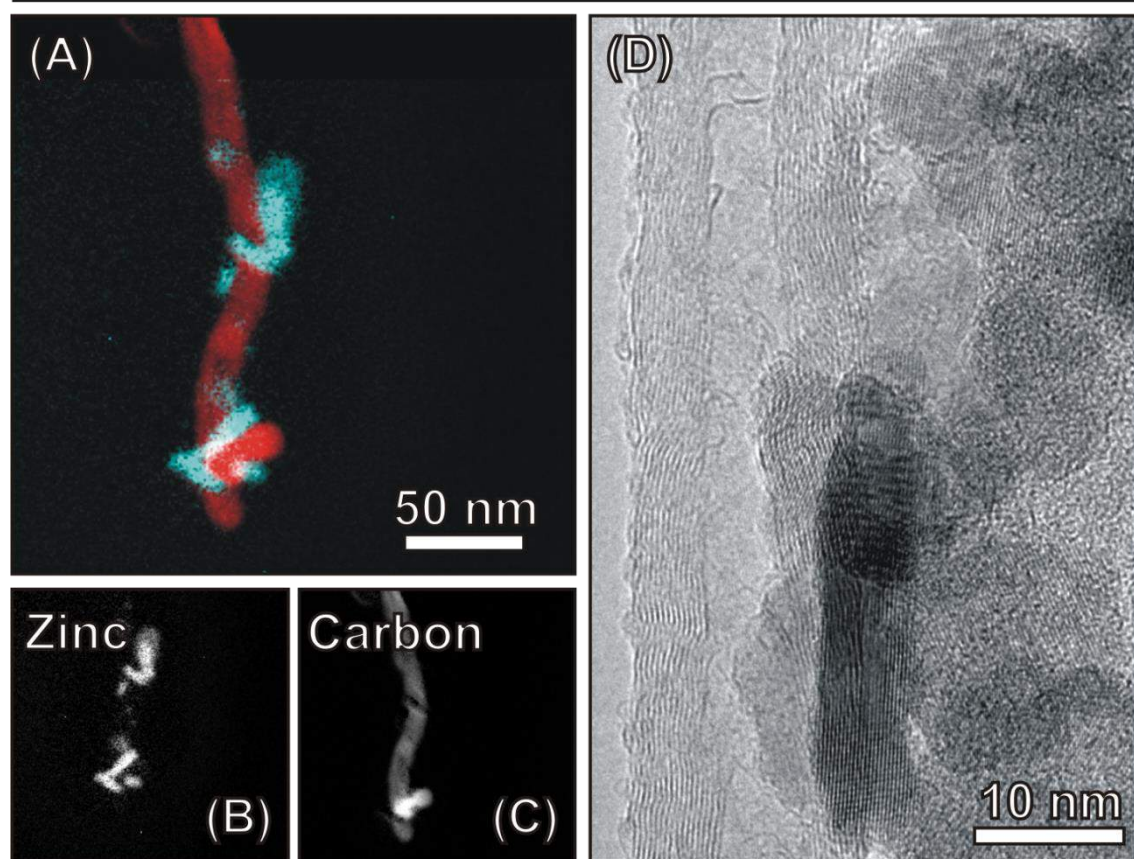


Figure 53 Carbon and zinc contents of ZnO nanotubes are presented in (A) showing the color-coded EFTEM map generated from individual (B) zinc (light blue) and (C) carbon (red) elemental maps. (D) This HRTEM image reveals crystallized ZnO nanoparticles attached to the surface of MWCNTs.

In situ XRD was used to monitor the crystallization behavior of these metal oxides when calcining these films in air from room temperature to 450°C. VO_x crystallized at approximately $T_{\text{cry}} = 290^\circ\text{C}$ showed no increase in grain size after crystallization (Figure 54-(A)). The final crystalline phase was confirmed to be V_2O_5 by *ex situ* XRD (Figure 54-(B)). In contrast, ZnO coatings did not show remarkable changes of the diffraction peaks during the calcination since they were already crystallized as deposited (Figure 54-(C)). The *ex situ* XRD result of the calcined sample in Figure 54-(D) confirms that these diffraction peaks are from the hexagonal ZnO phase. However, a notable intensification of the diffraction peaks of ZnO (100), (002) and (101) was observed in Figure 54-(C), which implies that there was an increase in the grain size of the ZnO coating. Based on the evolution of the diffraction peak at (101), we used the Scherrer equation²⁰¹ ($D = K\lambda/\beta \cos \theta$; where D is the mean grain size, K is

the crystallite shape factor, λ is the X-ray wavelength, θ is the Bragg angle and β is the pure diffraction broadening) to plot the variation of grain size *versus* calcination time, as shown in Figure 54-(E). The result shows that the initial grain size of the as deposited ZnO was about 10 nm and increased to ~80 nm during the calcination. As the calcination temperature increases, the ZnO grains grow, which implies a merging process of ZnO nanoparticles during the calcination.

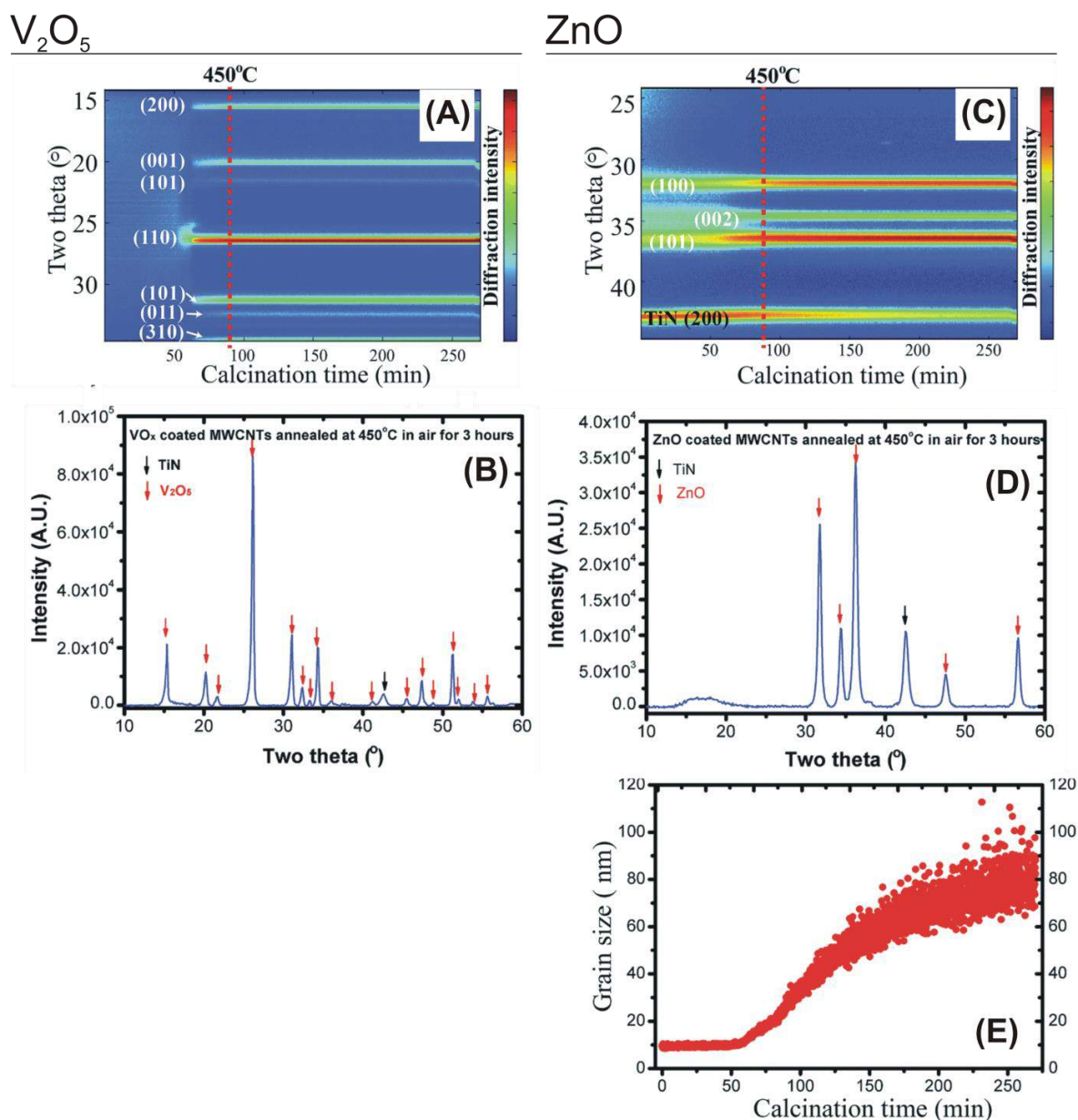


Figure 54 *In situ* XRD of VO_x (A) and ZnO (C) coated MWCNTs that were annealed from 20 to 450 °C at a ramp rate of 5 °C/min and isothermally held at 450 °C for 3 hours. *Ex situ* XRD results in (B) and (D) show the final crystalline phases of VO_x and ZnO samples after the calcination, respectively. The grain size of ZnO *versus* calcination time is shown in (E).

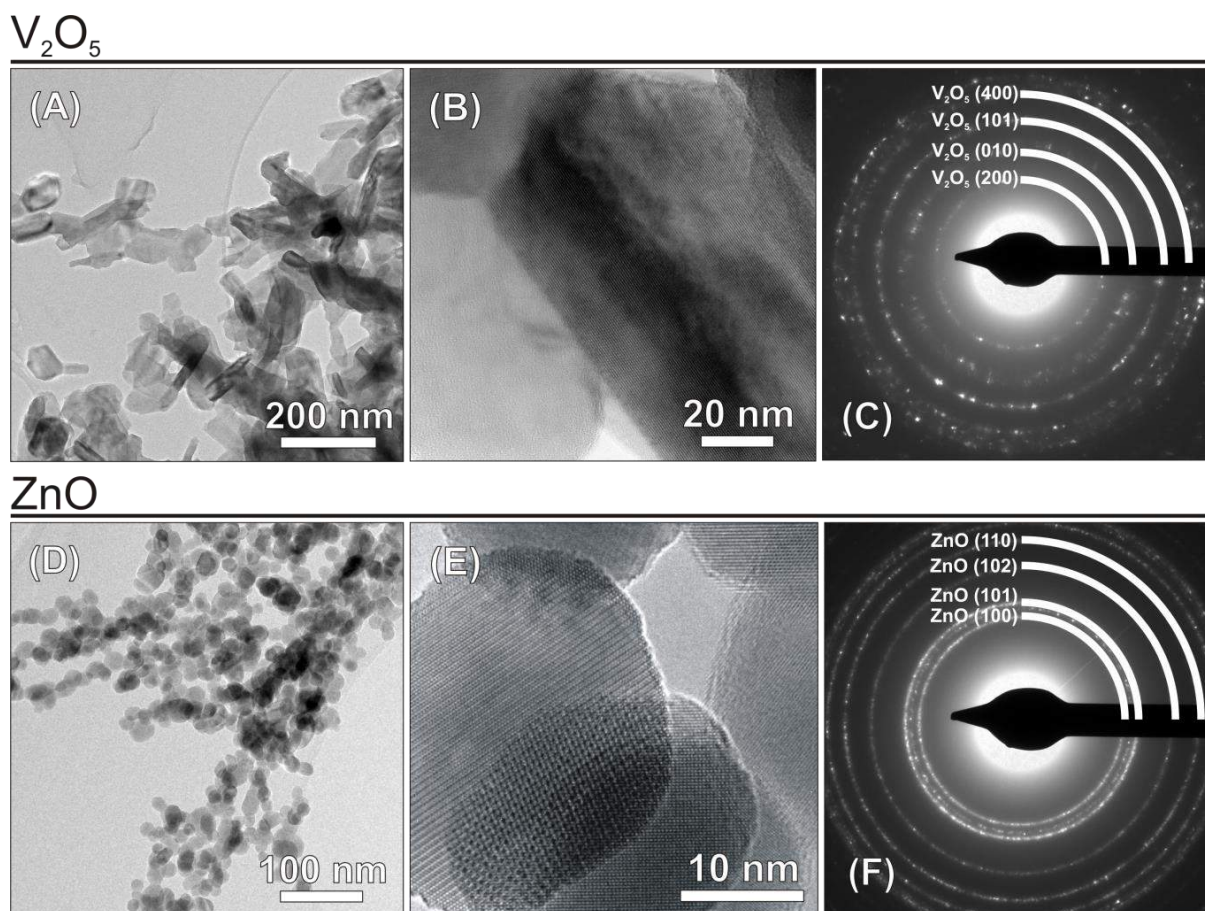


Figure 55 HRTEM images of the interconnected V_2O_5 nanorods after annealing VO_x coated MWCNTs in air (A and B). SAED pattern of crystallized V_2O_5 (C). HRTEM images of the interconnected ZnO nanoparticles after annealing ZnO coated MWCNTs in air (D and E). SAED pattern of crystallized ZnO (F).

To investigate the morphology of the VO_x and ZnO coatings after the calcination, HRTEM was carried out for these two films. Figure 55-(A) and (B) show that the VO_x coating crystallizes into interconnected V_2O_5 nanorods, with diameters of 20 to 80 nm and lengths of 60 nm to more than 100 nm. The electron diffraction rings in the SAED pattern of crystallized VO_x shown in Figure 55-(C) are indexed according to the various planes of the V_2O_5 phase. In the case of ZnO, as shown in Figure 55-(D) and (E), spherical ZnO nanoparticles with diameters ranging from 10 to 50 nm connect to each other in a similar manner as the V_2O_5 nanorods, indicating that during the carbon removal the initial separate nanoparticles connected to each other and grew into larger particles. The SAED pattern in Figure 55-(F) confirms that these ZnO nanoparticles are crystalline. The coverage of ZnO nanoparticles on the MWCNTs is lower in comparison to the coverage of VO_x , explaining the shrinkage (from ~ 6 to ~ 4.7 μm) of the film after calcination compared to the film of V_2O_5 nanorods, as

shown in Figure 47. Even though a uniform coverage of metal oxide on the MWCNTs may facilitate structure preservation during carbon removal, the examples of VO_x and ZnO clearly demonstrate that calcination of samples with a non-continuous coating can also result in a supportless nanostructure of porous metal oxide through merging and sintering of the separate nanoparticles into 3D interconnected networks during the calcination.

Kinetics of carbon removal

We systematically investigated the oxidation temperatures of MWCNTs coated with Al_2O_3 , TiO_2 , ZnO and VO_x by using EDX to record the carbon signal at different quenches of the samples during calcination in air, as shown in Figure 56-(A) and (B). In Figure 56-(A), MWCNTs were coated with 100 ALD cycles of Al_2O_3 , TiO_2 , ZnO and VO_x respectively and annealed from room temperature to 600°C . Several quenches at different temperatures with 50°C intervals were performed for EDX measurement. For pure MWCNTs without metal oxide coating, T_{ox} is found to be $\sim 500^\circ\text{C}$. Upon coating with metal oxides, T_{ox} of MWCNTs changes accordingly. TiO_2 and VO_x coated MWCNTs have a $\sim 50^\circ\text{C}$ decrease in T_{ox} whereas for ZnO coated MWCNTs T_{ox} shows a $\sim 100^\circ\text{C}$ decrease^{60,198}. However, a $\sim 50^\circ\text{C}$ increase of T_{ox} is observed for the Al_2O_3 coated samples.

Different numbers of ALD cycles were also applied to investigate the effect of the thickness of the metal oxide coating on T_{ox} . In Figure 56-(B), carbon signals measured by EDX for 50, 100 and 200 cycle TiO_2 and Al_2O_3 coated MWCNTs are shown. For TiO_2 coated MWCNTs, the T_{ox} values are independent of the thickness of TiO_2 . For the Al_2O_3 coated MWCNTs, the thicker the Al_2O_3 layer, the higher the T_{ox} . For 200 cycles of Al_2O_3 , removal of the carbon is not yet complete, even though the quench is taken at 650°C . The decrease in T_{ox} of MWCNTs can be attributed to the catalytic effect of coated metal oxides. Aksel *et al.* proposed a possible mechanism for explaining this catalytic effect¹⁹⁸. First the oxygen in the metal oxide reacts with the carbon of the MWCNTs and generates CO and an oxygen vacancy in the metal oxide layer. Then oxygen vacancies migrate to the gas–solid interface and are occupied with oxygen from the ambient atmosphere. The results shown in Figure 56-(A) are in agreement with this hypothesis. However, the results in Figure 56-(B) show that the uniformity of the thin film coating also influences the oxidation temperature. If the layer of metal oxide is not dense

enough *e.g.* TiO₂ compared to Al₂O₃, increasing the thickness does not increase the oxidation temperature of the MWCNTs, since pin holes probably allow oxygen vacancies to migrate to the gas–solid interfaces. Comparing Figure 48-(A) with Figure 49-(A), the TiO₂ coating on the MWCNTs is less uniform than the Al₂O₃, which implies that the uniformity and the quality of Al₂O₃ coating are better than those of TiO₂ and would have fewer pin holes. On the other hand, compared to other methods of coating metal oxides on MWCNTs, ALD is a well-known technique for the growth of higher quality metal oxides. Given a perfect starting surface, ALD will grow a metal oxide layer with limited pinholes. An increase of oxidation temperature was found when TiO₂ was deposited by ALD on oxygen plasma treated MWCNTs, which have a more defective surface and are easier for TiO₂ to nucleate and form ALD coating with a higher quality²⁰².

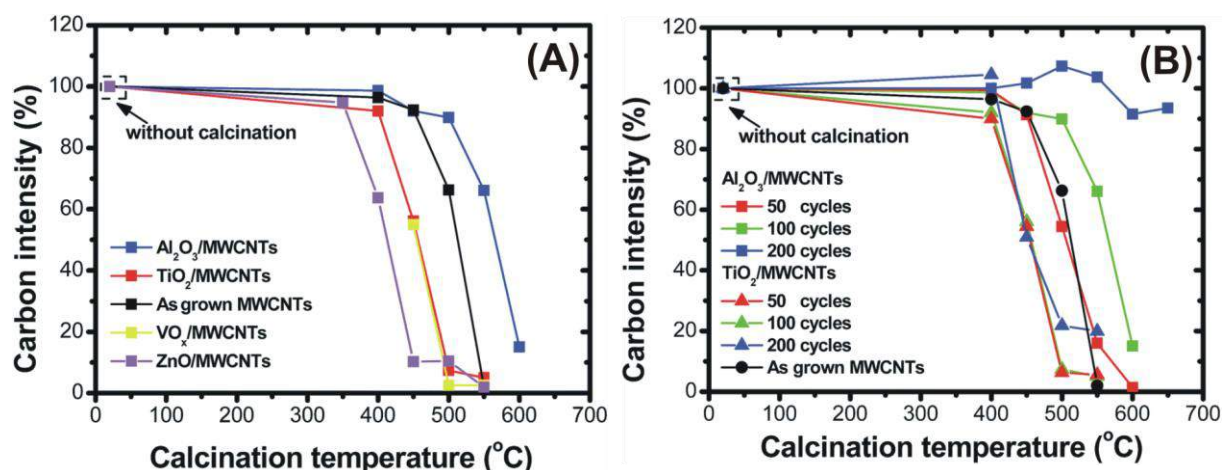


Figure 56 (A) EDX measured carbon contents of Al₂O₃, TiO₂, VO_x and ZnO coated MWCNTs with 100 ALD cycles quenched at different temperatures. The result of referenced uncoated MWCNTs is also shown. (B) EDX measured carbon contents of Al₂O₃ and TiO₂ coated MWCNTs with 50, 100 and 200 ALD cycles quenched at different temperatures. The result of referenced uncoated MWCNTs is also shown.

6.4 Conclusions

To summarize, by using TEM, a thorough understanding was obtained concerning the formation of nanostructured metal oxides by ALD deposition of metal oxides on MWCNTs and subsequent calcination. The process of morphological transformation during calcination is sketched according to T_{cry} and T_{ox} , as indicated in the scheme. From the systematic investigation above we can conclude that:

(i) For crystalline oxides (*i.e.* when calcining at temperatures higher than T_{cry}), sintering becomes a key mechanism during the calcination and determines the final morphology. For the TiO_2 sample, the driving force to reduce the surface area in combination with a sufficient mobility of the atoms causes a collapse of the hollow tube nanostructure into chains of anatase nanoparticles.

(ii) As illustrated by the examples of VO_x and ZnO , a continuous coating of the MWCNTs is not indispensable for avoiding the entire structure to collapse during the removal of the carbon support. A self-supported, interconnected 3D structure can be formed by merging and sintering of the initial separate nanoparticles during the calcination.

(iii) The uniformity and thickness of the metal oxide coating affects the T_{ox} of the MWCNTs. Thick layers of metal oxide with high quality increase the T_{ox} , which is due to the retardance of oxygen vacancy diffusion from the carbon–metal oxide interface to the exterior surface.

Chapter 7 INVESTIGATION OF A 3D NETWORK OF

PT NANOWIRES SYNTHESIZED BY ATOMIC LAYER DEPOSITION ON A CARBONACEOUS TEMPLATE

CONTENTS

CHAPTER 7 INVESTIGATION OF A 3D NETWORK OF PT NANOWIRES SYNTHESIZED BY ATOMIC LAYER DEPOSITION ON A CARBONACEOUS TEMPLATE.....	117
7.1 INTRODUCTION	117
7.2 EXPERIMENTAL DETAILS	118
7.3 RESULTS AND DISCUSSION.....	119
7.4 CONCLUSIONS.....	126

This chapter has been published as:

Shaoren Deng, Mert Kurttepli, Stella Deheryan, Daire J Cott, Philippe M Vereecken, Johan A Martens, Sara Bals, Gustaaf van Tendeloo, Christophe Detavernier, “Synthesis of a 3D network of Pt nanowires by atomic layer deposition on a carbonaceous template”, **2014**, *Nanoscale*, Volume 6, Issue 12, Pages 6939-6944.

Chapter 7 Investigation of a 3D network of Pt nanowires synthesized by atomic layer deposition on a carbonaceous template

The formation of a 3D network composed of free standing and interconnected Pt nanowires was investigated by advanced TEM. The novel material was achieved by a two-step method, consisting of conformal deposition of Pt by ALD on a forest of carbon nanotubes and subsequent removal of the carbonaceous template. The characterization showed that this pure 3D nanostructure of platinum is self-supported and offers a high surface area, which might be beneficial for various applications.

7.1 Introduction

As an effective catalyst, platinum (Pt) has been widely used in many applications including water splitting, fuel cells and automobile emission control^{203–205}. Different synthesis methods have been so far employed to synthesize Pt nanostructures with various morphologies. For instance, electrospinning was successfully carried out for the synthesis of Pt nanowires²⁰⁶. Yang et al. reported the production of Pt nanoparticles by reducing chloroplatinic acid (H_2PtCl_6) in formic acid at low temperature²⁰⁷. In the case of porous Pt structure synthesis, the use of a template material with a large surface area is widely preferred. Sun et al. used an aqueous method to grow ultra-small Pt nanowires on nitrogen-doped carbon nanotubes²⁰⁸. Sattayasamitsathit et al. demonstrated a delicate three-dimensional (3D) porous carbon structure decorated with Pt nanoparticles by electro-deposition²⁰⁹. 3D ordered networks of platinum nanowires were synthesized by S. Akbar et al. using a lipid with a high surface area as an electrochemical template²¹⁰. Dealloying a Pt–M (Al, Fe, Au.) alloy is another popular way to fabricate porous Pt nanowires and has therefore been under intensive research in recent years^{211–213}.

Different types of porous materials, e.g. Pt nanotubes or hybrid catalysts, have been successfully produced using ALD^{193,214,215}. Liu et al. for instance deposited Pt nanoparticles on carbon nanotube (CNT) supports for fuel cell applications²¹⁶. On the other hand, support-free and porous Pt nanostructures can be advantageous for certain applications, e.g., in aggressive environments where the supports are potentially not stable. As an example, Pt

nanoparticles dispersed on a carbon support may suffer from instability issues during oxygen reduction reactions^{217,218}.

Here, we report the structural characterization of Pt clusters on ordered MWCNTs and the formation of a 3D network comprising pure self-supporting Pt nanowires upon removal of the MWCNTs through annealing in air. The ALD Pt coated MWCNTs and the 3D network of Pt nanowires (i.e. after removal of the carbonaceous support) will be referred to as “Pt-MWCNTs” and “3D-Pt” throughout this chapter, respectively.

7.2 Experimental Details

Prior to MWCNTs growth, 70 nm TiN and 1 nm Co as catalysts were sputtered on an 8 inch Si wafer (Endura PVD tool, Applied Materials, USA). MWCNTs were synthesized at IMEC by Dr. D. Cott through catalyst-enhanced PECVD, as described previously. The ALD process of Pt onto MWCNTs was carried out at Ghent University (Dr. Shaoren Deng and Prof. Christophe Detavernier). The details of the ALD parameters can be found in Table 4. After ALD coating, *in situ* X-ray diffraction (adapted Bruker D8 system) was used to characterize the crystallization behavior during the calcination in air at 450°C. SEM accompanied by EDX was performed using a FEI Quanta 200 F to resolve the morphology of the samples before and after annealing. TEM specimens were prepared by crushing technique (see Section 2.2.1). BFTEM images and SAED patterns were acquired using a FEI Tecnai F20 TEM operating at 200 kV. HAADF-STEM images and EDX elemental maps were collected using a FEI Titan 60-300 TEM operating at 300 kV, equipped with a ChemiSTEM system for EDX analysis. HAADF-STEM electron tomography tilt series were collected using either an FEI Titan 60-300 TEM operating at 300 kV or an FEI Tecnai F20 TEM operating at 200 kV, both of which are equipped with an advanced tomography holder from Fischione Instruments and the FEI XPlore3D software package. For the tomography experiments, 71 HAADF-STEM images were acquired over the range of $\pm 70^\circ$ with 2° tilt increments. Alignment and reconstruction of the tomography data were carried out using the FEI Inspect3D software package. The reconstructions were performed using the “Simultaneous Iterative Reconstruction Technique” (SIRT) with 25 iterations implemented in Inspect 3D. Amira software (Visage Imaging GmbH) was used for visualization.

7.3 Results and discussion

A SEM image of the Pt-MWCNTs (Figure 57-(A)) shows that after 50 cycles of Pt coating, no obvious morphological changes were observed at the micrometer-scale after ALD. A TEM study of the samples (see Figure 57-(B) and (C)) revealed that Pt- ALD on the MWCNTs results in the formation of nanoparticles attached to the MWCNTs. The high resolution HAADF-STEM image given in Figure 57-(D) illustrates the crystallinity of the as-deposited Pt nanoparticles.

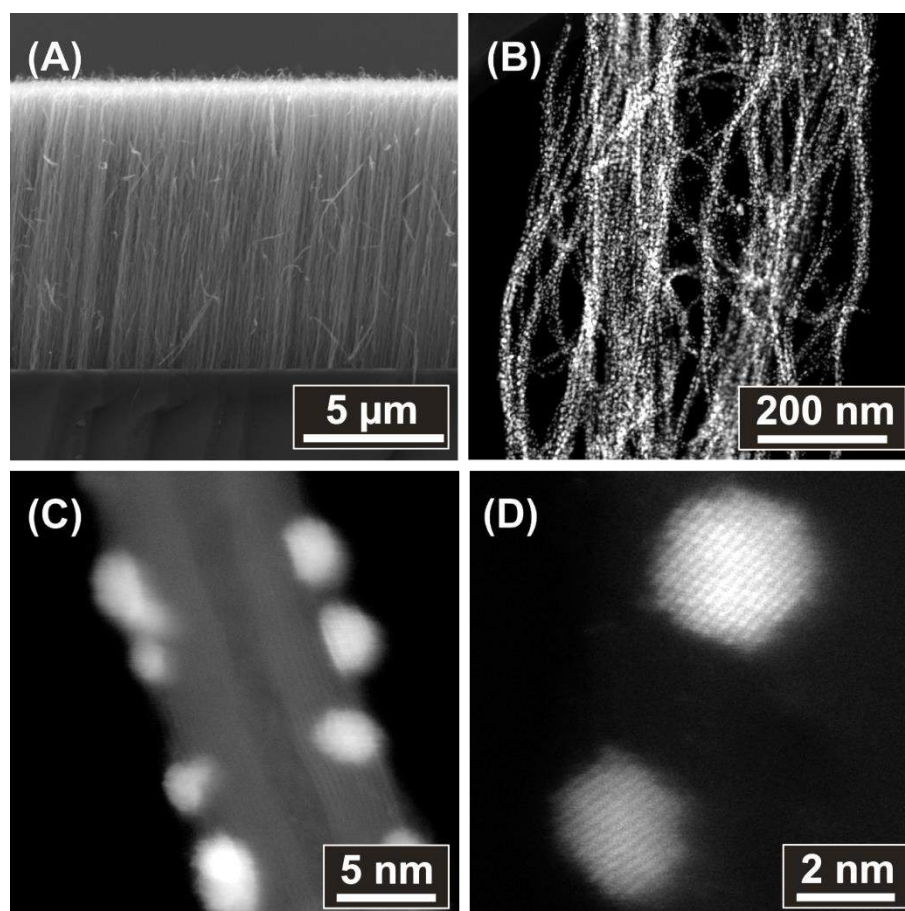


Figure 57 (A) SEM and (B) HAADF-STEM images of the as-deposited 50 cycle Pt-MWCNT samples. (C) and (D) high resolution HAADF-STEM images showing crystalline Pt nanoparticles coated on a single MWCNT.

In order to investigate the purity of the Pt nanoparticles, EDX elemental maps were collected from a region specified on the HAADF-STEM image, as shown in Figure 58-(A). The color-coded elemental map indicates the carbon and platinum content of the specified area and proves that the Pt nanoparticles are indeed attached to the MWCNTs (see Figure 58-(A-C)).

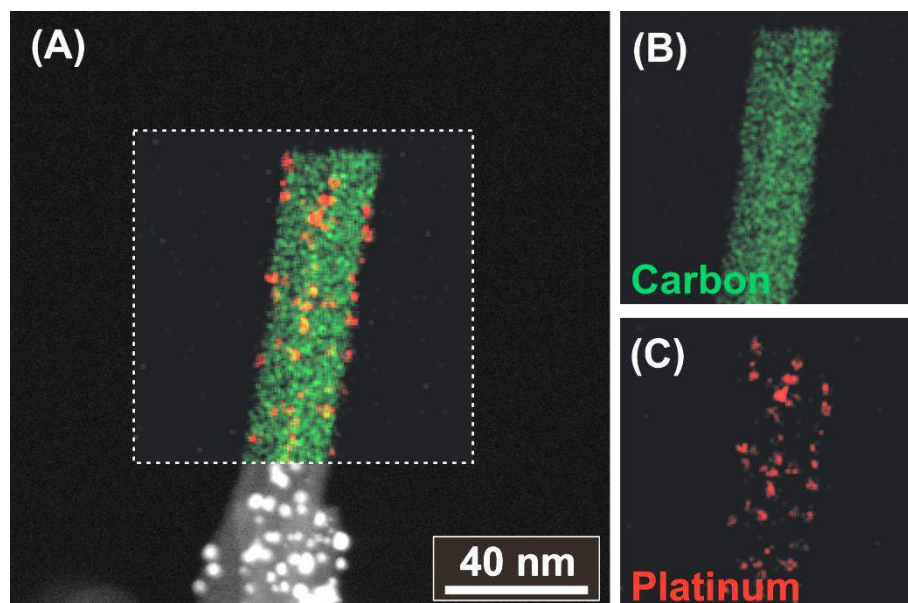


Figure 58 (A) A color-mixed elemental map of (B) carbon (green) and (C) platinum (red) overlaid with the (A) HAADF-STEM image.

In order to characterize the Pt-coated MWCNTs in 3D, an electron tomography experiment was performed. The visualization of the 3D reconstructed volume is presented in Figure 59-A). The formation of randomly distributed Pt nanoparticles on the MWCNTs is clearly observed in the 3D visualization. The size distribution of the Pt nanoparticles was obtained from the electron tomography experiment. It was found that the nanoparticles have an average particle radius around 3 nm, as shown in Figure 59-(B).

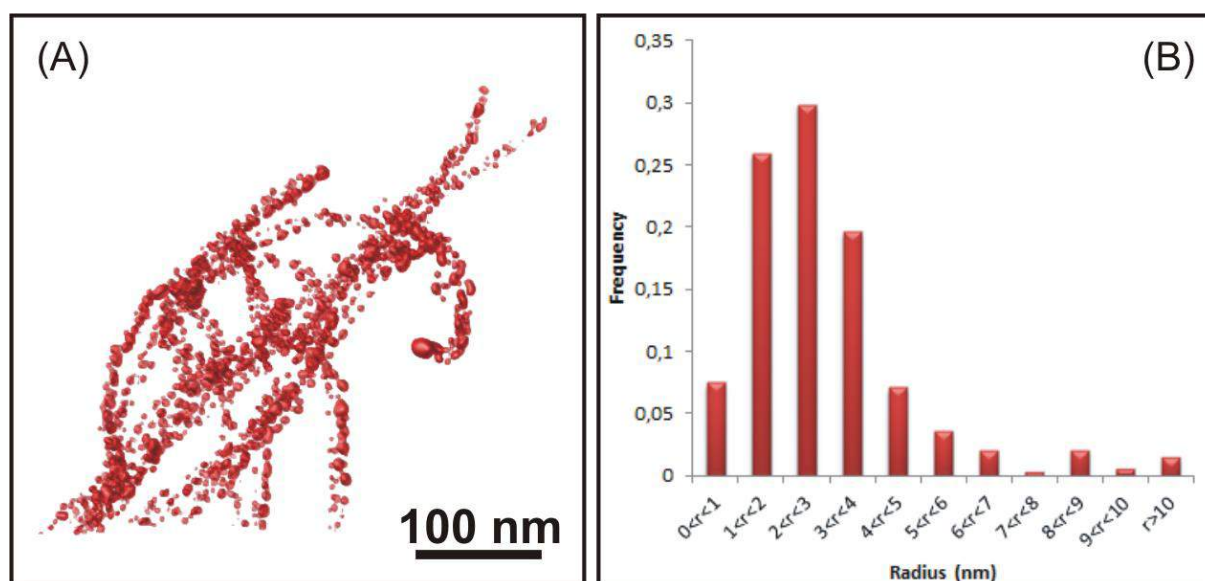


Figure 59 (A) The visualization of the 3D tomography and (B) the distribution of the Pt nanoparticle size from 50 cycle Pt-MWCNT samples (only Pt nanoparticles are shown).

In view of the wide spacing in between neighboring Pt nanoparticles on the MWCNTs, one could expect that removal of the carbonaceous support would induce complete collapse of the structure. Surprisingly, the overall forest-type morphology was preserved after calcination of the Pt-MWCNTs in air at 450°C. In Figure 60, SEM images and EDX results are used to schematically illustrate the transformation of Pt-MWCNTs into a free standing 3D-Pt nanostructure. Even though the MWCNTs were removed during the calcination in air, the overall structure was largely preserved; although a clear shrinkage of the height can be observed.

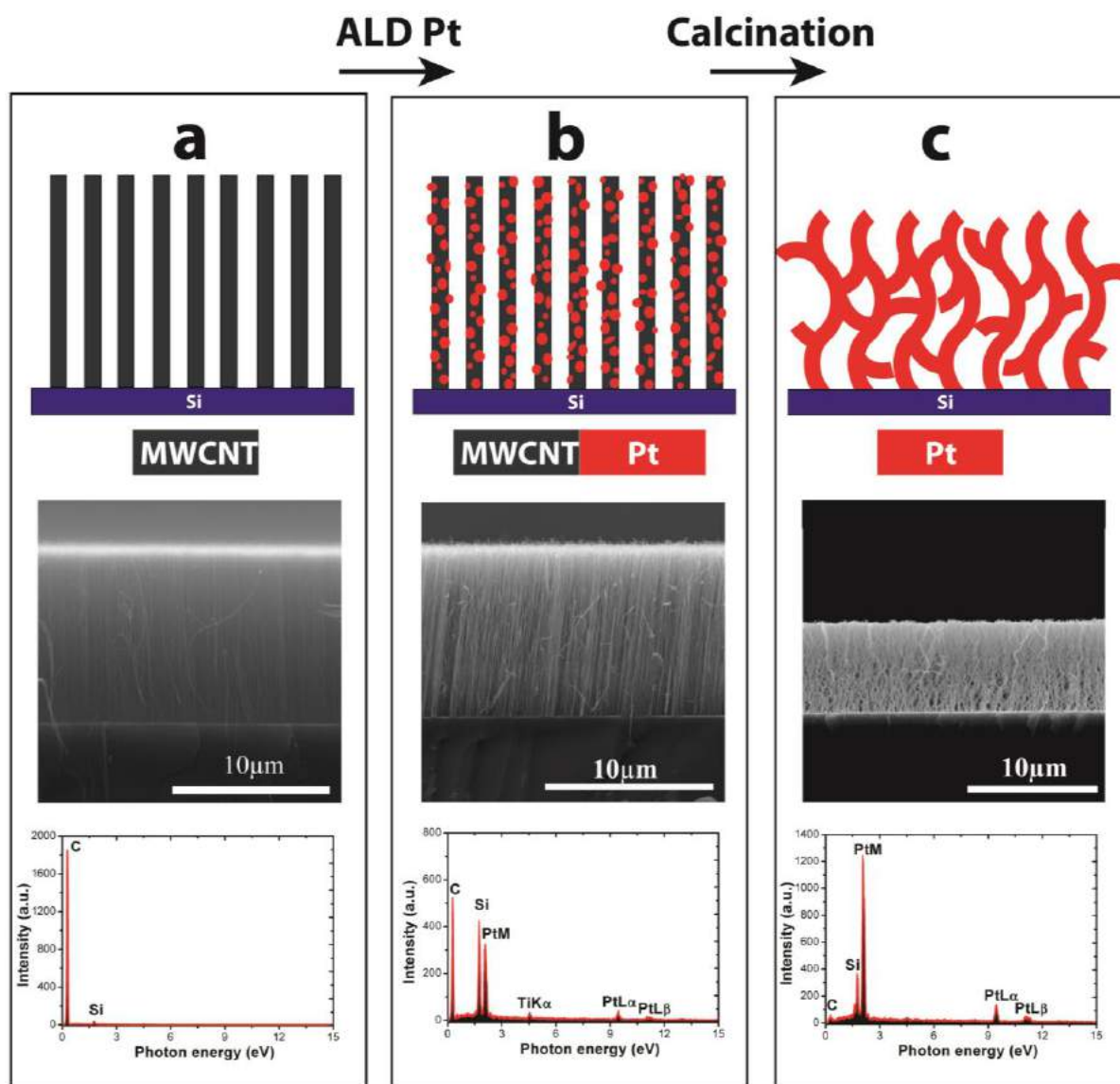


Figure 60 A combined figures of schematic illustration, SEM images and EDX results shows the morphology and elementary transformation from MWCNTs (a) to Pt-MWCNTs (b) and to 3D-Pt (c).

A detailed characterization of the resulting 3D-Pt sample was carried out by TEM (see Figure 61). Figure 61-(A) and (B) depict this 3D network comprising Pt nanowires with different diameters ranging from 10 to 50 nm. Such variation of the diameter is likely to result from the merging of Pt coating on adjacent MWCNTs into larger crystalline wires, whereas the Pt coating on isolated MWCNTs forms thinner nanowires. The high-resolution HAADF-STEM image shown in Figure 61-(C) reveals that these Pt nanowires are zigzag shaped and composed of crystalline nanoparticles. The SAED pattern (see Figure 61-(D)) shows no diffraction rings from the graphite phase but a clear appearance of diffraction rings from Pt, confirming the removal of the MWCNTs subsequent to annealing in air.

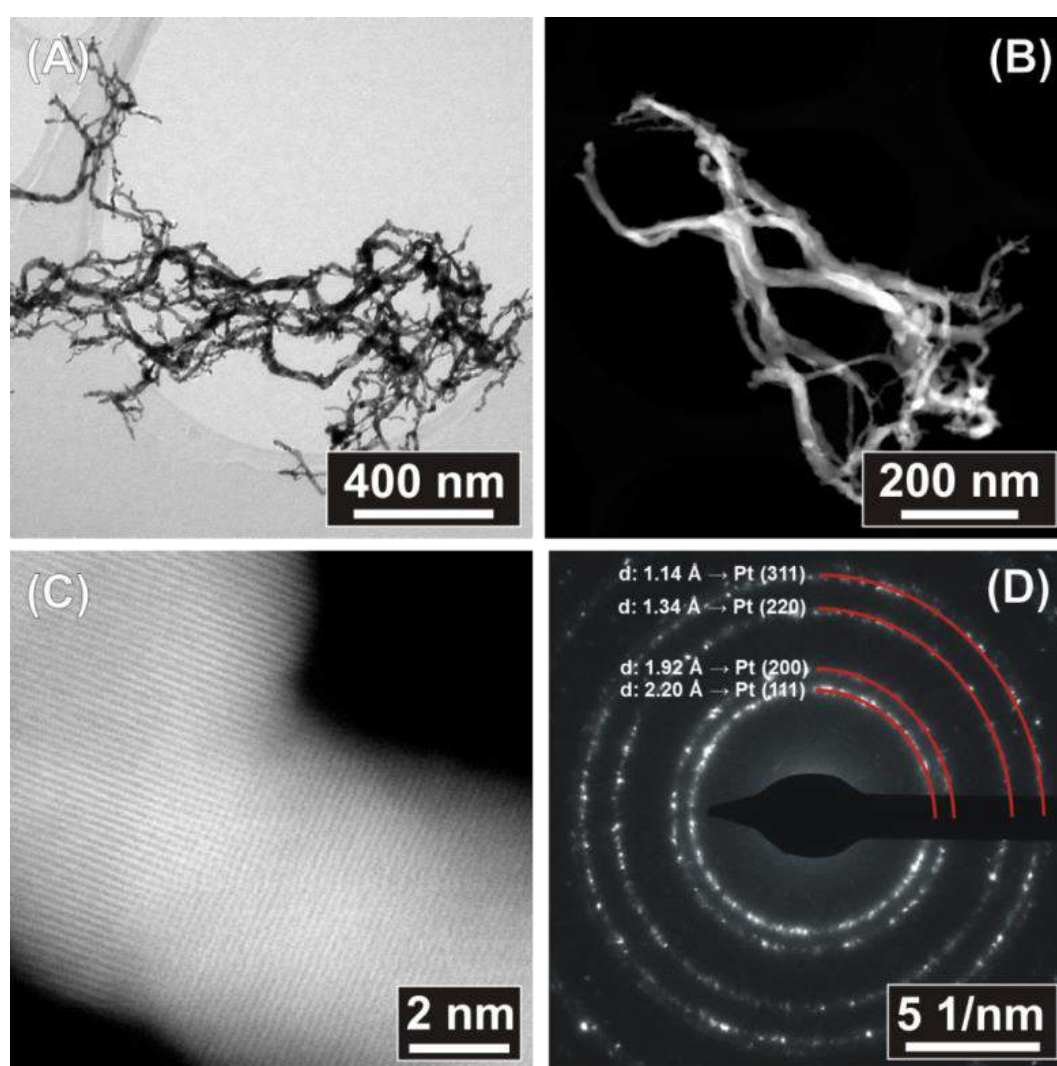


Figure 61 (A) BFTEM and (B) HAADF-STEM images of the 50 cycle 3D-Pt sample. (C) High resolution HAADF-STEM images of the 50 cycle 3D-Pt sample. (D) The SAED pattern of the part of the 50 cycle 3D-Pt sample given in (A).

The 3D nature of the network of Pt nanowires is revealed by HAADF-STEM electron tomography (see Figure 62-(A)). Unlike the as-deposited sample where Pt nanoparticles were observed to be attached to MWCNTs (see Figure 59), the annealed sample exhibits a 3D Pt network consisting of many interconnected Pt nanowires of different diameters. Necks throughout all the Pt nanowires were observed, which could be due to the migration and agglomeration of small Pt nanoparticles, and therefore resulted in thinner regions. From the HAADF-STEM electron tomography of the 50 cycle Pt-MWCNT samples, the orthoslices were collected from specified locations of the visualization (see Figure 62-(B-D)). These orthoslices also show that all the MWCNTs are removed completely, the tubular morphology was not formed, and instead solid Pt nanowires are formed.

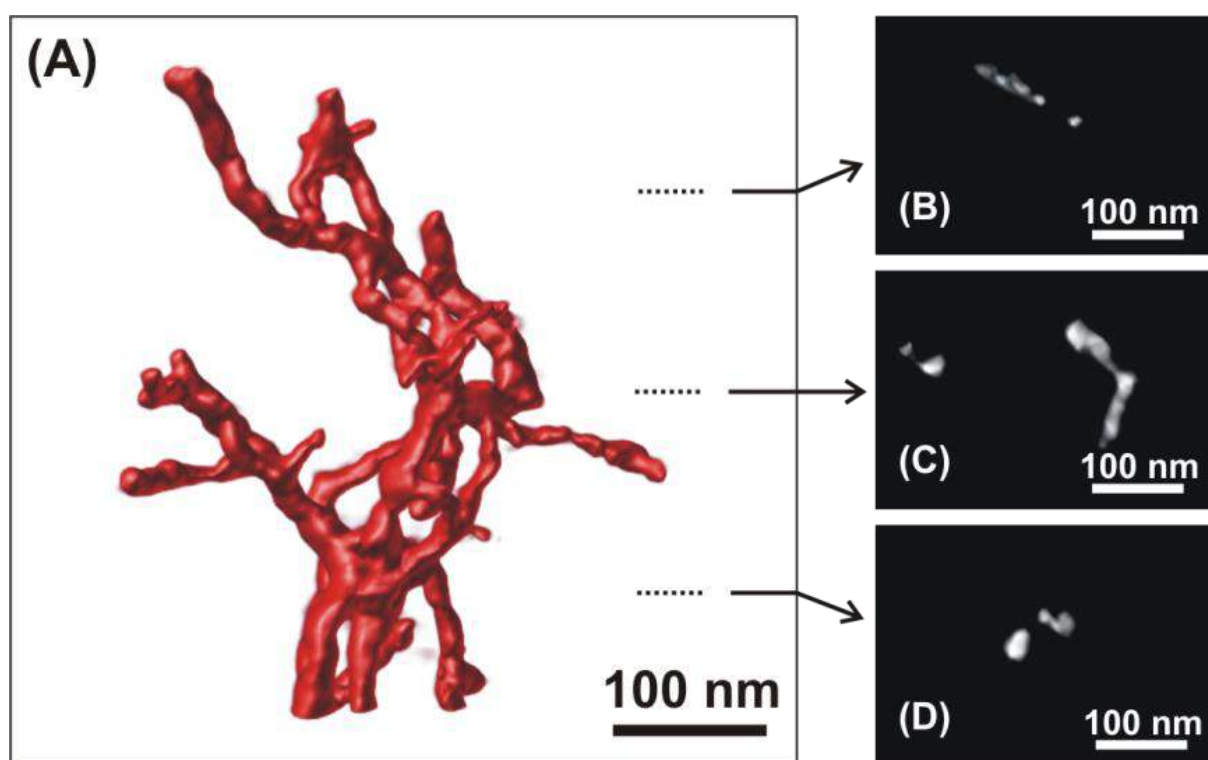


Figure 62 (A) The visualization of the 3D tomography of a section cut from the 50 cycle Pt sample. (B-D) Orthoslice images of 50 cycles 3D Pt sample from the reconstruction.

A detailed investigation of the carbon removal was carried out by EDX on several quenches of 50 cycle Pt-MWCNT samples and *in situ* XRD during the isothermal process, as shown in Figure 63-(A) and (B). For as-grown MWCNTs, the intensity of the carbon signal slightly decreases when the annealing temperature reaches 550°C and decreases significantly from 550 to 650°C, which indicates that the oxidation temperature is around 600°C for the

uncoated MWCNTs. For the 50 cycle Pt-MWCNTs, the carbon EDX signal exhibits similar evolution. However, the drastic descent of the carbon signal starts at a temperature between 350 and 400°C. This implies that the oxidation temperature of the MWCNTs has been significantly reduced due to the Pt nanoparticle coating on the MWCNTs. This might be attributed to the catalytic effect of the Pt nanoparticles, which seems to facilitate the oxidation process of the MWCNTs²¹⁹. Since the 50 cycle Pt-MWCNT sample has an uncoated MWCNT surface after the Pt ALD process, which includes an ozone exposure step, the effect of the exposure of MWCNTs to ozone pulses used during the ALD deposition process on the oxidation temperature has to be taken into consideration. Therefore, an ozone treated reference sample of MWCNTs was achieved by applying 50 half-cycles of ozone pulse on MWCNTs with the same pulse time and same temperature as applied during the Pt ALD process. As can be seen in Figure 63-(A), the variation of the carbon signal of the ozone treated reference sample overlaps with the uncoated MWCNTs, which excludes the possible effect of ozone treatment during the ALD process on the carbon removal.

In Figure 63-(B), the evolution of the grain size of Pt nanoparticles was calculated using the Scherrer equation and the FWHM of the Pt (111) diffraction peak during the calcination. The red points represent the evolution of the grain size during calcination in air at 450°C for 3 hours. The grain size starts to grow from 5 nm, which is in good agreement with the TEM characterization in Figure 59, and then gradually increases as the annealing temperature is raised at a fixed rate of 5°C min⁻¹. When the temperature is above 435°C, the grain size takes off and gradually increases during the isothermal plateau at 450°C and reaches a range of 24–27 nm at the end of the plateau. According to the EDX results in Figure 63-(A), the carbon intensity drops steeply between 400 and 450°C. Since this coincides with the dramatic increase of the Pt grain size, the removal of carbon appears to assist the merging of the Pt nanoparticles into larger grains. The limited increase of Pt grain size (blue points) of a control sample calcined at 450°C in He for 3 hours is in agreement with this interpretation. The grain size does not increase spectacularly when the sample was annealed at 400°C in air for 3 hours (green points), although this long anneal also resulted in complete removal of carbon according to EDX. This indicates that the calcination temperature is an important factor in the growth of the Pt grains.

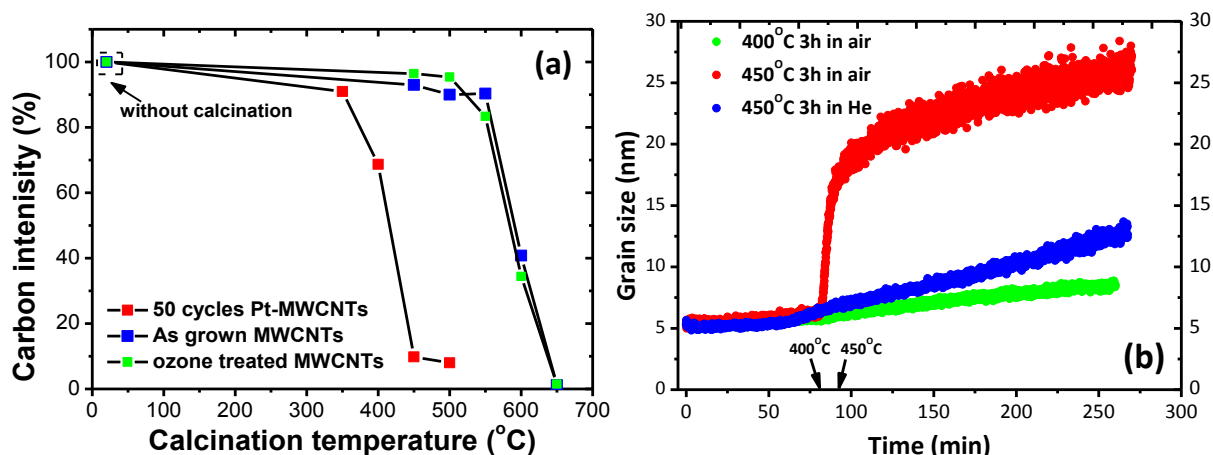


Figure 63 (a) Carbon content as determined by EDS on as grown MWCNTs, ozone treated MWCNTs and 50 cycles Pt-MWCNTs calcined at different temperatures. (b) is the grain size versus calcination time, calculated from *in situ* XRD measurement by using the Sherrer equation. The sample was ramped up from room temperature to 400 or 450°C at a constant rate of 5°C/min, and then kept at this temperature for a period of up to 3 hours.

To investigate the effect of the amount of Pt on the morphology after carbon removal, 100 and 200 cycle Pt-MWCNT samples were also annealed using the same process. SEM images of the annealed samples are shown in Figure 64-(A)–(C). For all the samples, a similar morphology was observed for the 3D-Pt structure. However, a considerable decrease in the overall layer thickness was observed. The thicknesses of 50, 100 and 200 cycle 3D-Pt samples were measured to be 5.82, 6.82 and 7.0 μm , respectively. The reduced shrinkage of the height for the sample with more ALD Pt cycles indicates that the presence of a larger amount of as-deposited Pt coating reduces the shrinkage during calcination.

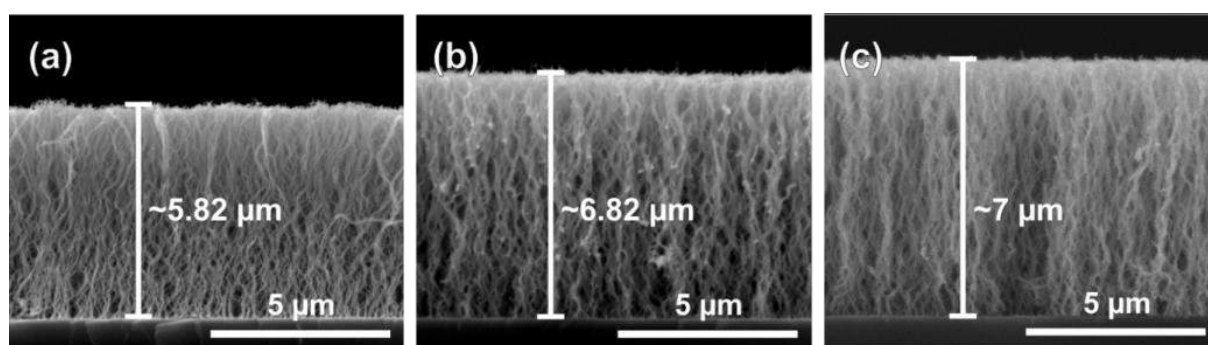


Figure 64 SEM pictures of 50 cycles (a), 100 cycles (b) and 200 cycles (c) Pt-MWCNT samples after calcination at 450°C in air for 3 hours.

7.4 Conclusions

In summary, using 2D and 3D TEM, we demonstrated the formation of a novel porous 3D network comprised of free standing Pt nanowires. It was clearly shown that Pt nanowires formed an interconnected architecture which consists of pure Pt without any carbon support. The porous, conductive and interconnected features of this 3D network of Pt nanowires could be ideal for multiple applications requiring support-free Pt catalysts, e.g. for use in corrosive environments.

Chapter 8 CONCLUSIONS AND FUTURE RESEARCH

Chapter 8 Conclusions and future research

In this thesis, we demonstrated how advanced electron microscopy can be used to study materials that consist of soft and hard matter. For the soft matter part, it was shown that the extraordinary physical properties of CNTs and CNSs, such as high surface area and aspect ratio, make them well-suited as templates to deposit different metals/metal oxides. In case of the hard compound, it was demonstrated that the structural properties of oxide templates and their interactions with the soft matter components have great influence on the final characteristics of the materials comprising carbonaceous species. These two approaches are summarized at a schematic illustration presented in Figure 65.

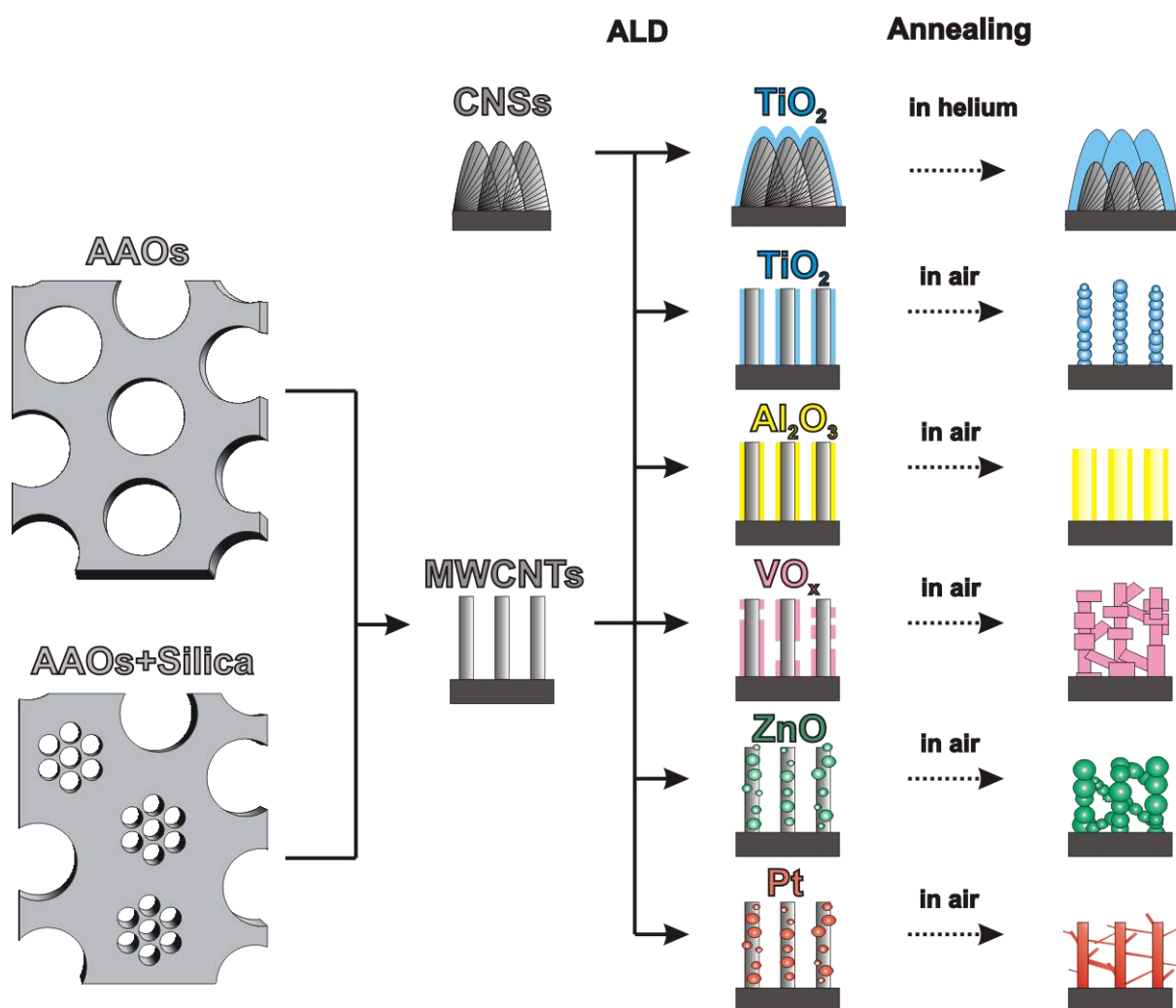


Figure 65 Schematic demonstration of the templated synthesis of MWCNTs and the formation of porous metal oxide nanostructures by ALD on MWCNTs and CNSs followed by calcination.

In Part 1, TEM was used to show that the AAO membrane templated synthesis approach can be adopted when CNTs are fabricated through CCVD. From the analysis, it was concluded that the method can yield long CNT bundles that are sticking out from the pores of AAO membrane with the alignment parallel to the gas flow direction at CVD. In addition, the characterization of the Fe₂Ni catalyst impregnated AAO membranes demonstrated that a short NaOH etching step can enhance the adhesion of the particles and prevent the blockage of the AAO pores by the catalyst solution. Moreover, our results showed how TEM can be used to determine the structure and morphology of complex material systems, such as mesoporous silica confined in the pores of AAO membrane as in our case, both qualitatively and quantitatively. In this respect, the optimization of the mesopores of silica can be assisted.

In Part 2, it was concluded that CNSs can be used as templates to deposit TiO₂ layers through ALD, and that in this case both the anatase content of the TiO₂ layer and the preservation of CNSs upon annealing in helium environment can be revealed by TEM. For the investigation of porous nanostructured metals/metal oxides synthesized through ALD on forests of MWCNTs, which include Al₂O₃, TiO₂, V₂O₅, ZnO and Pt, it was demonstrated that the calcination in air environment leads to different resulting morphologies depending on the type of the deposited metal/metal oxide layer.

Future research work is worth considering as follows:

- Although FIB sample preparation has succeeded in preserving aCNTb's and the catalysts in AAO pores for TEM analysis, the TEM investigation of the FIB lamella could yield information mostly from a small section of the AAO-CNTs due to the FIB being site specific. In addition, in case the length of the aCNTb's would reach to several tens of micrometers with future improvements at the synthesis part, preparing FIB lamellas from such aCNTb's confined in the pores of AAO membranes could be challenging. Therefore, cross-section TEM sample preparation can be applied to AAO-CNTs materials in the future analysis, which could make their characterization possible at a larger scale.
- If the growth of CNTs inside the columns of mesoporous silica synthesized in AAO membrane pores would be succeeded in the future, this shall require an in-depth TEM analysis preferentially in 3D. However, in such case, conventional HAADF-STEM

tomography would possibly not yield all the necessary information, especially in terms of their chemical analysis. This is due to the fact that the resulting materials would be consisting of elements which have low atomic numbers and are neighboring to each other in the periodic table, such as Al, Si, O and C. EDX-STEM tomography will be of great importance for such samples, which was already shown here in case of AAO-aCNTb's.

- Since carbon-based materials are susceptible to electron beam damage, the structural changes which occur due to knock-on damage can be a severe problem during STEM and TEM observations. Here, we could overcome this limitation by using accelerating voltages (120 kV) mildly above the threshold for the knock on damage (~80 kV). In this manner, the morphology of these templates was mostly preserved while maintaining a resolution less than one angstrom. However, this technique was mostly limited to resolving the structure of the metal/metal oxide coatings, whereas the structural information attained from the carbon based counterparts was restricted due to the decreased but yet mildly present knock-on damage. In future, the use of low voltage aberration correction in STEM and TEM imaging will become increasingly important to understand the interaction between carbon based templates and their coatings. For instance, the technique could be applied to directly observe the interface between as-deposited ALD processed layers and the template nanostructures at accelerating voltages below the threshold value for the knock-on damage. In this manner, preferential deposition or formation of nanoparticles at defective sites of carbonaceous templates can be studied without any potential morphological changes which occur at the carbonaceous materials as a result of the knock-on process.
- In addition, another solution to reduce beam damage could be the use of new generation CCD cameras, which are designed to optimize image detection for beam-sensitive specimens requiring extreme low dose conditions. Since the efficient detection of low-contrast signals is critical, especially in cases of imaging carbonaceous materials, or electron tomography, in which the tomogram resolution increases with the number of images recorded, these new detectors offer an improved signal-to-noise ratio. In the future, the characterizations of the samples we studied here could be conducted by the use of such image detectors, through which the beam

damage could be further reduced by the decrease at the total acquisition times of the images recorded.

Bibliography

Bibliography

- (1) Heimann, R. B.; Esvukov, S. E.; Koga, Y. Carbon Allotropes: A Suggested Classification Scheme Based on Valence Orbital Hybridization. *Carbon*, 1997, 35, 1654–1658.
- (2) Robertson, J. Diamond-like Amorphous Carbon. *Materials Science and Engineering: R: Reports*, 2002, 37, 129–281.
- (3) Novoselov, K. S.; Geim, a K.; Morozov, S. V; Jiang, D.; Zhang, Y.; Dubonos, S. V; Grigorieva, I. V; Firsov, a a. Electric Field Effect in Atomically Thin Carbon Films. *Science* **2004**, 306, 666–669.
- (4) Tjong, S. C. Recent Progress in the Development and Properties of Novel Metal Matrix Nanocomposites Reinforced with Carbon Nanotubes and Graphene Nanosheets. *Materials Science and Engineering R: Reports*, 2013, 74, 281–350.
- (5) Rooth, M.; Quinlan, R. a.; Widenkvist, E.; Lu, J.; Grennberg, H.; Holloway, B. C.; Hårsta, A.; Jansson, U. Atomic Layer Deposition of Titanium Dioxide Nanostructures Using Carbon Nanosheets as a Template. *J. Cryst. Growth* **2009**, 311, 373–377.
- (6) Zhu, M.; Wang, J.; Holloway, B. C.; Outlaw, R. a.; Zhao, X.; Hou, K.; Shutthanandan, V.; Manos, D. M. A Mechanism for Carbon Nanosheet Formation. *Carbon N. Y.* **2007**, 45, 2229–2234.
- (7) Georgakilas, V. Chemical Functionalization of Ultrathin Carbon Nanosheets. *Fullerenes, Nanotubes and Carbon Nanostructures*, 2010, 18, 87–95.
- (8) Cott, D. J.; Verheijen, M.; Richard, O.; Radu, I.; Gendt, S. De; Elshocht, S. Van; Vereecken, P. M. Synthesis of Large Area Carbon Nanosheets for Energy Storage Applications. *Carbon N. Y.* **2013**, 58, 59–65.
- (9) Ando, Y.; Zhao, X.; Ohkohchi, M. Production of Petal-like Graphite Sheets by Hydrogen Arc Discharge. *Carbon*, 1997, 35, 153–158.

- (10) Shih, W. C.; Jeng, J. M.; Huang, C. T.; Lo, J. T. Fabrication of Carbon Nanoflakes by RF Sputtering for Field Emission Applications. In *Vacuum*; Elsevier Ltd, 2010; Vol. 84, pp. 1452–1456.
- (11) Wang, J. J.; Zhu, M. Y.; Outlaw, R. a.; Zhao, X.; Manos, D. M.; Holloway, B. C.; Mammana, V. P. Free-Standing Subnanometer Graphite Sheets. *Appl. Phys. Lett.* **2004**, 85, 1265–1267.
- (12) Shang, N. G.; Papakonstantinou, P.; McMullan, M.; Chu, M.; Stamboulis, A.; Potenza, A.; Dhesi, S. S.; Marchetto, H. Catalyst-Free Efficient Growth, Orientation and Biosensing Properties of Multilayer Graphene Nanoflake Films with Sharp Edge Planes. *Adv. Funct. Mater.* **2008**, 18, 3506–3514.
- (13) Wu, Y.; Qiao, P.; Chong, T.; Shen, Z. Carbon Nanowalls Grown by Microwave Plasma Enhanced Chemical Vapor Deposition. *Adv. Mater.* **2002**, 14, 64–67.
- (14) Shen, J. M.; Feng, Y. T. Formation of Flower-like Carbon Nanosheet Aggregations and Their Electrochemical Application. *J. Phys. Chem. C* **2008**, 112, 13114–13120.
- (15) Wang, Z. P.; Shoji, M.; Ogata, H. Growth and Electrochemical Properties of Carbon Nanosheets via Microwave Plasma Enhanced Chemical Vapor Deposition. *Fullerenes, Nanotubes and Carbon Nanostructures*, 2012, 20, 473–481.
- (16) Ban, C.; Xie, M.; Sun, X.; Travis, J. J.; Wang, G.; Sun, H.; Dillon, A. C.; Lian, J.; George, S. M. Atomic Layer Deposition of Amorphous TiO₂ on Graphene as an Anode for Li-Ion Batteries. *Nanotechnology* **2013**, 24, 424002.
- (17) Yoo, E.; Okata, T.; Akita, T.; Kohyama, M.; Nakamura, J.; Honma, I. Enhanced Electrocatalytic Activity of Pt Subnanoclusters on Graphene Nanosheet Surface. *Nano Lett.* **2009**, 9, 2255–2259.
- (18) Guo, P.; Song, H.; Chen, X. Electrochemical Performance of Graphene Nanosheets as Anode Material for Lithium-Ion Batteries. *Electrochem. commun.* **2009**, 11, 1320–1324.

- (19) Zhao, X.; Tian, H.; Zhu, M.; Tian, K.; Wang, J. J.; Kang, F.; Outlaw, R. a. Carbon Nanosheets as the Electrode Material in Supercapacitors. *J. Power Sources* **2009**, *194*, 1208–1212.
- (20) Moitzheim, S.; Nimisha, C. S.; Deng, S.; Cott, D. J.; Detavernier, C.; Vereecken, P. M. Nanostructured TiO₂/carbon Nanosheet Hybrid Electrode for High-Rate Thin-Film Lithium-Ion Batteries. *Nanotechnology* **2014**, *25*, 504008.
- (21) Liu, J.; Meng, X.; Hu, Y.; Geng, D.; Banis, M. N.; Cai, M.; Li, R.; Sun, X. Controlled Synthesis of Zirconium Oxide on Graphene Nanosheets by Atomic Layer Deposition and Its Growth Mechanism. *Carbon N. Y.* **2013**, *52*, 74–82.
- (22) Iijima, S. Helical Microtubules of Graphitic Carbon. *Nature*, 1991, *354*, 56–58.
- (23) De Volder, M. F. L.; Tawfick, S. H.; Baughman, R. H.; Hart, a J. Carbon Nanotubes: Present and Future Commercial Applications - SOM. *Science (80-.)*. **2013**, *339*, 535–539.
- (24) Peng, B.; Locascio, M.; Zapol, P.; Li, S.; Mielke, S. L.; Schatz, G. C.; Espinosa, H. D. Measurements of near-Ultimate Strength for Multiwalled Carbon Nanotubes and Irradiation-Induced Crosslinking Improvements. *Nat. Nanotechnol.* **2008**, *3*, 626–631.
- (25) Pop, E.; Mann, D.; Wang, Q.; Goodson, K.; Dai, H. Thermal Conductance of an Individual Single-Wall Carbon Nanotube above Room Temperature. *Nano Lett.* **2006**, *6*, 96–100.
- (26) Graebner, J. E.; Jin, S.; Kammlott, G. W.; Herb, J. a.; Gardinier, C. F. Unusually High Thermal Conductivity in Diamond Films. *Appl. Phys. Lett.* **1992**, *60*, 1576–1578.
- (27) Wei, B. Q.; Vajtai, R.; Ajayan, P. M. Reliability and Current Carrying Capacity of Carbon Nanotubes. *Appl. Phys. Lett.* **2001**, *79*, 1172–1174.

- (28) Li, X. L.; Li, C.; Zhang, Y.; Chu, D. P.; Milne, W. I.; Fan, H. J. Atomic Layer Deposition of ZnO on Multi-Walled Carbon Nanotubes and Its Use for Synthesis of CNT–ZnO Heterostructures. *Nanoscale Res. Lett.* **2010**, *5*, 1836–1840.
- (29) Awasthi, K.; Srivastava, A.; Srivastava, O. N. Synthesis of Carbon Nanotubes. *J. Nanosci. Nanotechnol.* **2005**, *5*, 1616–1636.
- (30) Ebbesen, T. W.; Ajayan, P. M. Large-Scale Synthesis of Carbon Nanotubes. *Nature*, 1992, *358*, 220–222.
- (31) Ando, Y.; Iijima, S. Preparation of Carbon Nanotubes by Arc-Discharge Evaporation. *Japanese J. Appl. Physics, Part 2 Lett.* **1993**, *32*.
- (32) Zhang, Y.; Gu, H.; Iijima, S. Single-Wall Carbon Nanotubes Synthesized by Laser Ablation in a Nitrogen Atmosphere. *Appl. Phys. Lett.* **1998**, *73*, 3827–3829.
- (33) Puretzky, a. a.; Geohegan, D. B.; Fan, X.; Pennycook, S. J. Dynamics of Single-Wall Carbon Nanotube Synthesis by Laser Vaporization. *Appl. Phys. A Mater. Sci. Process.* **2000**, *70*, 153–160.
- (34) Varshney, D.; Weiner, B. R.; Morell, G. Growth and Field Emission Study of a Monolithic Carbon Nanotube/diamond Composite. *Carbon N. Y.* **2010**, *48*, 3353–3358.
- (35) Tempel, H.; Joshi, R.; Schneider, J. J. Ink Jet Printing of Ferritin as Method for Selective Catalyst Patterning and Growth of Multiwalled Carbon Nanotubes. *Mater. Chem. Phys.* **2010**, *121*, 178–183.
- (36) Smajda, R.; Andresen, J. C.; Duchamp, M.; Meunier, R.; Casimirius, S.; Hernádi, K.; Forró, L.; Magrez, A. Synthesis and Mechanical Properties of Carbon Nanotubes Produced by the Water Assisted CVD Process. *Phys. Status Solidi* **2009**, *246*, 2457–2460.

- (37) Patole, S. P.; Alegaonkar, P. S.; Lee, H.-C.; Yoo, J.-B. Optimization of Water Assisted Chemical Vapor Deposition Parameters for Super Growth of Carbon Nanotubes. *Carbon*, 2008, *46*, 1987–1993.
- (38) Byon, H. R.; Lim, H.; Song, H. J.; Choi, H. C. A Synthesis of High Purity Single-Walled Carbon Nanotubes from Small Diameters of Cobalt Nanoparticles by Using Oxygen-Assisted Chemical Vapor Deposition Process. **2007**, *28*, 2056–2060.
- (39) Xu, Y.; Dervishi, E.; Biris, A. R.; Biris, A. S. Chirality-Enriched Semiconducting Carbon Nanotubes Synthesized on High Surface Area MgO-Supported Catalyst. *Mater. Lett.* **2011**, *65*, 1878–1881.
- (40) Steiner, S. a.; Baumann, T. F.; Bayer, B. C.; Blume, R.; Worsley, M. a.; MoberlyChan, W. J.; Shaw, E. L.; Schlögl, R.; Hart, a. J.; Hofmann, S.; et al. Nanoscale Zirconia as a Nonmetallic Catalyst for Graphitization of Carbon and Growth of Single- and Multiwall Carbon Nanotubes. *J. Am. Chem. Soc.* **2009**, *131*, 12144–12154.
- (41) Chhowalla, M.; Teo, K. B. K.; Ducati, C.; Rupesinghe, N. L.; Amaratunga, G. a J.; Ferrari, a. C.; Roy, D.; Robertson, J.; Milne, W. I. Growth Process Conditions of Vertically Aligned Carbon Nanotubes Using Plasma Enhanced Chemical Vapor Deposition. *J. Appl. Phys.* **2001**, *90*, 5308–5317.
- (42) Li, Y.; Mann, D.; Rolandi, M.; Kim, W.; Ural, A.; Hung, S.; Javey, A.; Cao, J.; Wang, D.; Yenilmez, E.; et al. Preferential Growth of Semiconducting Single-Walled Carbon Nanotubes by a Plasma Enhanced CVD Method. *Nano Lett.* **2004**, *4*, 317–321.
- (43) Kumar, M.; Ando, Y. Chemical Vapor Deposition of Carbon Nanotubes: A Review on Growth Mechanism and Mass Production. *J. Nanosci. Nanotechnol.* **2010**, *10*, 3739–3758.
- (44) Fan, S. Self-Oriented Regular Arrays of Carbon Nanotubes and Their Field Emission Properties. *Science (80-.)*. **1999**, *283*, 512–514.

- (45) Altalhi, T.; Ginic-Markovic, M.; Han, N.; Clarke, S.; Losic, D. Synthesis of Carbon Nanotube (CNT) Composite Membranes. *Membranes (Basel)*. **2010**, *1*, 37–47.
- (46) Szabó, A.; Perri, C.; Csató, A.; Giordano, G.; Vuono, D.; Nagy, J. B. Synthesis Methods of Carbon Nanotubes and Related Materials. *Materials (Basel)*. **2010**, *3*, 3092–3140.
- (47) Kumar, M.; Ando, Y. Chemical Vapor Deposition of Carbon Nanotubes: A Review on Growth Mechanism and Mass Production. *J. Nanosci. Nanotechnol.* **2010**, *10*, 3739–3758.
- (48) Rashid, H. U.; Yu, K.; Umar, M. N.; Anjum, M. N.; Khan, K.; Ahmad, N.; Jan, M. T. CATALYST ROLE IN CHEMICAL VAPOR DEPOSITION (CVD) PROCESS: A REVIEW. *Rev. Adv. Mater. Sci* **2015**, *40*, 235–248.
- (49) Ganesh, E. Single Walled and Multi Walled Carbon Nanotube Structure, Synthesis and Applications. *Ijitee.Org* **2013**, 311–320.
- (50) Prasek, J.; Drbohlavova, J.; Chomoucka, J.; Hubalek, J.; Jasek, O.; Adam, V.; Kizek, R. Methods for Carbon Nanotubes Synthesis—review. *Journal of Materials Chemistry*, 2011, *21*, 15872.
- (51) Bianco, A.; Kostarelos, K.; Prato, M. Applications of Carbon Nanotubes in Drug Delivery. *Current Opinion in Chemical Biology*, 2005, *9*, 674–679.
- (52) Terrones, M. : Synthesis, Properties, and Applications of Carbon Nanotubes. *Annual Review of Materials Research*, 2003, *33*, 419–501.
- (53) Martel, R.; Schmidt, T.; Shea, H. R.; Hertel, T.; Avouris, P. Single- and Multi-Wall Carbon Nanotube Field-Effect Transistors. *Appl. Phys. Lett.* **1998**, *73*, 2447–2449.
- (54) Dillon, a. C.; Jones, K. M.; Bekkedahl, T. a.; Kiang, C. H.; Bethune, D. S.; Heben, M. J. Storage of Hydrogen in Single-Walled Carbon Nanotubes. *Nature*, 1997, *386*, 377–379.

- (55) Wirth, C. T.; Bayer, B. C.; Gamalski, A. D.; Esconjauregui, S.; Weatherup, R. S.; Ducati, C.; Baehetz, C.; Robertson, J.; Hofmann, S. The Phase of Iron Catalyst Nanoparticles during Carbon Nanotube Growth. *Chem. Mater.* **2012**, *24*, 4633–4640.
- (56) Landois, P.; Pinault, M.; Rouzière, S.; Porterat, D.; Mocuta, C.; Elkaim, E.; Mayne-L’Hermite, M.; Launois, P. In Situ Time Resolved Wide Angle X-Ray Diffraction Study of Nanotube Carpet Growth: Nature of Catalyst Particles and Progressive Nanotube Alignment. *Carbon N. Y.* **2015**, *87*, 246–256.
- (57) Nishimura, K.; Okazaki, N.; Pan, L.; Nakayama, Y. In Situ Study of Iron Catalysts for Carbon Nanotube Growth Using X-Ray Diffraction Analysis. *Jpn. J. Appl. Phys.* **2004**, *43*, L471–L474.
- (58) Safarova, K.; Drovak, a; Kubinek, R. Usage of AFM, SEM and TEM for the Research of Carbon Nanotubes. *Mod. Res. Educ. Top. Microsc.* **2007**, 513–519.
- (59) Hou, P.; Liu, C.; Shi, C.; Cheng, H. Carbon Nanotubes Prepared by Anodic Aluminum Oxide Template Method. *Chinese Sci. Bull.* **2012**, *57*, 187–204.
- (60) Willinger, M.-G.; Neri, G.; Bonavita, A.; Micali, G.; Rauwel, E.; Hertrich, T.; Pinna, N. The Controlled Deposition of Metal Oxides onto Carbon Nanotubes by Atomic Layer Deposition: Examples and a Case Study on the Application of V2O4 Coated Nanotubes in Gas Sensing. *Phys. Chem. Chem. Phys.* **2009**, *11*, 3615–3622.
- (61) Xiao, K.; Gregoire, J. M.; McCluskey, P. J.; Dale, D.; Vlassak, J. J. Scanning AC Nanocalorimetry Combined with in-Situ X-Ray Diffraction. *J. Appl. Phys.* **2013**, *113*, 243501.
- (62) Urban, K. W. Is Science Prepared for Atomic-Resolution Electron Microscopy? *Nat Mater* **2009**, *8*, 260–262.
- (63) Muller, D. A. Structure and Bonding at the Atomic Scale by Scanning Transmission Electron Microscopy. *Nat Mater* **2009**, *8*, 263–270.

- (64) Li, Y.-L.; Kinloch, I. a; Windle, A. H. Direct Spinning of Carbon Nanotube Fibers from Chemical Vapor Deposition Synthesis. *Science* **2004**, *304*, 276–278.
- (65) Zhang, M.; Atkinson, K. R.; Baughman, R. H. Multifunctional Carbon Nanotube Yarns by Downsizing an Ancient Technology. *Science* **2004**, *306*, 1358–1361.
- (66) Deng, S.; Verbruggen, S. W.; He, Z.; Cott, D. J.; Vereecken, P. M.; Martens, J. a.; Bals, S.; Lenaerts, S.; Detavernier, C. Atomic Layer Deposition-Based Synthesis of Photoactive TiO₂ Nanoparticle Chains by Using Carbon Nanotubes as Sacrificial Templates. *RSC Adv.* **2014**, *4*, 11648.
- (67) Zhou, W.; Apkarian, R.; Wang, Z. L.; Joy, D. Fundamentals of Scanning Electron Microscopy (SEM). In *Scanning Microscopy for Nanotechnology*; Springer New York: New York, NY, 2006; pp. 1–40.
- (68) Genç, a; University, T. O. S.; Inc, E. a F. I.; University, T. O. S. Post-FIB TEM Sample Preparation Using A Low Energy Argon Beam. *Microscopy and Microanalysis*, 2007, *13*, 1520–1521.
- (69) Rao, D. V. S.; Muraleedharan, K.; Humphreys, C. J. TEM Specimen Preparation Techniques. **2010**, 1232–1244.
- (70) Kirmse, H.; Oehlschlegel, E.; Polzer, F.; Blumstengel, S.; Sparenberg, M.; Henneberger, F. Cross-Sectional TEM Preparation of Hybrid Inorganic/organic Materials Systems by Ultramicrotomy. *J. Phys. Conf. Ser.* **2013**, *471*, 012034.
- (71) Dürr, A. C.; Schreiber, F.; Kelsch, M.; Dosch, H. Optimized Preparation of Cross-Sectional TEM Specimens of Organic Thin Films. *Ultramicroscopy* **2003**, *98*, 51–55.
- (72) Ma, H.; Shieh, K.; Qiao, T. X. Study of Transmission Electron Microscopy (TEM) and Scanning Electron Microscopy (SEM). **2006**, *4*, 14–22.
- (73) Williams, D.; Carter, C. B. High-Resolution TEM. In *Transmission Electron Microscopy SE* - 28; Springer US, 2009; pp. 483–509.

- (74) De Graef, M. *Introduction to Conventional Transmission Electron Microscopy*; Cambridge University Press, 2003.
- (75) Abe, E. Atomic-Scale Characterization of Nanostructured Metallic Materials by HAADF/Z-Contrast STEM. *Mater. Trans.* **2003**, *44*, 2035–2041.
- (76) Genc, A.; Kovarik, L.; Gu, M.; Cheng, H.; Plachinda, P.; Pullan, L.; Freitag, B.; Wang, C. XEDS STEM Tomography for 3D Chemical Characterization of Nanoscale Particles. *Ultramicroscopy* **2013**, *131*, 24–32.
- (77) Lin, M.; Tan, H. R.; Tan, J. P. Y.; Boothroyd, C.; Foo, Y. L.; He, C. Bin. Transmission Electron Microscope Tomography of Nanostructured Materials. *J. Nanoeng. Nanomanufacturing* **2011**, *1*, 257–264.
- (78) Genç, A.; Cheng, H.; Winterstein, J.; Pullan, L.; Freitag, B.; Fraser, H. L. 3D Chemical Mapping Using Tomography with an Enhanced XEDS System MAPPING TECHNOLOGY. **2012**, 23–25.
- (79) Verbeeck, J.; Van Dyck, D.; Van Tendeloo, G. Energy-Filtered Transmission Electron Microscopy: An Overview. *Spectrochim. Acta Part B At. Spectrosc.* **2004**, *59*, 1529–1534.
- (80) Palisaitis, J. *Electron Energy Loss Spectroscopy of III-Nitride Semiconductors [Elektronisk Resurs]*; Link{ö}ping University Electronic Press: Link{ö}ping, 2011.
- (81) Krivanek, O. L.; Ursin, J. P.; Bacon, N. J.; Corbin, G. J.; Dellby, N.; Hrcirik, P.; Murfitt, M. F.; Own, C. S.; Szilagyi, Z. S. High-Energy-Resolution Monochromator for Aberration-Corrected Scanning Transmission Electron Microscopy/electron Energy-Loss Spectroscopy. *Philos. Trans. A. Math. Phys. Eng. Sci.* **2009**, *367*, 3683–3697.
- (82) Subramanian, S.; Clark, G.; Ly, K.; Chrasticky, T. Energy-Filtered Transmission Electron Microscopy (EFTEM) of Semiconductor Devices. *Electron. Device Fail. Anal.* **2010**, *13*, 20–28.

- (83) Weyland, M.; Midgley, P. a. Electron Tomography. *Mater. Today* **2004**, *7*, 32–40.
- (84) Hawkes, P. W. The Electron Microscope as a Structure Projector. In *Electron Tomography*; Springer New York: New York, NY, 2006; pp. 83–111.
- (85) Bals, S.; Van Tendeloo, G.; Kisielowski, C. A New Approach for Electron Tomography: Annular Dark-Field Transmission Electron Microscopy. *Adv. Mater.* **2006**, *18*, 892 – +.
- (86) Bals, S.; Batenburg, K. J.; Verbeeck, J.; Sijbers, J.; Van Tendeloo, G. Quantitative Three-Dimensional Reconstruction of Catalyst Particles for Bamboo-like Carbon Nanotubes. *Nano Lett.* **2007**, *7*, 3669–3674.
- (87) Midgley, P. A.; Dunin-Borkowski, R. E. Electron Tomography and Holography in Materials Science. *Nat. Mater.* **2009**, *8*, 271–280.
- (88) Midgley, P. a; Weyland, M. 3D Electron Microscopy in the Physical Sciences: The Development of Z-Contrast and EFTEM Tomography. In *Ultramicroscopy*; 2003; Vol. 96, pp. 413–431.
- (89) Frank, J.; McEwen, B. F. Alignment by Cross-Correlation. In *Electron Tomography*; Frank, J., Ed.; Springer US: Boston, MA, 1992; pp. 205–213.
- (90) Schoenmakers, R. H. M.; Perquin, R. A.; Fliervoet, T. F.; Voorhout, W.; Schirmacher, H. New Software for High Resolution , High Throughput Electron Tomography. **2005**, 5–6.
- (91) Fernandez, J.-J. Computational Methods for Electron Tomography. *Micron*, 2012, *43*, 1010–1030.
- (92) Gilbert, P. Iterative Methods for the Three-Dimensional Reconstruction of an Object from Projections. *J. Theor. Biol.* **1972**, *36*, 105–117.

- (93) Van Eyndhoven, G.; Kurttepel, M.; Van Oers, C. J.; Cool, P.; Bals, S.; Batenburg, K. J.; Sijbers, J. Pore REconstruction and Segmentation (PORES) Method for Improved Porosity Quantification of Nanoporous Materials. *Ultramicroscopy* **2015**, *148*, 10–19.
- (94) Heidari Mezerji, H.; Van den Broek, W.; Bals, S. A Practical Method to Determine the Effective Resolution in Incoherent Experimental Electron Tomography. *Ultramicroscopy* **2011**, *111*, 330–336.
- (95) Batenburg, K. J.; Bals, S.; Sijbers, J.; Kübel, C.; Midgley, P. a; Hernandez, J. C.; Kaiser, U.; Encina, E. R.; Coronado, E. a; Van Tendeloo, G. 3D Imaging of Nanomaterials by Discrete Tomography. *Ultramicroscopy* **2009**, *109*, 730–740.
- (96) Fang, W.-C.; Fang, W.-L. Fast and Reversible Surface Redox Reduction in V2O5 Dispersed on CNx Nanotubes. *Chem. Commun. (Camb)*. **2008**, 5236–5238.
- (97) Cavanagh, A. S.; Wilson, C. a; Weimer, A. W.; George, S. M. Atomic Layer Deposition on Gram Quantities of Multi-Walled Carbon Nanotubes. *Nanotechnology* **2009**, *20*, 255602.
- (98) Liang, Y.; Wang, H.; Sanchez Casalongue, H.; Chen, Z.; Dai, H. TiO₂ Nanocrystals Grown on Graphene as Advanced Photocatalytic Hybrid Materials. *Nano Res.* **2010**, *3*, 701–705.
- (99) Sun, X.; Xie, M.; Wang, G.; Sun, H.; Cavanagh, A. S.; Travis, J. J.; George, S. M.; Lian, J. Atomic Layer Deposition of TiO₂ on Graphene for Supercapacitors. *Journal of The Electrochemical Society*, 2012, *159*, A364.
- (100) Čech, J.; Kalbáč, M.; Curran, S. a.; Zhang, D.; Dettlaff-Weglikowska, U.; Dunsch, L.; Yang, S.; Roth, S. HRTEM and EELS Investigation of Functionalized Carbon Nanotubes. *Phys. E Low-dimensional Syst. Nanostructures* **2007**, *37*, 109–114.
- (101) Ren, Y.; Fu, Y. Q.; Liao, K.; Li, F.; Cheng, H. M. Fatigue Failure Mechanisms of Single-Walled Carbon Nanotube Ropes Embedded in Epoxy. *Appl. Phys. Lett.* **2004**, *84*, 2811.

- (102) Gojny, F. H.; Wichmann, M. H. G.; Köpke, U.; Fiedler, B.; Schulte, K. Carbon Nanotube-Reinforced Epoxy-Composites: Enhanced Stiffness and Fracture Toughness at Low Nanotube Content. *Compos. Sci. Technol.* **2004**, *64*, 2363–2371.
- (103) Hetherington, C. Aberration Correction for TEM. *Mater. Today* **2004**, *7*, 50–55.
- (104) Egerton, R. F. Choice of Operating Voltage for a Transmission Electron Microscope. *Ultramicroscopy* **2014**, *145*, 85–93.
- (105) Smith, B. W.; Luzzi, D. E. Electron Irradiation Effects in Single Wall Carbon Nanotubes. *J. Appl. Phys.* **2001**, *90*, 3509–3515.
- (106) Lepinay, K.; Lorut, F.; Pantel, R.; Epicier, T. Chemical 3D Tomography of 28nm High K Metal Gate Transistor: STEM XEDS Experimental Method and Results. *Micron* **2013**, *47*, 43–49.
- (107) Liao, X. Z.; Serquis, A.; Jia, Q. X.; Peterson, D. E.; Zhu, Y. T.; Xu, H. F. Effect of Catalyst Composition on Carbon Nanotube Growth. *Appl. Phys. Lett.* **2003**, *82*, 2694.
- (108) Kukovitsky, E. F.; L'vov, S. G.; Sainov, N. a.; Shustov, V. a.; Chernozatonskii, L. a. Correlation between Metal Catalyst Particle Size and Carbon Nanotube Growth. *Chem. Phys. Lett.* **2002**, *355*, 497–503.
- (109) Lee, C. J.; Park, J.; Yu, J. a. Catalyst Effect on Carbon Nanotubes Synthesized by Thermal Chemical Vapor Deposition. *Chem. Phys. Lett.* **2002**, *360*, 250–255.
- (110) Homma, Y.; Kobayashi, Y.; Ogino, T.; Takagi, D.; Ito, R.; Jung, Y.; Ajayan, P. Role of Transition Metal Catalysts in Single-Walled Carbon Nanotube Growth in Chemical Vapor Deposition. *J. Phys. Chem. B* **2003**, *107*, 12161–12164.
- (111) Magrez, A.; Seo, J. W.; Smajda, R.; Mionić, M.; Forró, L. Catalytic CVD Synthesis of Carbon Nanotubes: Towards High Yield and Low Temperature Growth. *Materials (Basel)*. **2010**, *3*, 4871–4891.

- (112) Melezhyk, a V; Rukhov, a V; Tugolukov, E. N.; Tkachev, a G. Some Aspects of Carbon Nanotubes Technology. *Carbon N. Y.* **2013**, *4*, 247–259.
- (113) Platschek, B.; Petkov, N.; Bein, T. Tuning the Structure and Orientation of Hexagonally Ordered Mesoporous Channels in Anodic Alumina Membrane Hosts: A 2D Small-Angle X-Ray Scattering Study. *Angew. Chemie* **2006**, *118*, 1152–1156.
- (114) Cauda, V.; Mühlstein, L.; Onida, B.; Bein, T. Tuning Drug Uptake and Release Rates through Different Morphologies and Pore Diameters of Confined Mesoporous Silica. *Microporous Mesoporous Mater.* **2009**, *118*, 435–442.
- (115) Wu, Y.; Cheng, G.; Katsov, K.; Sides, S. W.; Wang, J.; Tang, J.; Fredrickson, G. H.; Moskovits, M.; Stucky, G. D. Composite Mesostructures by Nano-Confinement. *Nat. Mater.* **2004**, *3*, 816–822.
- (116) Wu, Y.; Livneh, T.; Zhang, Y. X.; Cheng, G.; Wang, J.; Tang, J.; Moskovits, M.; Stucky, G. D. Template Synthesis of Highly Ordered Mesostructured Nanowires and Nanowire Arrays. *Nano Lett.* **2004**, *4*, 2337–2342.
- (117) Platschek, B.; Keilbach, A.; Bein, T. Mesoporous Structures Confined in Anodic Alumina Membranes. *Adv. Mater.* **2011**, *23*, 2395–2412.
- (118) Kresge, C. T.; Leonowicz, M. E.; Roth, W. J.; Vartuli, J. C.; Beck, J. S. Ordered Mesoporous Molecular Sieves Synthesized by a Liquid-Crystal Template Mechanism. *Nature* **1992**, *359*, 710–712.
- (119) Zhao, D.; Feng, J.; Huo, Q.; Melosh, N.; Fredrickson, G. H.; Chmelka, B. F.; Stucky, G. D. Triblock Copolymer Syntheses of Mesoporous Silica with Periodic 50 to 300 Angstrom Pores. *Science (80-.)*. **1998**, *279*, 548–552.
- (120) Gong, Z.; Ji, G.; Zheng, M.; Chang, X.; Dai, W.; Pan, L.; Shi, Y.; Zheng, Y. Structural Characterization of Mesoporous Silica Nanofibers Synthesized within Porous Alumina Membranes. *Nanoscale Res. Lett.* **2009**, *4*, 1257–1262.

- (121) Platschek, B.; Köhn, R.; Döblinger, M.; Bein, T. Formation Mechanism of Mesostructured Silica in Confined Space: An in Situ GISAXS Study. *Chemphyschem* **2008**, *9*, 2059–2067.
- (122) Platschek, B.; Petkov, N.; Himsl, D.; Zimdars, S.; Li, Z.; Köhn, R.; Bein, T. Vertical Columnar Block-Copolymer-Templated Mesoporous Silica via Confined Phase Transformation. *J. Am. Chem. Soc.* **2008**, *130*, 17362–17371.
- (123) Yamaguchi, a.; Kaneda, H.; Fu, W.; Teramae, N. Structural Control of Surfactant-Templated Mesoporous Silica Formed Inside Columnar Alumina Pores. *Adv. Mater.* **2008**, *20*, 1034–1037.
- (124) Platschek, B.; Petkov, N.; Bein, T. Tuning the Structure and Orientation of Hexagonally Ordered Mesoporous Channels in Anodic Alumina Membrane Hosts: A 2D Small-Angle X-Ray Scattering Study. *Angew. Chem. Int. Ed. Engl.* **2006**, *45*, 1134–1138.
- (125) Platschek, B.; Köhn, R.; Döblinger, M.; Bein, T. In Situ GISAXS Study of the Formation of Mesostructured Phases within the Pores of Anodic Alumina Membranes. *Langmuir* **2008**, *24*, 5018–5023.
- (126) Petkov, N.; Platschek, B.; Morris, M. A.; Holmes, J. D.; Bein, T. Oriented Growth of Metal and Semiconductor Nanostructures within Aligned Mesoporous Channels. *Chem. Mater.* **2007**, *19*, 1376–1381.
- (127) Platschek, B.; Petkov, N.; Himsl, D.; Zimdars, S.; Li, Z.; Köhn, R.; Bein, T. Vertical Columnar Block-Copolymer-Templated Mesoporous Silica via Confined Phase Transformation. *J. Am. Chem. Soc.* **2008**, *130*, 17362–17371.
- (128) Keilbach, A.; Moses, J.; Köhn, R.; Döblinger, M.; Bein, T. Electrodeposition of Copper and Silver Nanowires in Hierarchical Mesoporous Silica/Anodic Alumina Nanostructures. *Chem. Mater.* **2010**, *22*, 5430–5436.

- (129) Mühlstein, L.; Riederer, M.; Platschek, B.; Bein, T. In Situ Functionalization of Mesoporous Silica within the Pores of Anodic Alumina Membranes. *J. Mater. Chem.* **2009**, *19*, 9195.
- (130) Jeong, S.-H.; Hwang, H.-Y.; Lee, K.-H.; Jeong, Y. Template-Based Carbon Nanotubes and Their Application to a Field Emitter. *Appl. Phys. Lett.* **2001**, *78*, 2052.
- (131) Hu, W.; Gong, D.; Chen, Z.; Yuan, L.; Saito, K.; Grimes, C. a.; Kichambare, P. Growth of Well-Aligned Carbon Nanotube Arrays on Silicon Substrates Using Porous Alumina Film as a Nanotemplate. *Appl. Phys. Lett.* **2001**, *79*, 3083.
- (132) Iwasaki, T.; Motoi, T.; Den, T. Multiwalled Carbon Nanotubes Growth in Anodic Alumina Nanoholes. *Appl. Phys. Lett.* **1999**, *75*, 2044.
- (133) Jin Seung Lee; Geun Hoi Gu; Kim, H.; Kwang Seok Jeong; Bae, J.; Jung Sang Suh. Growth of Carbon Nanotubes on Anodic Aluminum Oxide Templates: Fabrication of a Tube-in-Tube and Linearly Joined Tube. *Chem. Mater.* **2001**, *13*, 2387–2391.
- (134) Shin, Y. S.; Yang, J. H.; Park, C.-Y.; Kwon, M. H.; Yoo, J.-B.; Yang, C. W. Synthesis of Crystalline Carbon Nanotube Arrays on Anodic Aluminum Oxide Using Catalyst Reduction with Low Pressure Thermal Chemical Vapor Deposition. *Jpn. J. Appl. Phys.* **2006**, *45*, 1869–1872.
- (135) Ciambelli, P.; Arurault, L.; Sarno, M.; Fontorbes, S.; Leone, C.; Datas, L.; Sannino, D.; Lenormand, P.; Du Plouy, S. L. B. Controlled Growth of CNT in Mesoporous AAO through Optimized Conditions for Membrane Preparation and CVD Operation. *Nanotechnology* **2011**, *22*, 265613.
- (136) Sui, Y. C.; González-León, J. a.; Bermúdez, a.; Saniger, J. M. Synthesis of Multi Branched Carbon Nanotubes in Porous Anodic Aluminum Oxide Template. *Carbon N. Y.* **2001**, *39*, 1709–1715.
- (137) Kyotani, T.; Tsai, L. F.; Tomita, A. Preparation of Ultrafine Carbon Tubes in Nanochannels of an Anodic Aluminum Oxide Film. *Chem. Mater.* **1996**, *8*, 2109–2113.

- (138) De los Arcos, T.; Garnier, M. G.; Seo, J. W.; Oelhafen, P.; Thommen, V.; Mathys, D. The Influence of Catalyst Chemical State and Morphology on Carbon Nanotube Growth. *J. Phys. Chem. B* **2004**, *108*, 7728–7734.
- (139) Nagaraju, N. Alumina and Silica Supported Metal Catalysts for the Production of Carbon Nanotubes. *J. Mol. Catal. A Chem.* **2002**, *181*, 57–62.
- (140) Magrez, A.; Smajda, R.; Seo, J. W.; Horváth, E.; Ribič, P. R.; Andresen, J. C.; Acquaviva, D.; Olariu, A.; Laurency, G.; Forró, L. Striking Influence of the Catalyst Support and Its Acid–Base Properties: New Insight into the Growth Mechanism of Carbon Nanotubes. *ACS Nano* **2011**, *5*, 3428–3437.
- (141) Yu, M. Strength and Breaking Mechanism of Multiwalled Carbon Nanotubes Under Tensile Load. *Science*, 2000, *287*, 637–640.
- (142) Shi, W.; Shen, Y.; Jiang, H.; Song, C.; Ma, Y.; Mu, J.; Yang, B.; Ge, D. Lysine-Attached Anodic Aluminum Oxide (AAO)–silica Affinity Membrane for Bilirubin Removal. *J. Memb. Sci.* **2010**, *349*, 333–340.
- (143) Xomeritakis, G.; Liu, N. G.; Chen, Z.; Jiang, Y.-B.; Köhn, R.; Johnson, P. E.; Tsai, C.-Y.; Shah, P. B.; Khalil, S.; Singh, S.; et al. Anodic Alumina Supported Dual-Layer Microporous Silica Membranes. *J. Memb. Sci.* **2007**, *287*, 157–161.
- (144) Yao, B.; Fleming, D.; Morris, M. A.; Lawrence, S. E. Structural Control of Mesoporous Silica Nanowire Arrays in Porous Alumina Membranes. **2004**, 4851–4855.
- (145) Yang, Z.; Niu, Z.; Cao, X.; Yang, Z.; Lu, Y.; Hu, Z.; Han, C. C. Template Synthesis of Uniform 1D Mesoporous Silica Materials and Their Arrays in Anodic Alumina Membranes. *Angew. Chem. Int. Ed. Engl.* **2003**, *42*, 4201–4203.
- (146) Wu, Y.; Cheng, G.; Katsov, K.; Sides, S. W.; Wang, J.; Tang, J.; Fredrickson, G. H.; Moskovits, M.; Stucky, G. D. Composite Mesoporous Structures by Nano-Confinement. *Nat. Mater.* **2004**, *3*, 816–822.

- (147) Ciesla, U.; Schüth, F. Ordered Mesoporous Materials. *Microporous Mesoporous Mater.* **1999**, *27*, 131–149.
- (148) Hoffmann, F.; Cornelius, M.; Morell, J.; Fröba, M. Silica-Based Mesoporous Organic-Inorganic Hybrid Materials. *Angew. Chem. Int. Ed. Engl.* **2006**, *45*, 3216–3251.
- (149) Kurttepel, M.; Deng, S.; Verbruggen, S. W.; Guzzinati, G.; Cott, D. J.; Lenaerts, S.; Verbeeck, J.; Van Tendeloo, G.; Detavernier, C.; Bals, S. Synthesis and Characterization of Photoreactive TiO₂/Carbon Nanosheet Composites. *J. Phys. Chem. C* **2014**, *118*, 140822231449007.
- (150) Meoto, S.; Coppens, M.-O. Anodic Alumina-Templated Synthesis of Mesostructured Silica Membranes – Current Status and Challenges. *J. Mater. Chem. A* **2014**, *2*, 5640.
- (151) Knez, M.; Nielsch, K.; Niinistö, L. Synthesis and Surface Engineering of Complex Nanostructures by Atomic Layer Deposition. *Adv. Mater.* **2007**, *19*, 3425–3438.
- (152) Deng, S. Templated Synthesis of Porous Materials via Atomic Layer Deposition, Ghent University, 2015.
- (153) Soleimani Dorcheh, a.; Abbasi, M. H. Silica Aerogel; Synthesis, Properties and Characterization. *J. Mater. Process. Technol.* **2008**, *199*, 10–26.
- (154) Kemell, M.; Pore, V.; Tupala, J.; Ritala, M.; Leskelä, M. Atomic Layer Deposition of Nanostructured TiO₂ Photocatalysts via Template Approach. *Chem. Mater.* **2007**, *19*, 1816–1820.
- (155) Elam, J. W.; Xiong, G.; Han, C. Y.; Wang, H. H.; Birrell, J. P.; Welp, U.; Hryn, J. N.; Pellin, M. J.; Baumann, T. F.; Poco, J. F.; et al. Atomic Layer Deposition for the Conformal Coating of Nanoporous Materials. *J. Nanomater.* **2006**, *2006*, 1–5.
- (156) Lee, J.; Ju, H.; Lee, J. K.; Kim, H. S.; Lee, J. Atomic Layer Deposition of TiO₂ Nanotubes and Its Improved Electrostatic Capacitance. *Electrochem. commun.* **2010**, *12*, 210–212.

- (157) Meng, X.; Geng, D.; Liu, J.; Li, R.; Sun, X. Controllable Synthesis of Graphene-Based Titanium Dioxide Nanocomposites by Atomic Layer Deposition. *Nanotechnology* **2011**, *22*, 165602.
- (158) Boukhalifa, S.; Evanoff, K.; Yushin, G. Atomic Layer Deposition of Vanadium Oxide on Carbon Nanotubes for High-Power Supercapacitor Electrodes. *Energy Environ. Sci.* **2012**, *5*, 6872.
- (159) Liu, C.; Wang, C.-C.; Kei, C.-C.; Hsueh, Y.-C.; Perng, T.-P. Atomic Layer Deposition of Platinum Nanoparticles on Carbon Nanotubes for Application in Proton-Exchange Membrane Fuel Cells. *Small* **2009**, *5*, 1535–1538.
- (160) Lu, S.-Y.; Tang, C.-W.; Lin, Y.-H.; Kuo, H.-F.; Lai, Y.-C.; Tsai, M.-Y.; Ouyang, H.; Hsu, W.-K. TiO₂-Coated Carbon Nanotubes: A Redshift Enhanced Photocatalysis at Visible Light. *Appl. Phys. Lett.* **2010**, *96*, 231915.
- (161) Wang, X. D.; Graugnard, E.; King, J. S.; Wang, Z. L.; Summers, C. J. Large-Scale Fabrication of Ordered Nanobowl Arrays. **2004**, 2–5.
- (162) Hamann, T. W.; Martinson, A. B. F.; Elam, J. W.; Pellin, M. J.; Hupp, J. T. Atomic Layer Deposition of TiO₂ on Aerogel Templates: New Photoanodes for Dye-Sensitized Solar Cells. **2008**, 10303–10307.
- (163) Williams, V. O.; Jeong, N. C.; Prasittichai, C.; Farha, O. K.; Pellin, M. J.; Hupp, J. T. Fast Transporting ZnO-TiO₂ Coaxial Photoanodes for Dye-Sensitized Solar Cells Based on ALD-Modified SiO₂ Aerogel Frameworks. *ACS Nano* **2012**, *6*, 6185–6196.
- (164) Fujishima, A.; Honda, K. Electrochemical Photolysis of Water at a Semiconductor Electrode. *Nature* **1972**, *238*, 37–38.
- (165) Chen, X.; Mao, S. S. Titanium Dioxide Nanomaterials: Synthesis, Properties, Modifications, and Applications. *Chem. Rev.* **2007**, *107*, 2891–2959.

- (166) Kay, A.; Grätzel, M. Low Cost Photovoltaic Modules Based on Dye Sensitized Nanocrystalline Titanium Dioxide and Carbon Powder. *Sol. Energy Mater. Sol. Cells* **1996**, *44*, 99–117.
- (167) Vivero-Escoto, J. L.; Chiang, Y.-D.; Wu, K. C.-W.; Yamauchi, Y. Recent Progress in Mesoporous Titania Materials: Adjusting Morphology for Innovative Applications. *Sci. Technol. Adv. Mater.* **2012**, *13*, 013003.
- (168) Su, C.; Hong, B.-Y.; Tseng, C.-M. Sol–gel Preparation and Photocatalysis of Titanium Dioxide. *Catal. Today* **2004**, *96*, 119–126.
- (169) Weinberger, B.; Garber, R. Titanium Dioxide Photocatalysts Produced by Reactive Magnetron Sputtering. *Appl. Phys. Lett.* **1995**, *66*, 2409–2411.
- (170) Li Puma, G.; Bono, A.; Krishnaiah, D.; Collin, J. G. Preparation of Titanium Dioxide Photocatalyst Loaded onto Activated Carbon Support Using Chemical Vapor Deposition: A Review Paper. *J. Hazard. Mater.* **2008**, *157*, 209–219.
- (171) Ban, C.; Xie, M.; Sun, X.; Travis, J. J.; Wang, G.; Sun, H.; Dillon, A. C.; Lian, J.; George, S. M. Atomic Layer Deposition of Amorphous TiO₂ on Graphene as an Anode for Li-Ion Batteries. *Nanotechnology* **2013**, *24*, 424002.
- (172) Ovenstone, J.; Yanagisawa, K. Effect of Hydrothermal Treatment of Amorphous Titania on the Phase Change from Anatase to Rutile during Calcination. *Chem. Mater.* **1999**, *32*, 2770–2774.
- (173) Yang, Y.; Qu, L.; Dai, L.; Kang, T. S.; Durstock, M. Electrophoresis Coating of Titanium Dioxide on Aligned Carbon Nanotubes for Controlled Syntheses of Photoelectronic Nanomaterials. *Adv. Mater.* **2007**, *19*, 1239–1243.
- (174) Verbeeck, J.; Van Aert, S. Model Based Quantification of EELS Spectra. *Ultramicroscopy* **2004**, *101*, 207–224.

- (175) Deng, S.; Verbruggen, S. W.; He, Z.; Cott, D. J.; Vereecken, P. M.; Martens, J. a.; Bals, S.; Lenaerts, S.; Detavernier, C. Atomic Layer Deposition-Based Synthesis of Photoactive TiO₂ Nanoparticle Chains by Using Carbon Nanotubes as Sacrificial Templates. *RSC Adv.* **2014**, *4*, 11648.
- (176) Knaepen, W.; Gaudet, S.; Detavernier, C.; Van Meirhaeghe, R. L.; Sweet, J. J.; Lavoie, C. In Situ X-Ray Diffraction Study of Metal Induced Crystallization of Amorphous Germanium. *J. Appl. Phys.* **2009**, *105*, 083532.
- (177) Verbruggen, S. W.; Deng, S.; Kurttepli, M.; Cott, D. J.; Vereecken, P. M.; Bals, S.; Martens, J. a.; Detavernier, C.; Lenaerts, S. Photocatalytic Acetaldehyde Oxidation in Air Using Spacious TiO₂ Films Prepared by Atomic Layer Deposition on Supported Carbonaceous Sacrificial Templates. *Appl. Catal. B Environ.* **2014**, *160-161*, 204–210.
- (178) Bertoni, G.; Beyers, E.; Verbeeck, J.; Mertens, M.; Cool, P.; Vansant, E. F.; Van Tendeloo, G. Quantification of Crystalline and Amorphous Content in Porous Samples from Electron Energy Loss Spectroscopy. *Ultramicroscopy* **2006**, *106*, 630–635.
- (179) Aarik, J.; Aidla, A.; Mändar, H.; Sammelselg, V. Anomalous Effect of Temperature on Atomic Layer Deposition of Titanium Dioxide. *J. Cryst. Growth* **2000**, *220*, 531–537.
- (180) Tian, G.; Fu, H.; Jing, L.; Tian, C. Synthesis and Photocatalytic Activity of Stable Nanocrystalline TiO₂ with High Crystallinity and Large Surface Area. *J. Hazard. Mater.* **2009**, *161*, 1122–1130.
- (181) Park, N.; van de Lagemaat, J.; Frank, A. J. Comparison of Dye-Sensitized Rutile- and Anatase-Based TiO₂ Solar Cells. *J. Phys. Chem. B* **2000**, *104*, 8989–8994.
- (182) Ben Naceur, J.; Gaidi, M.; Bousbih, F.; Mechiakh, R.; Chtourou, R. Annealing Effects on Microstructural and Optical Properties of Nanostructured-TiO₂ Thin Films Prepared by Sol–gel Technique. *Curr. Appl. Phys.* **2012**, *12*, 422–428.
- (183) Ye, Q.; Liu, P. Y.; Tang, Z. F.; Zhai, L. Hydrophilic Properties of Nano-TiO₂ Thin Films Deposited by RF Magnetron Sputtering. *Vacuum* **2007**, *81*, 627–631.

- (184) Dendooven, J.; Goris, B.; Devloo-Casier, K.; Levrau, E.; Biermans, E.; Baklanov, M. R.; Ludwig, K. F.; Voort, P. Van Der; Bals, S.; Detavernier, C. Tuning the Pore Size of Ink-Bottle Mesopores by Atomic Layer Deposition. *Chem. Mater.* **2012**, *24*, 1992–1994.
- (185) Zhu, H.; Wei, J.; Wang, K.; Wu, D. Applications of Carbon Materials in Photovoltaic Solar Cells. *Sol. Energy Mater. Sol. Cells* **2009**, *93*, 1461–1470.
- (186) Brown, P.; Takechi, K.; Kamat, P. Single-Walled Carbon Nanotube Scaffolds for Dye-Sensitized Solar Cells. *J. Phys. Chem. C* **2008**, *112*, 4776–4782.
- (187) Verbruggen, S. W.; Masschaele, K.; Moortgat, E.; Korany, T. E.; Hauchecorne, B.; Martens, J. a.; Lenaerts, S. Factors Driving the Activity of Commercial Titanium Dioxide Powders towards Gas Phase Photocatalytic Oxidation of Acetaldehyde. *Catal. Sci. Technol.* **2012**, *2*, 2311.
- (188) Li, Y.; Fu, Z.-Y.; Su, B.-L. Hierarchically Structured Porous Materials for Energy Conversion and Storage. *Adv. Funct. Mater.* **2012**, *22*, 4634–4667.
- (189) Agarwala, S.; Kevin, M.; Wong, a S. W.; Peh, C. K. N.; Thavasi, V.; Ho, G. W. Mesophase Ordering of TiO₂ Film with High Surface Area and Strong Light Harvesting for Dye-Sensitized Solar Cell. *ACS Appl. Mater. Interfaces* **2010**, *2*, 1844–1850.
- (190) Cheng, F.; Tao, Z.; Liang, J.; Chen, J. Template-Directed Materials for Rechargeable Lithium-Ion Batteries. *Chem. Mater.* **2008**, *20*, 667–681.
- (191) Kim, S. W.; Han, T. H.; Kim, J.; Gwon, H.; Moon, H. S.; Kang, S. W.; Kim, S. O.; Kang, K. Fabrication and Electrochemical Characterization of TiO₂ Three-Dimensional Nanonetwork Based on Peptide Assembly. *ACS Nano* **2009**, *3*, 1085–1090.

- (192) Min, Y.-S.; Bae, E. J.; Jeong, K. S.; Cho, Y. J.; Lee, J.-H.; Choi, W. B.; Park, G.-S. Ruthenium Oxide Nanotube Arrays Fabricated by Atomic Layer Deposition Using a Carbon Nanotube Template. *Adv. Mater.* **2003**, *15*, 1019–1022.
- (193) Comstock, D. J.; Christensen, S. T.; Elam, J. W.; Pellin, M. J.; Hersam, M. C. Tuning the Composition and Nanostructure of Pt/Ir Films via Anodized Aluminum Oxide Templated Atomic Layer Deposition. *Adv. Funct. Mater.* **2010**, *20*, 3099–3105.
- (194) Korhonen, J. T.; Hiekkataipale, P.; Malm, J.; Karppinen, M.; Ikkala, O.; Ras, R. H. a. Inorganic Hollow Nanotube Aerogels by Atomic Layer Deposition onto Native Nanocellulose Templates. *ACS Nano* **2011**, *5*, 1967–1974.
- (195) Li, F.; Yao, X.; Wang, Z.; Xing, W.; Jin, W.; Huang, J.; Wang, Y. Highly Porous Metal Oxide Networks of Interconnected Nanotubes by Atomic Layer Deposition. *Nano Lett.* **2012**, *12*, 5033–5038.
- (196) Lee, J. S.; Min, B.; Cho, K.; Kim, S.; Park, J.; Lee, Y. T.; Kim, N. S.; Lee, M. S.; Park, S. O.; Moon, J. T. Al₂O₃ Nanotubes and Nanorods Fabricated by Coating and Filling of Carbon Nanotubes with Atomic-Layer Deposition. *J. Cryst. Growth* **2003**, *254*, 443–448.
- (197) Du, N.; Zhang, H.; Chen, B.; Xiangyang, M.; Liu, Z.; Wu, J.; Yang, D. Porous Indium Oxide Nanotubes: Layer-by-Layer Assembly on Carbon-Nanotube Templates and Application for Room-Temperature NH₃ Gas Sensors. *Adv. Mater.* **2007**, *19*, 1641–1645.
- (198) Aksel, S.; Eder, D. Catalytic Effect of Metal Oxides on the Oxidation Resistance in Carbon Nanotube–inorganic Hybrids. *Journal of Materials Chemistry*, 2010, *20*, 9149.
- (199) Green, J. M.; Dong, L.; Gutu, T.; Jiao, J.; Conley, J. F.; Ono, Y. ZnO-Nanoparticle-Coated Carbon Nanotubes Demonstrating Enhanced Electron Field-Emission Properties. *J. Appl. Phys.* **2006**, *99*, 0–4.

- (200) Marichy, C.; Pinna, N. Carbon-Nanostructures Coated/decorated by Atomic Layer Deposition: Growth and Applications. *Coord. Chem. Rev.* **2013**, *257*, 3232–3253.
- (201) Alexander, L.; Klug, H. P. Determination of Crystallite Size with the X-Ray Spectrometer. *J. Appl. Phys.* **1950**, *21*, 137.
- (202) Rongé, J.; Deng, S.; Pulinthanathu Sree, S.; Bosserez, T.; Verbruggen, S. W.; Kumar Singh, N.; Dendooven, J.; Roeffaers, M. B. J.; Taulelle, F.; De Volder, M.; et al. Air-Based Photoelectrochemical Cell Capturing Water Molecules from Ambient Air for Hydrogen Production. *RSC Adv.* **2014**, *4*, 29286.
- (203) Osterloh, F. E. Inorganic Materials as Catalysts for Photochemical Splitting of Water. *Chemistry of Materials*, 2008, *20*, 35–54.
- (204) Zhang, S.; Yuan, X.-Z.; Hin, J. N. C.; Wang, H.; Friedrich, K. A.; Schulze, M. A Review of Platinum-Based Catalyst Layer Degradation in Proton Exchange Membrane Fuel Cells. *Journal of Power Sources*, 2009, *194*, 588–600.
- (205) Tanaka, H.; Taniguchi, M.; Uenishi, M.; Kajita, N.; Tan, I.; Nishihata, Y.; Mizuki, J.; Narita, K.; Kimura, M.; Kaneko, K. Self-Regenerating Rh- and Pt-Based Perovskite Catalysts for Automotive-Emissions Control. *Angew. Chemie* **2006**, *118*, 6144–6148.
- (206) Shui, J.; Li, J. C. M. Platinum Nanowires Produced by Electrospinning. *Nano Lett.* **2009**, *9*, 1307–1314.
- (207) Yang, D.; Sun, S.; Meng, H.; Dodelet, J. P.; Sacher, E. Formation of a Porous Platinum Nanoparticle Froth for Electrochemical Applications, Produced without Templates, Surfactants, or Stabilizers. *Chem. Mater.* **2008**, *20*, 4677–4681.
- (208) Sun, S.; Zhang, G.; Zhong, Y.; Liu, H.; Li, R.; Zhou, X.; Sun, X. Ultrathin Single Crystal Pt Nanowires Grown on N-Doped Carbon Nanotubes. *Chem. Commun. (Camb)*. **2009**, 7048–7050.

- (209) Sattayasamitsathit, S.; O'Mahony, A. M.; Xiao, X.; Brozik, S. M.; Washburn, C. M.; Wheeler, D. R.; Cha, J.; Burckel, D. B.; Polsky, R.; Wang, J. Highly Dispersed Pt Nanoparticle-Modified 3D Porous Carbon: A Metallized Carbon Electrode Material. *Electrochem. commun.* **2011**, *13*, 856–860.
- (210) Akbar, S.; Elliott, J. M.; Rittman, M.; Squires, A. M. Facile Production of Ordered 3D Platinum Nanowire Networks with “Single Diamond” Bicontinuous Cubic Morphology. *Adv. Mater.* **2013**, *25*, 1160–1164.
- (211) Shen, Z.; Matsuki, Y.; Higashimine, K.; Miyake, M.; Shimoda, T. Formation of Porous Pt Nanoparticles through Core[^]ndash;Shell Pt[^]ndash;Al Nanoalloys and Wet Chemical Etching. *Chemistry Letters*, 2012, *41*, 644–646.
- (212) Shui, J. L.; Chen, C.; Li, J. C. M. Evolution of Nanoporous Pt-Fe Alloy Nanowires by Dealloying and Their Catalytic Property for Oxygen Reduction Reaction. *Adv. Funct. Mater.* **2011**, *21*, 3357–3362.
- (213) Zhang, X.; Lu, W.; Da, J.; Wang, H.; Zhao, D.; Webley, P. a. Porous Platinum Nanowire Arrays for Direct Ethanol Fuel Cell Applications. *Chem. Commun. (Camb)*. **2009**, 195–197.
- (214) Zhou, Y.; King, D. M.; Liang, X.; Li, J.; Weimer, A. W. Optimal Preparation of Pt/TiO₂ Photocatalysts Using Atomic Layer Deposition. *Appl. Catal. B Environ.* **2010**, *101*, 54–60.
- (215) Enterkin, J. a.; Poepelmeier, K. R.; Marks, L. D. Oriented Catalytic Platinum Nanoparticles on High Surface Area Strontium Titanate Nanocuboids. *Nano Lett.* **2011**, *11*, 993–997.
- (216) Liu, C.; Wang, C.-C.; Kei, C.-C.; Hsueh, Y.-C.; Perng, T.-P. Atomic Layer Deposition of Platinum Nanoparticles on Carbon Nanotubes for Application in Proton-Exchange Membrane Fuel Cells. *Small* **2009**, *5*, 1535–1538.

- (217) Chen, Z.; Waje, M.; Li, W.; Yan, Y. Supportless Pt and PtPd Nanotubes as Electrocatalysts for Oxygen-Reduction Reactions. *Angew. Chemie - Int. Ed.* **2007**, *46*, 4060–4063.
- (218) Liu, L.; Pippel, E. Low-Platinum-Content Quaternary PtCuCoNi Nanotubes with Markedly Enhanced Oxygen Reduction Activity. *Angew. Chemie - Int. Ed.* **2011**, *50*, 2729–2733.
- (219) Lehman, J. H.; Terrones, M.; Mansfield, E.; Hurst, K. E.; Meunier, V. Evaluating the Characteristics of Multiwall Carbon Nanotubes. *Carbon N. Y.* **2011**, *49*, 2581–2602.

Scientific Contributions

Scientific contributions

List of Publications

- Hyunchul Oh, Thomas Gennett, Plamen Atanassov, **Mert Kurttepel**i, Sara Bals, Katherine E Hurst, Michael Hirscher, “Hydrogen adsorption properties of platinum decorated hierarchically structured templated carbons”, **2013**, *Microporous and Mesoporous Materials*, Volume 177, Pages 66-74.
- Shaoren Deng*, **Mert Kurttepel**i*, Stella Deheryan, Daire J Cott, Philippe M Vereecken, Johan A Martens, Sara Bals, Gustaaf van Tendeloo, Christophe Detavernier, “Synthesis of a 3D network of Pt nanowires by atomic layer deposition on a carbonaceous template”, **2014**, *Nanoscale*, Volume 6, Issue 12, Pages 6939-6944.
- **Mert Kurttepel**i*, Shaoren Deng*, Sammy W Verbruggen, Giulio Guzzinati, Daire J Cott, Silvia Lenaerts, Jo Verbeeck, Gustaaf Van Tendeloo, Christophe Detavernier, Sara Bals, “Synthesis and Characterization of Photoreactive TiO₂-Carbon Nanosheet Composites”, **2014**, *The Journal of Physical Chemistry C*, Volume 118, Issue 36, Pages 21031-21037.
- Sammy W Verbruggen, Shaoren Deng, **Mert Kurttepel**i, Daire J Cott, Philippe M Vereecken, Sara Bals, Johan A Martens, Christophe Detavernier, Silvia Lenaerts, “Photocatalytic acetaldehyde oxidation in air using spacious TiO₂ films prepared by atomic layer deposition on supported carbonaceous sacrificial templates”, **2014**, *Applied Catalysis B: Environmental*, Volume 160, Pages 204-210.
- Shaoren Deng*, **Mert Kurttepel**i*, Daire J Cott, Sara Bals, Christophe Detavernier, “Porous nanostructured metal oxides synthesized through atomic layer deposition on a carbonaceous template followed by calcination”, **2015**, *Journal of Materials Chemistry A*, Volume 3, Issue 6, Pages 2642-2649.
- Geert Van Eyndhoven, **Mert Kurttepel**i, Cynthia J. Van Oers, Penny Cool, Sara Bals, K. Joost Batenburg, Jan Sijbers, “Pore REconstruction and Segmentation (PORES) method for improved porosity quantification of nanoporous materials”, **2015**, *Ultramicroscopy*, Volume 148, Pages 10-19.

- **Mert Kurttepel**i*, Roel Locus*, Sara Bals, Bert Sels, ‘Tailored Synthesis of Hierarchical Mesoporous Membranes by Evaporation Induced Self-Assembly’, to be submitted.

* These authors contributed equally.

- Elke Verheyen, Changbum Jo, **Mert Kurttepel**i, Gina Vanbutsele, Elena Gobechiya, Tamás I Korányi, Sara Bals, Gustaaf Van Tendeloo, Ryong Ryoo, Christine EA Kirschhock, Johan A Martens, “Molecular shape-selectivity of MFI zeolite nanosheets in n-decane isomerization and hydrocracking”, **2013**, *Journal of Catalysis*, Volume 300, Pages 70-80.
- Jolien Dendooven, Kilian Devloo-Casier, Matthias Ide, Kathryn Grandfield, **Mert Kurttepel**i, Karl F Ludwig, Sara Bals, Pascal Van Der Voort, Christophe Detavernier, “Atomic layer deposition-based tuning of the pore size in mesoporous thin films studied by in situ grazing incidence small angle X-ray scattering”, **2014**, *Nanoscale*, Volume 6, Issue 24, Pages 14991-14998.
- Cynthia J Van Oers, **Mert Kurttepel**i, Myrjam Mertens, Sara Bals, Vera Meynen, Pegie Cool, “Zeolite β nanoparticles based bimodal structures: mechanism and tuning of the porosity and zeolitic properties”, **2014**, *Microporous and Mesoporous Materials*, Volume 185, Pages 204-212.
- Ellen Bertels, Kevin Bruyninckx, **Mert Kurttepel**i, Mario Smet, Sara Bals, Bart Goderis, “Highly Efficient Hyperbranched CNT Surfactants: Influence of Molar Mass and Functionalization”, **2014**, *Langmuir*, Volume 30, Issue 41, Pages 12200-12209.
- Thijs Ennaert, Jan Geboers, Elena Gobechiya, Christophe M Courtin, **Mert Kurttepel**i, Kristof Houthoofd, Christine EA Kirschhock, Pieter CMM Magusin, Sara Bals, Pierre A Jacobs, Bert F Sels, “Conceptual Frame Rationalizing the Self-Stabilization of H-USY Zeolites in Hot Liquid Water”, **2014**, *ACS Catalysis*, Volume 5, Issue 2, Pages 754-768.
- Leen Van Tendeloo, Wauter Wangermez, **Mert Kurttepel**i, Benny de Blochouse, Sara Bals, Gustaaf Van Tendeloo, Johan A Martens, André Maes, Christine EA Kirschhock, Eric Breynaert, “Chabazite: Stable Cation-Exchanger in Hyper Alkaline

Concrete Pore Water”, **2015**, *Environmental science & technology*, Volume 49, Issue 4, Pages 2358-2365.

- Xia Sheng, Nick Daems, Bart Geboes, **Mert Kurttepli**, Sara Bals, Tom Breugelmans, Annick Hubin, Ivo FJ Vankelecom, Paolo P Pescarmona, “N-doped ordered mesoporous carbons prepared by a two-step nanocasting strategy as highly active and selective electrocatalysts for the reduction of O₂ to H₂O₂”, **2015**, *Applied Catalysis B: Environmental*, Volume 176, Pages 212-224.

Conference Proceedings

- **Mert Kurttepli**, Eva Bladt, Shaoren Deng, Daire J. Cott, Christophe Detavernier, Sara Bals, Gustaaf Van Tendeloo, “XEDS-STEM tomography of multilayer nanotubes for 3D chemical characterization”, 18th International Microscopy Conference, Prague, **2014**, Oral Presentation.
- **Mert Kurttepli**, Shaoren Deng, Sammy W. Verbruggen, Giulio Guzzinati, Daire J. Cott, Silvia Lenaerts, Christophe Detavernier, Sara Bals, Gustaaf Van Tendeloo, “TEM study of TiO₂ photocatalyst layers deposited on carbon nanosheet templates by atomic layer deposition”, 18th International Microscopy Conference, Prague, **2014**, Poster Presentation.

Acknowledgements

This doctoral thesis would not have been possible without the guidance and help of several individuals who, in one way or another, contributed and extended their valuable assistance in preparation and completion of this study.

First and foremost, my utmost gratitude to my promoter, Prof. Dr. Sara Bals, whose encouragement and support I will always remember and appreciate throughout my whole life. Thank you so much for providing the opportunity to pursue my PhD in the best group of EMAT, for your guiding and support all the way.

The work presented in this thesis cannot be obtained without the successful cooperation between KU Leuven, Ghent University and University of Antwerp. I would like to thank Prof. Dr. Jin Won Seo (KU Leuven), Prof. Dr. Christophe Detavernier (Ghent University), Dr. Shaoren Deng (Ghent University), Prof. Dr. Gustaaf Van Tendeloo (University of Antwerp), Prof. Dr. Silvia Lenaerts (University of Antwerp) and Dr. Sammy Verbruggen (University of Antwerp) for the best samples, invaluable suggestions and discussions.

It is difficult to leave my gratitude unsaid to people of EMAT. With their friendship, kindness and their great efforts to explain things in a clear and simple way, they helped and encouraged me to build and pursue my career on TEM. Thank you all for being there for me.

I am indebted to many of my colleagues and friends for providing the most stimulating and fun environment to learn and to enjoy. I am especially grateful to Maria Batuk, Dmitry Batuk, Eva Bladt, Burak Erkartal, Roland Fassbender, Giulio Guzzinati, Gerardo Martinez, Maria Meledina, Alexander Meledin, Selin Öztürk, Martin Pfannmöller, Kadir Şentosun, Engin Torun and Onur Urş.

ACKNOWLEDGEMENTS

I wish to thank Marta Babic for helping me get through the difficult times, for all the emotional support and caring, for providing a loving environment, for the times we shared, and for everything there was and there will be.

I wish to thank my entire extended family for supporting and caring for me. My brother, Berk Kurttepelı, my sister, Ebru Kurttepelı, my nephews, Erdal Ege Kurttepelı and Defne Kurttepelı, and my cousins, Kayhan Ateşçi, Gürcan Bulut, Yiğit Kurttepelı and Selda Kurttepelı. I love you all.

Lastly, and most importantly, I wish to thank my mother, Emine Kurttepelı, and my father, Erdal Kurttepelı. They raised me, supported me, taught me, and loved me. To them I dedicate this thesis. To them I dedicate my life.

Mert Kurttepelı

